UNIVERSITÀ DEGLI STUDI DI PALERMO

Dottorato di Ricerca in Aim Highest, Advances in Modelling, Health-Monitoring, Infrastructures, Geomatics, Geotechnics, Hazards, Engineering Structures, Transportation

Dipartimento di Ingegneria

Settore Scientifico Disciplinare ICAR/07

INFLUENCE OF PRE-EXISTING FAILURE PLANES ON CLAY SHEAR STRENGTH: A SLIDING BLOCK METHOD ANALYSIS

IL DOTTORE

Ing. Mohammad Esmaeel Rahbari

IL COORDINATORE

Prof. Ing. Giuseppe Campione

I TUTOR

Prof. Ing. Alessio Ferrari

Prof. Ing. Marco Rosone

CICLO XXXVI

ANNO CONSEGUIMENTO TITOLO 2024

Table of Contents

Acknowledgements

I extend my deepest gratitude to all who have supported and guided me through the journey of completing this thesis. This work is not just a reflection of my efforts but a testament to the invaluable contributions of many who have been integral to my academic and personal growth during this enlightening and challenging period.

First and foremost, my heartfelt thanks to my family in Iran. Being away from home for such a prolonged period brought unique challenges, alleviated only by their unwavering support and encouragement. My mother, Zahra Bibi, has been a steadfast source of emotional strength; her love and support have anchored me in difficult times. My father, Ahmad, whom I deeply miss and eagerly look forward to seeing, along with my older siblings, Arash and Arian, have been like additional parents to me. The sacrifices and constant encouragement from these four irreplaceable souls have been crucial to my perseverance and success.

I am immensely grateful to my professors, Alessio Ferrari and Marco Rosone, whose guidance was vital to my research and academic development. Their patience and dedication not only deepened my understanding of complex subjects but also prepared me for future scholarly endeavours. Their extensive investment in my work has profoundly shaped my academic journey. I also owe a special thank you to Dr. Sapienza, who provided considerable support in the geotechnics laboratory.

Additionally, I owe a great deal of thanks to my friends who stood by me throughout this journey: Maria, Erfan, Nazanin, Niloofar, Mozhgan, Mohammad in Palermo, and Behrooz, Farzan, Sina, Mohammadali, Farzad, Ali, who have shared with me their experiences in their immigration journey in other countries, as well as my friends in Iran, Arman and Hossein. Their companionship and support have lightened the burdens of my academic responsibilities, making this challenging journey more enjoyable and rewarding.

This thesis would not have been possible without the collective support and encouragement from everyone mentioned. I am eternally grateful to each for their unique contributions to my life and studies.

Abstract

This thesis investigates the shearing behaviour of Speswhite Kaolin through triaxial testing under both saturated drained and undrained conditions, analyzing homogeneous specimens as well as those with pre-existing failure planes. The primary objective of the study was to evaluate the shearing response of the material under varying stress states and to determine if extended shearing tests up to 30% axial strains could reveal the material's residual condition. A novel analytical approach, the Sliding Block Method (SBM), was developed and compared against conventional methods to analyze the shearing stage behaviour more effectively. This innovative method is designed to provide a more accurate representation of stress states. The force equilibrium on the soil body is evaluated considering the actual forces acting on the external surfaces of the specimen during the shearing stage and incorporating a comprehensive area correction of the failure surfaces developed in the sample.

Significant findings from this study indicate that the SBM enhances the interpretation of triaxial test data, especially by considering the friction between the specimen's top surface and the porous stone. In contrast to conventional methods, which often overlook such interactions, the SBM allows for a more detailed understanding of shearing process, particularly in the post-peak and post-sliding phases of testing.

This thesis demonstrates that the SBM offers a realistic approach to interpreting shearing behaviour data, potentially applicable to other triaxial shearing tests. This method is beneficial for geotechnical engineering applications, providing deeper insights into the material's behaviour under stress. The integration of friction considerations into the SBM significantly refines the analysis, leading to more accurate predictions and a richer understanding compared to conventional methodologies.

List of Symbols

A	Soil activity
A_c	Area of the projected failure plane or pre-existing failure plane on the specimen's top surface
A_{ci}	Initial area of the projected new failure plane on the top surface of the specimen during the new failure plane formation in the post-sliding phase
A_{L1}	Lateral surface area of the upper segment of the specimen's top block
A_{L2}	Lateral surface area of the lower segment of the specimen's top block
A_{L3}	Lateral surface area of the lower segment of the specimen's top block during the new failure plane formation in the post-sliding phase
A_{out}	The area of S* force
A_s	Arc area used to calculate changes in the contact area
ASTM	American Society for Testing and Materials
A_t	Area of the triangle used to determine variations in contact area
A_{TS}	Specimen's top surface area
B	Skempton value
b	Triangle's base
c	Cohesion intercept
CD	Consolidated Drained test
CM	Conventional Method
CNL	Constant Normal Load
CNS	Constant Normal Stiffness
CU	Consolidated Undrained test
DI	Damage index
d_n	Peak dilation angle
D_{pf}	Drop modulus
e	Void ratio
E_i	Tangent modulus
E_s	Secant modulus
ESP	Effective stress path
F_f	The friction force between the top surface of the specimen and porous stone
F_{L1}	Lateral force resulted from confining pressure acting on the upper segment of the specimen's top block
F_{L2}	Lateral force resulted from confining pressure acting on the lower segment of the specimen's top block
F_{L3}	Lateral force resulted from confining pressure acting on the lower segment of the specimen's top block during the new failure plane formation in the post-sliding phase scenario
F_q	Axial load recorded by submerged load cell in triaxial apparatus
F_{TS}	Specimen's top surface force resulted from confining pressure
i	Asperity angle
i_0	Initial asperity angle
ISRM	International Society for Rock Mechanics
JCS	Joint Wall Compressive Strength
JOC	Joint Over-Closure value
JRC	The Joint Roughness Coefficient
LVDT	Linear Variable Differential Transformers
N	Normal force
N_c	Normal force acting on the plane of failure or pre-existing failure plane resulted from confining pressure
N_q	Normal force acting on the plane of failure or pre-existing failure plane resulted from deviatoric stress
N_θ	Normal force acting on the plane of failure or pre-existing failure plane
N'_θ	Normal force acting on the plane of failure or pre-existing failure plane by considering the pore water pressure effect
OCR	Over-consolidation ratio
p	Mean total stress
p'	Mean effective stress
p'_0	Mean effective stress at consolidation stage
PI	Plasticity index
Pwp, u	$(u_b + \Delta u)$ pore water pressure
q	Deviatoric stress
r	Specimen's radius
r_i	Initial radius of the specimen
S	the force resulted from confining pressure on the new or pre-existing failure plane, which is not in the contact with the bottom block.
S*	the force resulted from confining pressure on the new failure plane, which is not in the contact with the bottom block in the new failure plane formation during post-sliding phase scenario
SBM	Sliding Block Method

S_f	The final phase of the force resulted from confining pressure on pre-existing failure plane, which is not in the contact with the bottom block in the new failure plane formation during post-sliding phase scenario.
s_n	The asperity shear angle
Sr	Degree of Saturation
T	Tangential force acting on the failure plane or pre-existing failure plane
t/a	Infill thickness to the average height of asperities
t_{100}	Time for complete consolidation
t_f	Time to failure
TSP	Total stress path
$u_{b,}$	Back pressure
w_l	Liquidity limit
w_p	Plasticity limit
w_r	Fracture energy dissipated under uniaxial compression
w_{r0}	total fracture energy dissipated under uniaxial compression
$(\sigma_\theta)_c$	Normal stress acting on the plane of failure or pre-existing failure plane resulted from confining pressure
$(\sigma_\theta)_q$	Normal stress acting on the plane of failure or pre-existing failure plane resulted from deviatoric stress
$(\tau_\theta)_c$	Tangential stress acting on the plane of failure or pre-existing failure plane resulted from confining pressure
$(\tau_\theta)_q$	Tangential stress acting on the plane of failure or pre-existing failure plane resulted from deviatoric stress
A_λ	Area of formed failure plane in post-sliding phase
$A_{\lambda\iota}$	Initial area of formed failure plane in post-sliding phase
A_θ	Area of failure plane or pre-existing failure plane
$A_{\theta\iota}$	Initial area of failure plane or pre-existing failure plane at the sliding onset
Δu	Excess pore water pressure
Δx	Horizontal displacement alongside the failure plane or pre-existing failure plane
Δx_f	Maximum Horizontal displacement alongside the pre-existing failure plane before new failure plane formation
Δz	Axial displacement of the failure plane or pre-existing failure plane
M	Specimen mass
T_q	Tangential force acting on the plane of failure or pre-existing failure plane resulted from deviatoric stress
T_θ	Tangential force acting on the plane of failure or pre-existing failure plane
β	Fracture angle
ε_a	Total axial strains, ($\varepsilon_{ac} + \varepsilon_{as}$)
ε_{ac}	Axial strains due to effect of compression in shearing phase
ε_{as}	Axial strains due to effect of sliding in shearing phase
ε_f	Typical range of strain at failure suggested by Head
ε_r	Radial strains
ε_v	Volumetric strains; ($\varepsilon_a + 2\varepsilon_r$) in conventional method and ($\varepsilon_{ac} + 2\varepsilon_r$) in sliding block method
ϕ_b	Basic friction angle of discontinuity
γ	Unit weight of soil
γ_d	Dry unit weight of soil
λ	Failure plane inclination from the horizon in the new failure plane formation in post-sliding phase scenario
$\theta°$	Failure plane or pre-existing failure plane inclination from the horizon
ρ_s	Soil-specific mass
σ_c	Uniaxial compression index
$\sigma'c$	Effective confining stress
σ_{ci}	Peak strength
σ_{cr}	Residual strength
σ_n	Normal stress
$\sigma_{n(CNL)}$	Normal stress under Constant Load Condition
σ_1	Axial stress in triaxial test, $\sigma_1 = \sigma_3 + q$
σ_3	Confining pressure in triaxial test
σ_θ	Normal stress acting on the plane of failure or pre-existing failure plane
τ_p	Peak shear stress of discontinuity
τ_θ	Tangential stress acting on the plane of failure or pre-existing failure plane
$\psi°$	Dilatancy angle

Chapter 1

Introduction

1.1 Objectives and Outline of the Thesis

This thesis investigates the shearing behaviour of Speswhite Kaolin, a reference material, through triaxial testing under both saturated drained and undrained conditions. The experimental work was conducted on homogeneous specimens and specimens with pre-existing failure planes to evaluate the material's response under these conditions.

From an analytical perspective, this study aims to develop a novel approach for analysing the shearing stage behaviour of materials using the Sliding Block Method. The objective is to determine whether this new perspective offers better insights following the formation of a new failure plane in homogeneous specimens (post-peak) and after the onset of sliding in specimens with pre-existing failure planes (post-sliding). Additionally, the research seeks to ascertain if continuing the shearing tests up to 30% axial strains could potentially reach the residual condition of the material.

The thesis is structured into several chapters, each addressing different aspects of the study:

Chapter 2 reviews previous studies on the shearing behaviour of rocks with discontinuities, the post-peak and residual strength of fine-grained soils.

Chapter 3 details the methodology of the experimental work, including the densification of the material to achieve the desired void ratio, the preparation and installation of specimens in the triaxial cell, and the conduction of triaxial tests under both drained and undrained conditions.

Chapter 4 focuses on the development of the Sliding Block Method by considering the force balance and area correction. It explores the application of this method to shearing behaviour data and compares it with conventional methods to assess its efficacy and accuracy.

Finally, **Chapter 5** provides a summary of the findings from the research and discusses the implications of these results. It also suggests directions for further investigations to expand upon the insights gained from this study.

This thesis aims to contribute to the field by offering a refined analytical tool for understanding and predicting the shearing behaviour of clay materials under saturated testing condition.

Chapter 2

Shear Strength in Discontinuities

2.1 Introduction

Laboratory simulations of rock discontinuities often involve artificially made specimens due to the challenge of obtaining natural samples with consistent characteristics. To create these models, a range of methods from traditional saw-toothed moulds (Ladanyi & Archambault, 1977; Johnston et al., 1987; Phien-Wej et al., 1990; Li et al., 2015) to advanced 3D printing (Kim et al., 2015; Jiang et al., 2016a; Jiang et al., 2016b) are utilized, aiming to replicate the complex textures found in natural rock formations. These techniques allow researchers to systematically study how variations in surface types, impact shear strength (Kodikara & Johnston, 1994). The shear strength pattern of regular, saw-toothed discontinuities typically displays a two-part linear graph, whereas the shear strength profile for naturally textured discontinuities shows a curved pattern, reflecting the complexity of natural rock surfaces (Patton, 1966). To gain a deeper understanding of shear behaviour in the presence of discontinuities, researchers have introduced factors such as the Joint Roughness Coefficient (JRC) and Joint Wall Compressive Strength (JCS). Their investigations have also shed light on the impact of various factors, including boundary conditions, normal stress on the discontinuity surface, shearing rates, humidity, pore water pressure, over-consolidation ratio, and infill thickness. These elements provide insights that are further elaborated in two distinct sections of this chapter: one focusing on clean rock discontinuities and the other on infilled rock discontinuities.

2.2 Shear Strength of Rock Discontinuities

2.2.1 Shear Strength of Clean Rock Discontinuities

- **JRC:**

The shear strength of rock discontinuities is profoundly influenced by their surface roughness. Rougher surfaces generally lead to stronger discontinuities, and this relationship diminishes with wider gaps or mismatched discontinuity alignments (Fig. 1). The Joint Roughness Coefficient (JRC), introduced by (Barton et al., 1974), is an established measure for this roughness, widely recognized by (ISRM, 1978; ASTM, 2016).

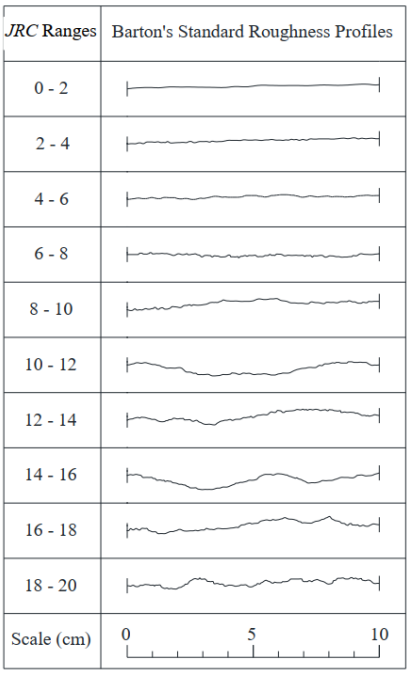

Fig. 1) Standard profiles illustrating the range of Joint Roughness Coefficient (JRC) values (Barton et al., 1974).

(Patton, 1966) also contributed significantly with his model predicting shear strength based on the discontinuity's asperity angle (i), which is a primarily dry-condition phenomenon (Equation 2.1),

$$\tau_p = \sigma_n \tan(\phi_b + i) \tag{2.1}$$

Where, τ_p, σ_n, and ϕ_b are peak shear strength of discontinuities, normal stress applied to discontinuity's surface, and basic friction angle of discontinuity, respectively. This approach is particularly relevant under conditions of low normal stress (shallow depth), where the asperity angle is more influential.

The Joint Roughness Coefficient (JRC) is typically determined by visually comparing the rock surface with established roughness profiles or through empirical test like the tilt or Schmidt Hammer tests (Barton & Choubey, 1977). However, these traditional methods carry a degree of subjectivity. As a result, alternative techniques have been developed, such as statistical analysis (Tse & Cruden, 1979; Yang et al., 2001), fractal methods (Maerz et al., 1990; Xie & Pariseau, 1995; Cheng, 1997) and contact area approaches (Grasselli, 2002; Grasselli & Egger, 2003) to provide a more objective characterization of discontinuity roughness. These methods seek to correlate with the JRC to ensure a more precise and reliable measure of rock surface roughness.

- **JCS:**

Barton's concept of Joint Wall Compressive Strength (JCS) plays a crucial role for measuring the compressive impact on shear behaviour of rock discontinuities. JCS offers a broader view of shear strength by considering the inherent strength of rock material itself, apart from its surface texture. A lower JCS, indicative of inherently weaker rock material, limits the joint's capacity to bear shear stress, regardless of its roughness (JRC). Studies have shown that discontinuities with rougher surfaces yet lower JCS are more susceptible to damage under shearing conditions than those with smoother surfaces but higher JCS. (Barton & Choubey, 1977; Bandis et al., 1983). This underscores the critical nature of JCS in understanding the overall stability and strength of rock joints. Tensile forces also play a critical role, potentially causing more damages to the rock's asperities than compressive forces (Tang & Wong, 2016; Zhang et al., 2016). While JCS for fresh rock surfaces is typically measured through compressive strength tests, for weathered surfaces, methods like the Schmidt Hammer Index test are common (ISRM, 1978), though they come with certain limitations in precision.

- **Boundary condition effects:**

The shear behaviour of rock discontinuities can be analyzed under two types of boundary conditions: CNL (Constant Normal Load) and CNS (Constant Normal Stiffness). CNL condition is suitable for planar and non-reinforced discontinuities where dilation is unrestricted. In contrast, CNS condition is applicable to reinforced and non-planar rock discontinuities, particularly when dilation is constrained by the surrounding rock mass (Shrivastava & Rao, 2015). Reinforcements such as rock bolts, anchors, or other stabilizing structures, effectively increase the boundary's stiffness and impact the shear behaviour of the rock. Under CNS condition, stiffer boundaries tend to show increased resistance to shearing. Given that rock joints typically exhibit non-planar characteristics and are often reinforced to enhance stability, examining shear behaviour under CNS condition provides a more accurate representation of their behaviour. This correlation between stiffness and shearing behaviour has been explored by several researchers, indicating a shift in rock behaviour from brittle to ductile as stiffness increases (Heuze, 1979; Jiang et al., 2004).

- **Role of normal stress on discontinuity's surface:**

The shear strength of rock discontinuities significantly depends on the normal stress applied to them. Patton (1966) conducted tests on artificial sawtooth joints under a Constant Normal Load

(CNL) condition and identified a two-part shear strength envelope, with one part describing asperity sliding (Equation 2.2) and the other asperity shearing (Equation 2.3),

$$\tau_{p(CNL)} = \sigma_{n(CNL)} \tan(\phi_b + i_0) \quad (2.2)$$

$$\tau_{p(CNL)} = c + \sigma_{n(CNL)} \tan(\phi_b) \quad (2.3)$$

where, $\sigma_{n(CNL)}$ = normal stress under Constant Normal Load condition, τ_p = peak shear stress, c = cohesion intercept, ϕ_b = basic friction angle, and i_0 = initial asperity angle.

In his findings, Patton noted that asperities slide under low normal stress, but when the stress exceeds a certain level, asperities are sheared through. Contrasting with Patton's findings, researchers like Barton (1973) and Maksimovic (1996) proposed that sliding and shearing can occur together, leading to different strength envelopes. It is noted that at lower to medium normal stresses, Patton's model tends to predict higher peak shear strengths than what is actually measured. Barton (1973) proposed a nonlinear strength envelope specifically for nonplanar rock joints under constant normal load (CNL) condition (Equation 2.4).

$$\left(\frac{\tau_p}{\sigma_n}\right)_{CNL} = \tan\left(\phi_b + JRC \log_{10}\left(\frac{\sigma_c}{\sigma_{n(CNL)}}\right)\right) \quad (2.4)$$

where, σ_c = uniaxial compression strength, $\phi_b = \phi - (d_n + s_n)$, d_n = the peak dilation angle, which shows a decrease when there is an increase in normal stress, and s_n = the asperity shear angle which shows an increase when there is an increase in normal stress due to more surface degradation.

Indraratna and Haque (1997) found that the shear behaviour of soft joints under Constant Normal Stiffness (CNS) shows notable differences from the usual patterns observed under constant normal load (CNL) conditions. In CNL tests, the dilation measured is always higher than in CNS tests. This means CNL data may not accurately capture the peak shear stress of joints. The CNS tests reveal a nonlinear shear strength envelope for soft joints, unlike the bilinear envelope observed in CNL tests. It is noteworthy that before reaching peak shear stress, the stress paths in CNS tests generally follow the strength envelope, particularly at low to medium initial normal stresses. Similarly, Skinas et al. (1990) also observed comparable results with joints made of sand, barytes, and cement. However, it is important to note that these materials are typically associated with harder rock types, rather than soft joints.

- **Role of shearing rates:**

The way rock breaks or deforms under shear stress is closely linked to how quickly the shearing happens. Generally, when you shear hard rocks quickly, they tend to lose strength, but soft rocks might get stronger with speed, at least until a certain rate. The work by (Crawford & Curran, 1981; Haque, 1999; Atapour & Moosavi, 2013) investigated this phenomenon and discovered that as you increase the shearing rate, initially, there is more resistance from the rock, and it can handle more stress. However, beyond a certain rate, this effect does not sustain, and the rock's resistance starts to decline.

- **Humidity effects:**

Barton (1973) delved into how water affects the shear strength of rock discontinuities, finding that moisture typically weakens rough discontinuities by reducing the tensile strength of the materials. However, if the discontinuities are polished and only slightly damp, their shear strength can be maintained or even increased. Zandarin et al., (2013) used a modified direct shear device for controlled relative humidity testing on rocks with discontinuity. Results indicated a strong correlation between peak shear stress, dilatancy, suction, and joint roughness, though with a limited effect on residual strength. They also observed less degradation of discontinuities with increased suction.

The study experimentally investigated the impact of suction on rock joint behaviour. A direct shear device was modified for controlled relative humidity testing, enabling the assessment of roughness effects on shear strength and dilatancy in rock joints. Results indicated a strong correlation between peak shear stress, dilatancy, suction, and joint roughness, with higher roughness resulting in greater shear strength and more brittle behaviour.

- **Over-consolidation ratio effects:**

Barton, (1973) noted an increase in shear strength as the over-consolidation ratio rise. Bandis et al., (1983) discussed the discontinuity over-closure effect on shear resistance due to stress history. As the Over-Consolidation Ratio (OCR) or Joint Over-Closure (JOC) values rise, the joint surfaces stick more together. This increased interaction boosts peak shear strength, the angle of dilation, and the stiffness of the material, as well as steepening the post-peak slope and increasing the asperity damaged area (Babanouri et al., 2011).

2.2.2 Shear Strength of Infilled Rock Discontinuities

When soil-like materials fill the discontinuities in rocks, it is necessary to consider several factors that are not relevant to the clean rock discontinuities.

- **Infill thickness effects:**

The shear strength of infilled joints is substantially affected by the thickness of the infill material. (Goodman, 1970) was the pioneer in examining how the thickness of the infill impacts joint strength, specifically investigating the ratio of infill thickness to the average height of asperities (*t*/*a*). Through direct shear tests on saw-toothed discontinuities filled with crushed mica, it was observed that a reduction in (*t/a*) ratio corresponded to a gradual decline in both shear stiffness and strength. Following this initial study, numerous researchers have explored the t/a ratio's effect on the mechanical properties of infilled discontinuities (Barton, 1974; Phien-Wej et al., 1990; Ladanyi & Archambault, 1977; De Toledo et al., 1993; Papaliangas et al., 1993; Haque, 1999). For discontinuities with various *t/a* ratios, (De Toledo et al., 1993) discovered a specific (*t/a*) ratio that separates areas where the infill has an impact from those where it does not. Noting that the critical value is dependent on the discontinuity's geometry and the particle size of the infill material. (Haque, 1999) expanded the research on the *t/a* ratio's impact, investigating infilled discontinuities under Constant Normal Stiffness (CNS) conditions. They carried out CNS direct shear tests on discontinuities filled with bentonite and found that shear strength could drop by up to 50% with just a thin infill layer. They also noted that shear strength reduction became more gradual with thicker infill, but this decrease became negligible once a critical (*t/a*) ratio was reached.

- **Boundary condition effects:**

The strength of a joint with infill is influenced by both the characteristics of the fill and the joint surface. In clay-filled joints, strength is affected by the alignment of particles along the contact surface, causing sliding (Kanji, 1974). Conversely, in sand-filled joints, the rolling of grains over each other becomes a significant factor, particularly when the rock surface is smoother than the sand particles, leading to reduced dilation and strength (Fig. 2). The surface roughness of the joint is a critical determinant in this interaction, and its effect varies with the soil particle size (De Toledo et al., 1993). yet further research is needed to fully comprehend the effects of boundary conditions on the strength of sand-filled joints.

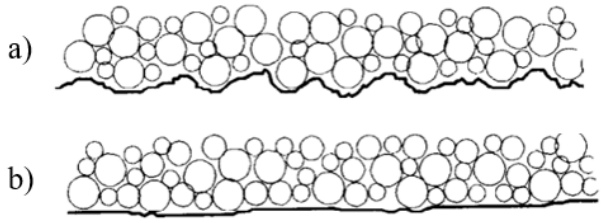

Fig. 2) Rock joint-sand filler contact: a) rough surface with no influence in the joint strength; b) smooth surface with weakening of the joint (De Toledo et al., 1993).

- **Water content effects:**

(Goodman, 1970) research on the impact of moisture within clay infill on shale discontinuities revealed that under dry conditions, there was notable initial stiffness and a significant variance between peak and residual strengths in the shear stress outcomes. However, as moisture content in the infill increase, there was a marked decline in shear stiffness. Depending on the infill's relative thickness, the post-peak behaviour exhibited either strain-hardening or strain softening (Fig. 3).

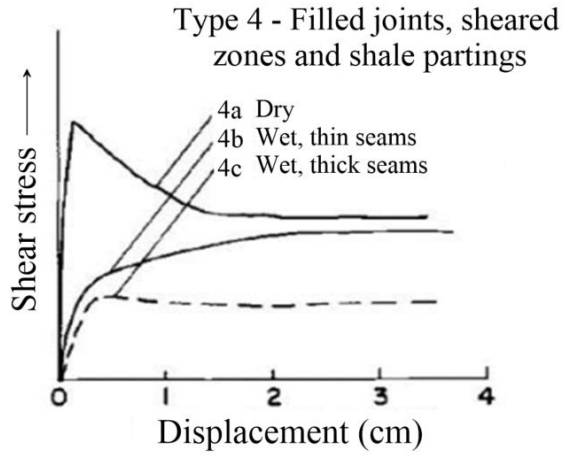

Fig. 3) Influence of infill water content on the relationship between shear and displacement for filled discontinuities (Goodman, 1970).

Saturation significantly reduces the friction angle and cohesion of discontinuity materials in clay rocks (Pellet et al., 2013). As the saturation or water content in the infill increased, there is a corresponding decrease in the discontinuity's peak shear strength (Premadasa & Wuditha N, 2013). According to the strength model they proposed, a higher infill degree of saturation resulted in a lower cohesion intercept and a larger critical (t/a) value, while also reducing the influence of the discontinuity's asperities on the total friction angle.

- **Effect of over-consolidation ratio:**

By interpreting the results on infilled rough discontinuities on shear behaviour, as the over-consolidation ratio of the infill increased, there is a reduction in both the critical (*t/a*) ratio and the excess pore water pressure during shearing, while the normalized shear strength exhibited an increase (Mylvaganam, 2007).

2.3 Post-Rupture and Residual Strength

The 1964 Rankine Lecture triggered significant interest in the shear strength of clays at large strains, leading to a focused research effort on the engineering properties of Keuper Marl. This research included measuring the residual strength of Keuper Marl using triaxial tests with preformed planes, as proposed by Skempton (1964), alongside traditional reversal shear box techniques. Prior to applying the triaxial technique, it was necessary to address rapid changes in the cross-sectional area due to increasing axial strain and the effects of the rubber membrane. The methodologies developed for Keuper Marl may offer broader applicative insights.

To measure residual strength, a shear plane was pre-formed in the sample at an angle of 45 degrees plus half the expected residual angle of shearing resistance. Findings indicate that small deviations in the angle of the shear plane do not significantly affect the measured values of residual shear strength. Corrections for changes in contact area and constraints imposed by the rubber membrane have proven valid up to 12% axial strain. These adjustments allow for reliable strength measurements across the shear plane of triaxial samples with pre-formed failure planes. The capability to reconsolidate samples at higher cell pressures after achieving small strains to maximum stress has been utilized to establish multiple points on the residual strength envelope, enhancing the understanding of the material's behaviour under varying conditions (Chandler, 1966).

In the study by Burland (1990), the intact strength properties of two heavily over-consolidated undisturbed clays, a low plasticity clay from Todi, Italy, and high plasticity London Clay from Ashford Common, were explored. The research demonstrated that for both types of clay, the intact failure surfaces are positioned above the intrinsic Hvorslev surfaces, highlighting the enhanced strength attributable to the natural microstructure of the soils.

Both clays exhibited brittle behaviour under low and intermediate stresses, leading to the formation of shear surfaces at peak intact strength. The strength on these shear surfaces decreased rapidly to a steady post-rupture strength after only minimal relative displacement, a

phenomenon distinct from the residual strength that is observed after much larger displacements.

The findings show that at lower stresses, the post-rupture failure envelopes and intrinsic critical state failure envelopes of both clays are closely aligned (Fig. 4). However, at higher stresses, the post-rupture strengths fall below the intrinsic critical state strengths, suggesting further investigation is needed into the phenomenon of post-rupture strength in other intact materials and its comparison with intrinsic critical state strength.

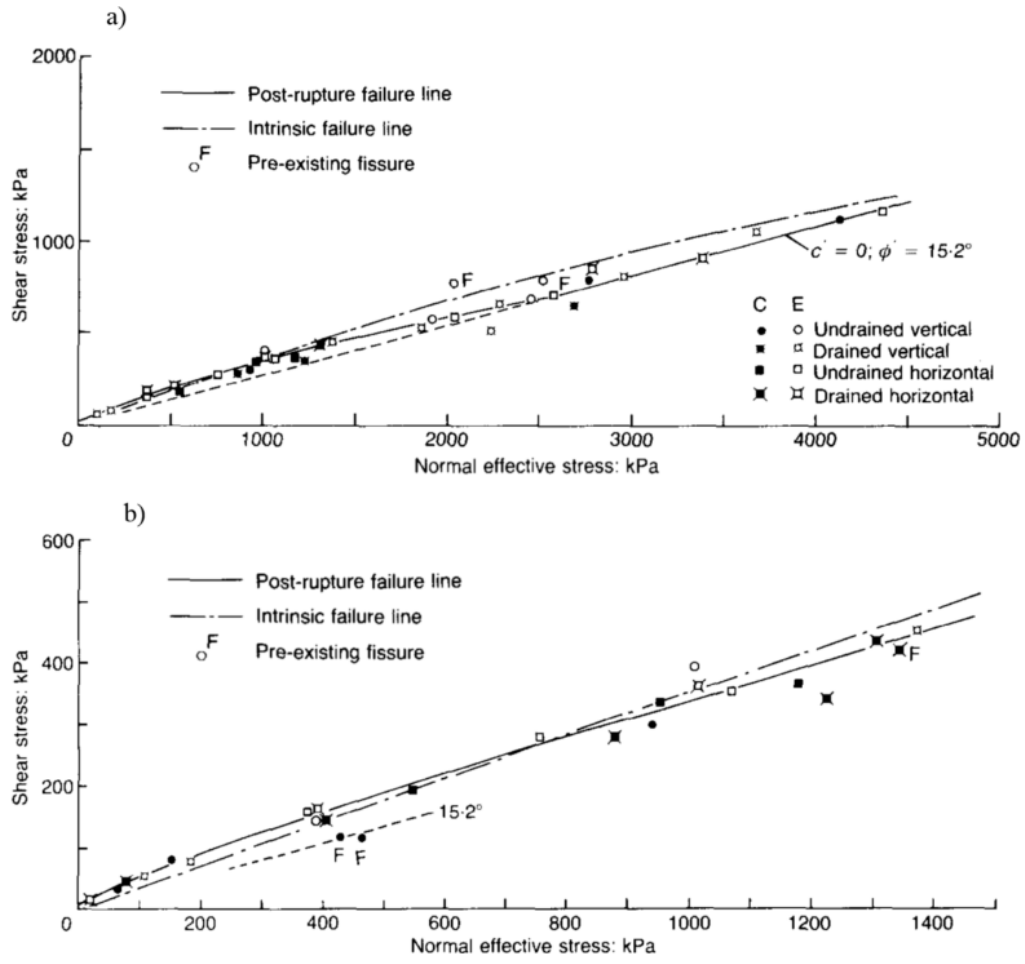

Fig. 4) Ashford Common: post-rupture failure envelopes for a) high pressures and b) low to medium pressures compared with the intrinsic failure line (Burland, 1990).

Moreover, the study also evaluated the strengths of samples containing pre-existing fissures. Most tests indicated that the strengths on these fissures were close to the post-rupture strength of initially intact specimens, though some results were slightly lower, establishing a well-defined lower limit to the fissured strength, particularly for London Clay.

In the study conducted by Georgiannu and Burland (2001), a comprehensive examination of the post-rupture strength of natural stiff clays was undertaken, focusing on the behaviour of

clays at low to intermediate confining pressures which typically exhibit very brittle shearing. This brittle shearing results from strain localization at around peak strength and thereafter involves approximately rigid block sliding along the resultant slip surface. The shear strength drops rapidly from peak intact strength to a reasonably constant post-rupture strength after only minimal relative displacement across the slip surface. This post-rupture strength is distinct from the residual strength, which is generally lower and requires substantially larger displacements to develop.

Their investigations revealed that the post-rupture strength of natural stiff clays closely aligns with or lies slightly above the intrinsic critical-state strength envelope at lower stresses but tends to fall below it at higher stresses. This behaviour was consistent across various tests, suggesting a strong influence of bonding and microstructural changes on the post-rupture strength. The rapid post-peak loss of strength is attributed mainly to changes in the microstructure, particularly the breaking of interparticle bonds, which is often accompanied by local dilation near the developing slip plane. This finding is consistent with the observations that even at large strains, the behaviour of natural clays can differ significantly from their reconstituted counterparts due to inherent structural differences.

The study by Georgiannou and Burland (2001) highlights the complex interactions between the microstructural characteristics of clays and their mechanical behaviour under stress, providing valuable insights into the post-rupture phenomena in stiff clays and underscoring the need for further research into this area to better understand the mechanisms driving these behaviours in geotechnical applications.

In evaluating the stability of slopes, the importance of understanding the drained residual shear strength of cohesive soils, especially concerning pre-existing slip surfaces, is crucial. Typically, the reversal direct shear test is employed to measure this strength in clays and clay-shales; however, it has limitations, most notably its inability to apply continuous shear in one direction. This limitation prevents full alignment of clay particles along the shear direction and may not accurately reflect the soil's true residual strength.

A more effective alternative is the torsional ring shear apparatus, which shears the specimen continuously in one direction, allowing clay particles to orient parallel to the direction of shear and thus develop a true residual strength condition. This apparatus maintains a constant cross-sectional area throughout the test, requires minimal supervision, and integrates well with data acquisition systems.

Research conducted by (Stark and Eid, 1994) using the torsional ring shear apparatus on various clays and shales has demonstrated that the drained residual failure envelope is significantly nonlinear, challenging simpler models often used in engineering practice. This nonlinearity, influenced by clay mineral types and the proportion of clay-sized particles, shows that the liquid limit is a valuable indicator of clay mineralogy. Particularly for soils with over 50% clay-sized particles and a liquid limit between 60 and 220, this nonlinearity is crucial.

The study results advocate for the inclusion of nonlinear characteristics of the drained residual strength in stability analyses to mirror the actual behaviour of cohesive soils more accurately under stress conditions. A new correlation has been developed that considers the liquid limit, clay-size fraction, and effective normal stress, providing a more accurate model of the entire nonlinear residual failure envelope.

The research conducted by Tiwari and Rao (2006) utilizing triaxial and true triaxial testing on physical models of rock mass, particularly those with three continuous joint sets made from sand lime, has provided valuable insights into the post-failure behaviour of jointed rock masses. The study was performed using a True Triaxial System (*TTS*) developed by the authors, highlighting distinct behaviours such as strain hardening, softening, and plasticity influenced by joint geometry and stress conditions.

Key findings from the study indicate that the stress-strain curves of rock mass specimens with joint orientations at $\theta = 0°$, 20°, 80°, and 90° predominantly exhibit strain softening behaviour. Interestingly, as the σ_2/σ_3 ratio increases, so does the slope of the curve post-peak, which diverges from the behaviour observed in intact rocks. Moreover, under increased confining stress, the post-peak slope of these curves rises, and intriguingly, all curves converge to a point that represents the ultimate strength of the rock mass, demonstrating a rock burst phenomenon (Fig. 5).

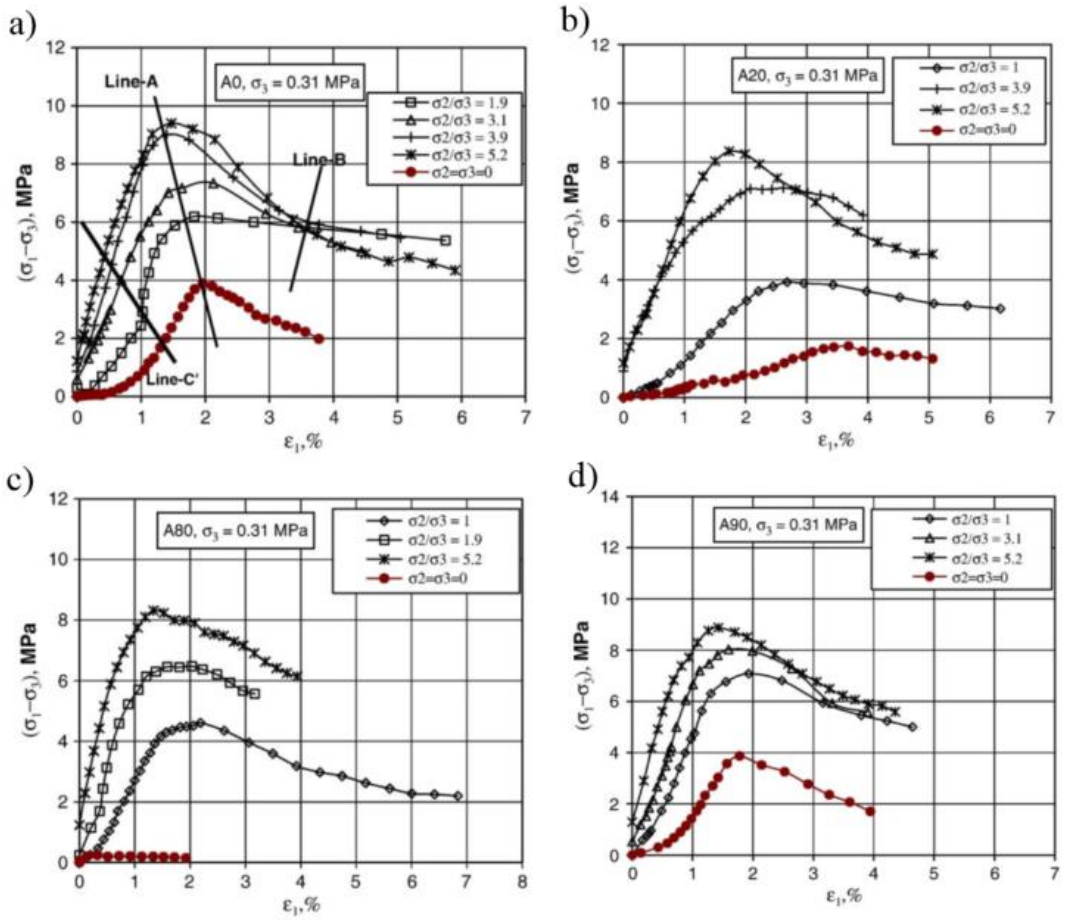

Fig. 5) Deviatoric stress-strain curves at different σ_2/σ_3 ratios for a) $\theta = 0°$, b) $\theta = 20°$, c) $\theta = 80°$, and d) $\theta = 90°$ jointed specimens at $\sigma_3 = 0.31$ MPa (Tiwari and Rao, 2006).

For joint orientations of $\theta = 40°$ and 60°, the behaviour shifts to strain hardening and plasticity, where higher σ_2/σ_3 ratios enhance the positive slope post-peak. At even higher σ_2/σ_3 ratios, however, the rock mass begins to exhibit strain softening. This indicates that while joint geometry significantly affects the rock mass behaviour under lower confinements, at higher confining stresses, the rock mass tends to display strain softening irrespective of the joint orientation.

Tiwari and Rao (2006) also developed plots based on σ_2/σ_3 ratios for different joint inclinations, drawing comparisons to earlier work by Bieniawski et al. (1969). These plots generally form straight lines, with slopes that vary according to joint geometry, providing a useful method for assessing rock mass behaviour under varying stress states (Fig. 6).

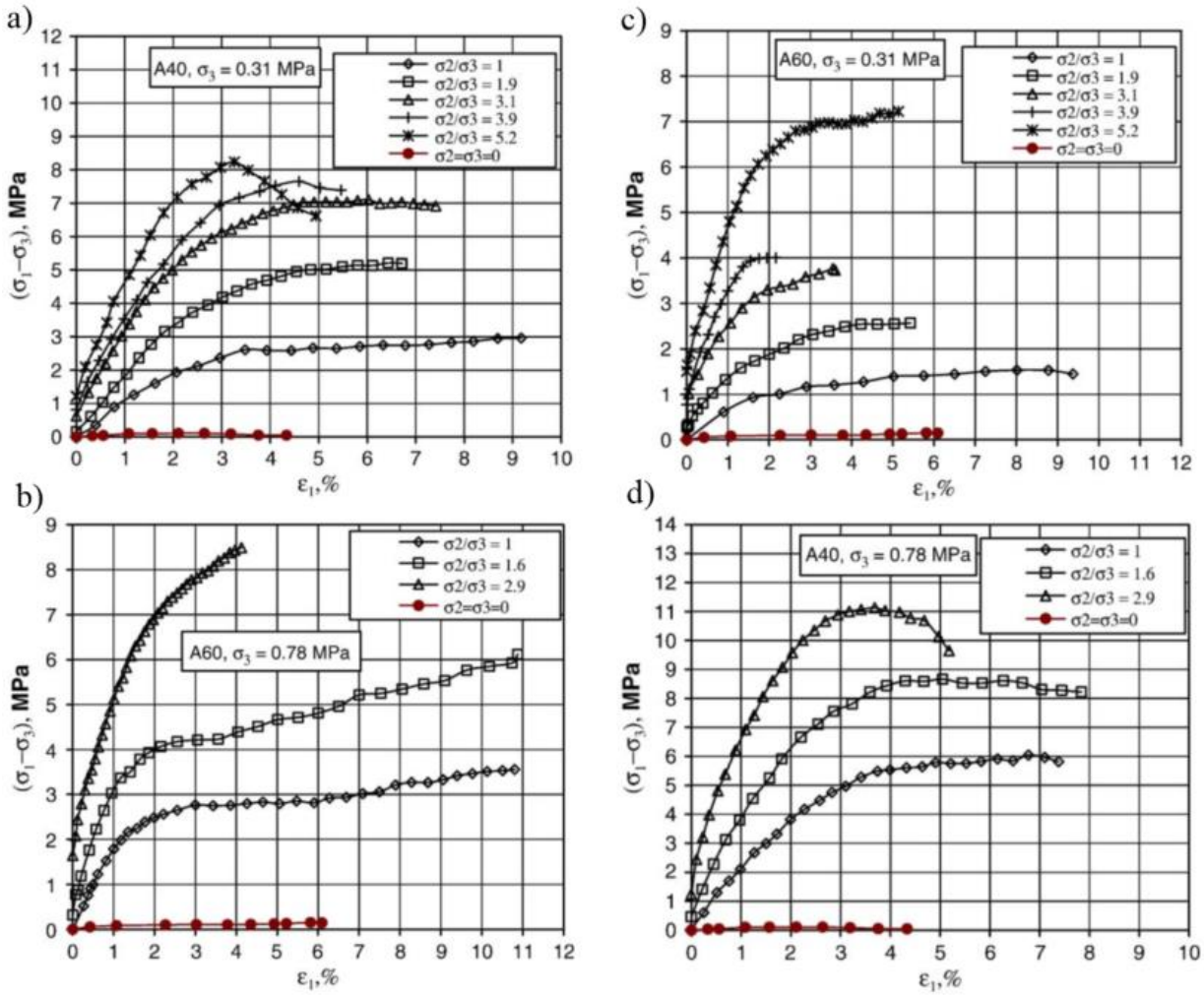

Fig. 6) Deviatoric stress-strain curves at different σ_2/σ_3 ratios for jointed specimens with $\theta = 40°$ and $\theta = 60°$ at a, c) σ_3 = 0.31 MPa, and b, d) σ_3 = 0.78 MPa (Tiwari and Rao, 2006).

The study notably suggests expressions to estimate the post-peak modulus under both triaxial and true triaxial stress conditions and proposes a zonation table that assists in evaluating the strain behaviours - hardening, softening, and plasticity - of rock mass materials, based on joint geometry and onsite confining stress conditions.

The study conducted by Stark and Hussain (2010), investigates the relevance of drained residual shear strength in analyzing slopes with pre-existing shear surfaces. Utilizing torsional ring and direct shear tests, it assesses whether strength gains along these surfaces over time are substantial. Findings indicate that while strength increases above the drained residual strength are detectable at effective normal stresses up to 100 kPa, these gains are ephemeral, dissipating quickly with slight shear displacements. Therefore, for practical purposes, especially in slope stabilization, relying on these transient strength increases is not advisable. Instead, employing

drained residual strength as specified by ASTM D6467 is recommended for landslide analysis and design.

Further findings suggest that strength gains are somewhat more significant in shallow landslides or at the shallower sections of deep-seated landslides (up to 5 meters deep) but are inconsequential at greater depths. The ephemeral nature of the observed strength recovery in ring and direct shear tests, even under modest effective normal stresses, indicates a minimal economic advantage in employing these gains for the remediation of shallow landslides or the upper portions of deeper landslides. Thus, these observed strength gains hold limited practical significance for landslide remediation but may provide useful insights into the behaviour and initial stability of shallow landslides prior to reactivation. It is concluded that both shallow and deep-seated landslide designs should incorporate the drained shear strength measurements according to ASTM D6467 (Stark and Hussain, 2010).

The study focused on the strength characteristics and subsequent failure of a cut slope in stiff clay constructed for a new local road. The slope, with a steep gradient of 1:1, significantly failed four months after excavation, prompting a detailed analysis using in-situ tests and laboratory shear tests. The strength distribution of the clay, assessed through Swedish sounding and borehole tests, showed deterioration from the surface downwards, consistent with long-term weathering effects.

Laboratory experiments conducted on stiff clay samples from the site involved a series of direct shear tests, modified to simulate varying degrees of weathering by controlling water absorption. It was found that increased water absorption significantly reduced the clay's shear strength, leading to the conclusion that weathering-induced strength deterioration was the primary cause of the slope failure. This study highlighted the efficacy of using direct shear tests over triaxial compression tests for simulating weathering effects in stiff clays, aligning with the principles of the Advanced Total Stress method introduced by Mochizuki et. al., (2011). This approach directly assesses shear strength deterioration due to weathering, without the need to monitor changes in pore water or air pressure within the samples (Mochizuki et. al., 2011).

The research conducted by Tutluoglu et. al., (2014) focuses on the characterization of post-failure behaviour of intact rocks under unconfined compression, which is critical for modelling the failed state around structures. The study emphasizes the necessity of stiff servo-controlled testing systems to accurately capture data in the post-failure region, which is less commonly documented compared to pre-peak and peak state parameters. The objective was to establish a

relationship between well-known pre-failure parameters such as tangent modulus (E_i), secant modulus (E_s), and peak strength (σ_{ci}), with post-failure parameters including the drop modulus (D_{pf}), residual strength (σ_{cr}), and dilatancy angle (ψ°).

Extensive testing was conducted on a diverse range of rock types including granite, rhyodacite, dunite, and quartzite, among others, to generate complete stress-strain curves and to derive post-failure characteristics. The study revealed that the drop modulus (D_{pf}) tends to increase with the rock strength (σ_{ci}), following a power law, and the D_{pf}/E_s ratio exhibited an exponential increase with a decreasing E_i/σ_{ci} ratio (Fig. 7). Additionally, the relationships for estimating residual strength and dilatancy from pre-peak and peak parameters were found to be logarithmic and exponential, respectively (Tutluoglu et al., 2014). These insights are pivotal for understanding the structural behaviour of rocks post-failure, especially in engineering applications involving rock stability and safety assessments.

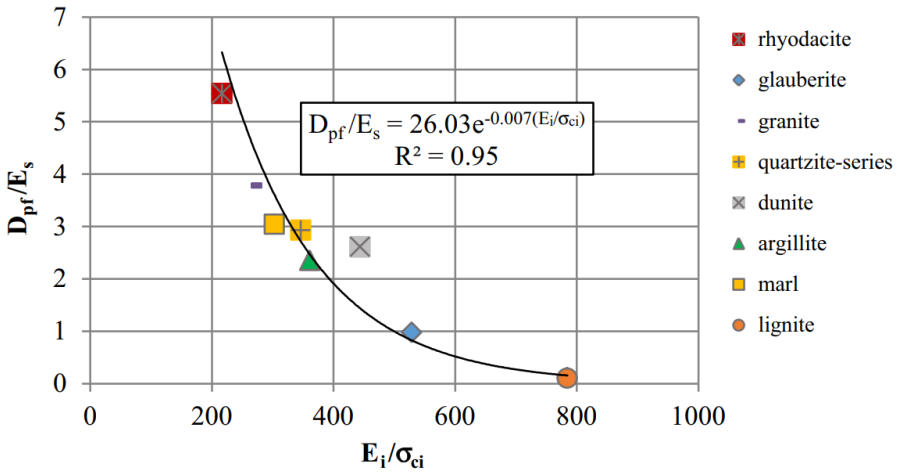

Fig. 7) Variation of D_{pf}/E_s with the modulus ratio E_i/σ_{ci} (Tutluoglu et al., 2014).

In the study conducted by Zhang and Li (2018), the concept of a Damage Index ($DI = w_r / w_{r0}$, where w_r represents the fracture energy at a given axial strain under triaxial compression and w_{r0} the total fracture energy dissipated under uniaxial compression) is introduced to assess the degree of damage in Class I rocks like Fauske marble during the post-peak stage of triaxial testing. This index is calculated as the ratio of the fracture energy dissipated at a specific strain during the post-peak phase of triaxial tests to the total fracture energy from uniaxial tests. The findings indicate that the *DI* at the onset of shear faulting increases almost linearly with confining stress, suggesting that damage intensifies under higher confinements.

For Class II rocks, the research highlights that upon reaching the peak differential stress, a portion of elastic energy is released. This release of excess elastic energy serves as a measure of the intensity of intrinsic strain bursts within the rock, influencing the intrinsic ejection velocity during burst events. Experimental observations on Kuru granite and Iddefjord granite revealed intrinsic ejection velocities of 4.6 m/s and 1.5 m/s, respectively, providing insight into the dynamic behaviour of these rocks under stress.

Moreover, the study explores how fracture angles in rocks vary with rock type and confining stress (Fig. 8). Data from experiments on Fauske marble and Iddefjord granite show that the fracture angle is exponentially related to the ratio of confining stress to uniaxial compressive strength, along with a material constant. It is proposed that higher confining stresses restrict the extension of wing cracks, leading to smaller fracture angles due to shorter wing crack extensions. This relationship underscores the impact of confining stress on fracture development in rocks (Zhang and Li, 2018).

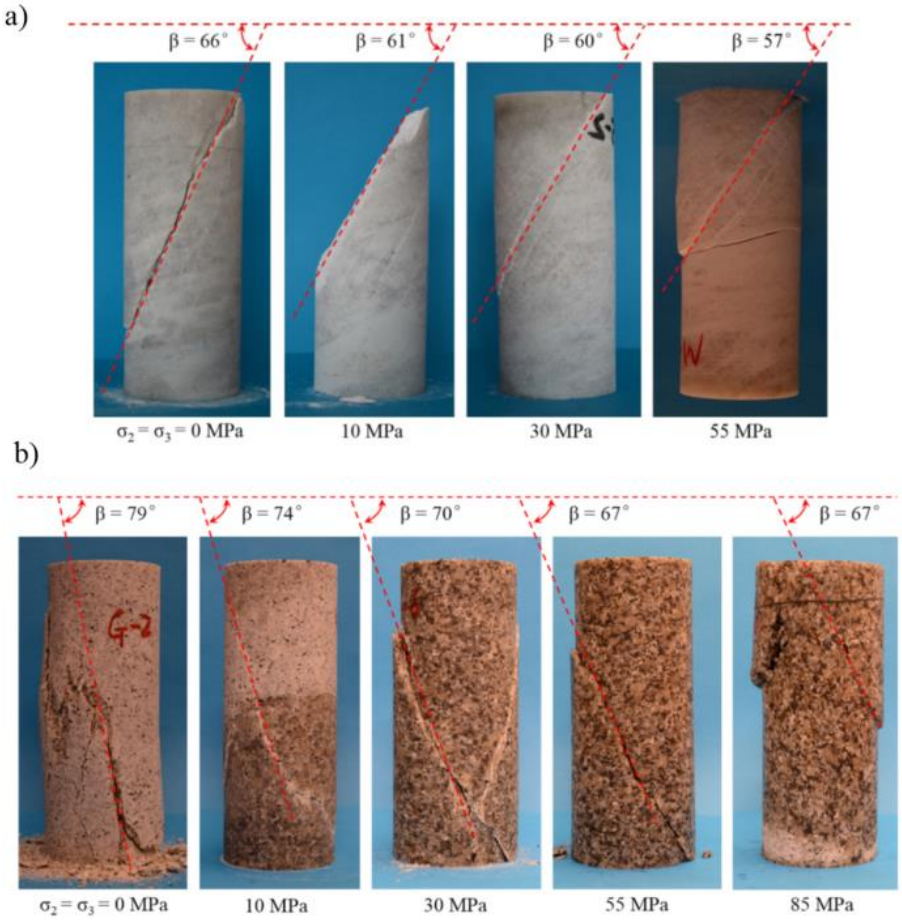

Fig. 8) Fracture angles β of specimens tested under different confining stresses for: a) marble, b) granite (Zhang and Li, 2018).

Sensitive clays undergo significant strength reduction after peak stress, crucial for understanding phenomena like landslides and mudflows. Traditional experimental methods struggle to accurately capture post-peak stress-strain behaviour, especially at high strains. This study proposes a new scientific approach to model the complete stress-strain curve for sensitive clays using data from Eastern Canada. A novel mathematical model and strain-softening equation are developed to describe the exponential and linear phases of strength reduction. This model enhances the prediction of post-failure movements in sensitive clays, proving essential for evaluating landslide susceptibility and retrogression potential. Further research is needed to refine the model's accuracy and broaden its application (Urmi et. al.,, 2023).

2.3.1 Stick-Slip Behaviour:

Stick-slip is a common frictional sliding behaviour observed in geological materials during laboratory experiments, which could potentially explain shallow-focus earthquakes. These events might occur as rocks slide along old or newly formed faults, with observed stress drops reflecting a minor fraction of the overall stress sustained by the surrounding rock.

In studying earthquake mechanisms, researchers often rely on observations of surface rock movements above the focal region and laboratory experiments on rocks under Earth-like conditions. For a while, Reid's elastic rebound theory, which posits that earthquakes result from sudden shearing motion along faults due to strain release, dominated explanations. This theory aligns with observed elastic radiation patterns from many earthquakes and is supported by laboratory experiences where stressed rocks like granite or diabase fracture and rapidly release stress through fault formation.

However, this theory has faced scrutiny, especially regarding deep-focus earthquakes. Critics argue that energy release from fracture alone is insufficient without sliding, which requires high stress, thus complicating the explanation for the typically low stress drops observed in major earthquakes.

Recent laboratory experiments have provided insights that support the Reid theory, particularly for earthquakes with focal depths less than 25 km, common in regions like California and Japan. Experiments show that rock sliding is usually jerky rather than smooth, likely due to variable frictional resistance. This jerky motion, or stick-slip, seen in various conditions and rock types, mimics the engineering phenomenon where stress builds up and releases in sudden drops, causing minimal slip each time.

Notably, even though the amplitude of laboratory stick-slips exceeds the typical stress drops of natural earthquakes, factors such as high temperature and slow strain rates seem to smooth out the sliding, potentially limiting stick-slip as an earthquake mechanism to shallow depths only. Moreover, laboratory setups might influence the occurrence of stick-slip, suggesting its potential variability under different natural conditions.

Given these insights, the stick-slip behaviour warrants consideration alongside the Reid mechanism as a plausible explanation for the generation of shallow-focus earthquakes. This phenomenon underscores the complex interaction between geological materials and mechanical conditions, highlighting the need for further research to understand its implications fully (Brace and Byerlee, 1966).

Stable sliding and stick-slip are distinct phenomena observed in frictional sliding of geological materials. Stable sliding does not produce audible stress drops and appears smooth, typically generating only weak, ultrasonically detectable elastic shocks, significantly milder than those resulting from stick-slip events.

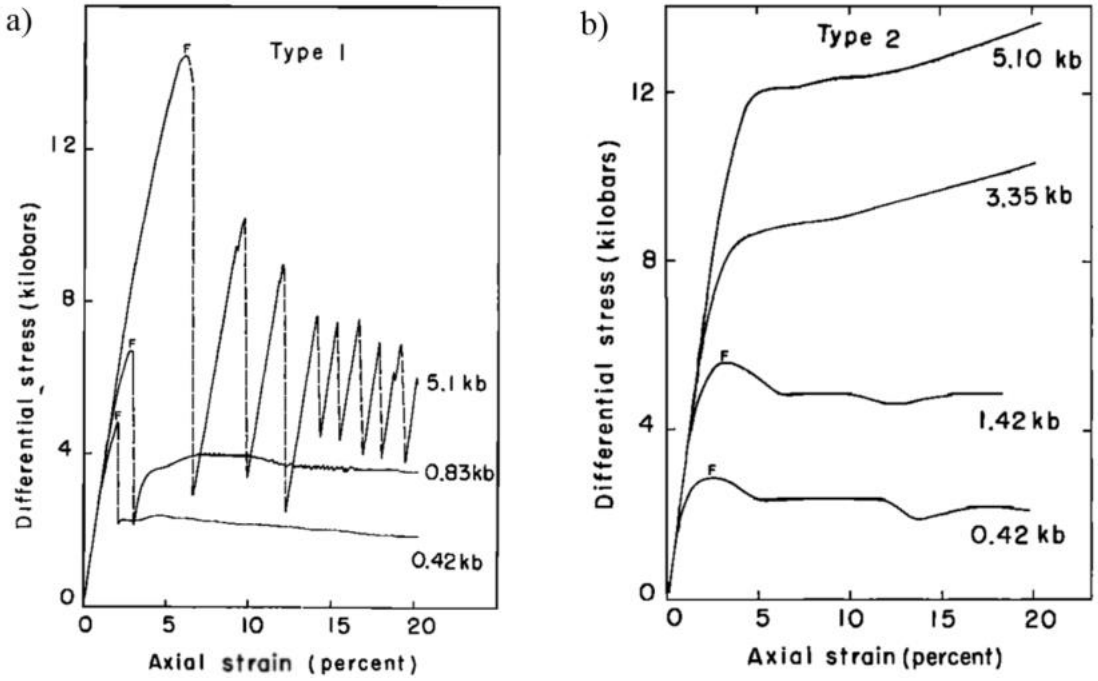

Fig. 9) Differential stress versus axial strain for a) San Marcos gabbro, b) Spruce Pine dunite. The value at the end of each curve gives the confining pressure in kilobars (Byerlee and Brace, 1968).

Different rock types exhibit varied sliding behaviours under pressure. Type I rocks demonstrate stick-slip at intermediate and high pressures with the stress drop magnitude increasing with pressure. In contrast, Type 2 rocks maintain stable sliding across all tested pressures. Once

these pressures exceed a certain threshold, rock deformation becomes more uniformly distributed without generating elastic shocks (Fig. 9).

The classification of rocks into Type 1 and Type 2 appears to be influenced by mineral composition and porosity. High-porosity rocks like tuffs do not exhibit stick-slip, nor do rocks containing minerals like calcite and serpentine. Interestingly, while certain minerals like chlorite and micas minimally affect frictional characteristics, serpentine content as low as 3% can significantly alter the frictional behaviour of rocks.

These observations suggest that the behaviour of rocks during sliding - whether resulting in steady or sudden stress drops - could vary based on the rock type and the surrounding pressure. This variability has implications for earthquake mechanics, particularly in the context of frictional sliding along fault lines.

If we consider that frictional sliding is responsible for earthquakes, the nature of the rock and the pressure conditions could dictate whether sliding results in earthquakes. For instance, Type 1 rocks may not produce earthquakes at shallow depths where stable sliding prevails but might do so deeper within the Earth where stick-slip occurs. This suggests a specific crustal zone where earthquakes due to stick-slip are likely, bounded above and below by depths where stable sliding resumes.

The interplay between different rock types along a fault line could further affect seismic activity. For example, in areas where Type 2 rocks allow for steady, visible sliding at the surface, adjacent Type 1 segments might accumulate stress until a critical threshold is reached, potentially triggering sudden, significant seismic events.

Such dynamics underscore the potential for using measurements of surface strains and tilts in seismically quiet areas - where stress accumulates in locked segments of a fault - to predict significant earthquakes. This speculative yet insightful perspective highlights the importance of understanding the mechanical behaviours of different rock types under varying stress conditions to better predict and possibly mitigate earthquake risks. (Byerlee and Brace, 1968)

2.3.2 Area Correction:

Mulabdic (1993) study focuses on the importance of correcting the cross-sectional area during triaxial shearing of firm soils that exhibit single-plane failure or zonal failure. It reviews existing methods of area correction and introduces a new approach. This assessment is based on data from soils enhanced with additives such as cement or lime. Key conclusions from the

analysis include the adjusting the cross-sectional area to reflect the specimen's shape post-testing, known as the observational approach. Corrections linearly apply to post-failure conditions based on changes in area from the failure point to the end of test. Simple corrections like cylinder, parabolic and bulging that utilize vertical and volumetric deformations are validated up to the failure point. This proposed correction method, alongside a modified version of the (La Rochelle, 1988) method that recommends a different approach for calculating ellipse diameter, provide comparable results. Utilizing these recommended corrections results in a higher measured residual strength compared to simpler methods, with the difference increasing alongside vertical strain. In their opinion, achieving residual strength typically occurs at a vertical strain of 6-8% after the failure point and running tests up to 10% vertical strain is generally sufficient to determine residual strength. These corrections are particularly effective for failure types that involve the formation of a single plane or a failure zone, to enhance the accuracy of geotechnical testing (Fig. 10).

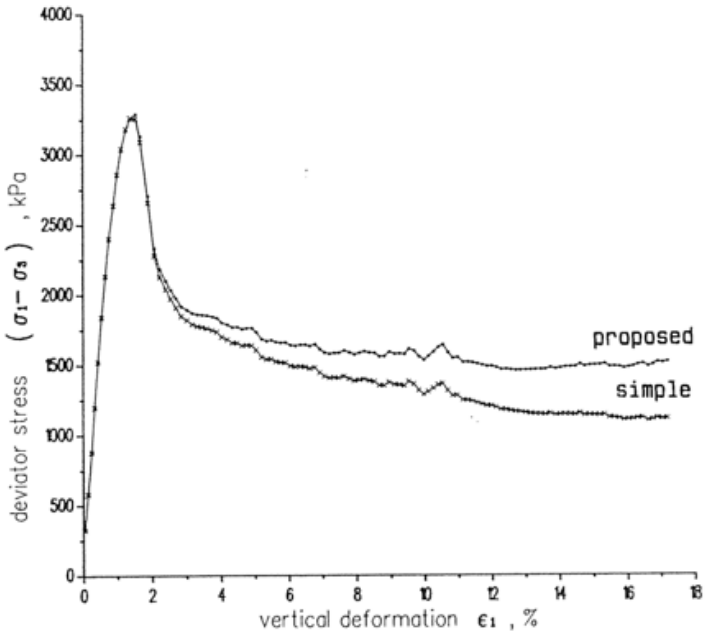

Fig. 10) Results of the CAD testing using silty clay with 10% cement, interpreted by the standard and the suggested method (Mulabdic, 1993).

2.4 Summary and Conclusion

The existing literature underscores the critical importance of accurately measuring the residual strength of clays using triaxial methods, emphasizing the need to adjust for changes in cross-sectional area, which is essential for assessing the long-term stability of slopes. Research on

over-consolidated clays, such as Todi and London Clay, reveals that intact failure surfaces surpass intrinsic Hvorslev surfaces, highlighting the natural microstructure's enhanced strength. These clays exhibit a sharp decline in strength on shear surfaces post-peak, distinctly different from residual strength, which emerges after considerably larger displacements.

Further studies using physical models of rock mass with triaxial and true triaxial testing illuminate the impact of joint geometry and stress states on post-failure behaviours such as strain hardening and softening. This insight is invaluable for predicting rock mass behaviour under real-world conditions. Additionally, torsional ring and direct shear tests demonstrate the essential role of drained residual strength in slope stability analysis, pointing out that strength gains observed in laboratory conditions may not reliably translate to long-term stability in field applications. Moreover, research suggests that stick-slip behaviour, typically observed in laboratory settings, could also be significant under natural geological conditions, potentially explaining the mechanisms behind shallow-focus earthquakes. This behaviour illustrates the complex interplay between geological materials and stress conditions, enhancing the understanding of earthquake mechanics.

In this study, the focus shifts to a detailed examination of the actual force balances and the real contact area between the top and bottom blocks of specimens during the shearing phase of triaxial testing in post-peak and post-sliding phase. Initially, this approach will be validated by comparing it with conventional methods used prior to the formation of a new failure plane (pre-peak) or before sliding onset in specimens with pre-existing failure planes (pre-sliding). Subsequent analyses will explore the period after the formation of a new failure plane in homogeneous specimens (post-peak) or after sliding onsets on pre-existing failure planes (post-sliding). The objective is to ascertain whether this innovative perspective can refine the interpretation of triaxial test data and yield deeper insights into the mechanics of soil and rock behaviour under stress.

Chapter 3

Experimental Study on Shear Strength of Saturated Clays

3.1 Details of Reference Material

In this research, Speswhite Kaolin was used to determine the shear strength of joints. Kaolin, especially a high-quality one like Speswhite, is often used as a reference material in various areas, including geotechnical engineering. The choice is based not just on its easy availability, but also on its unique qualities. These include its reliable and predictable behaviour, well-defined properties, high permeability, recognized shear strength characteristics, and its ability to be precisely reconstituted. These factors make Speswhite Kaolin a suitable material for the purposes of this research (Coduto D et al., 2011; Fernandes et al., 2023). The main geotechnical properties of the Speswhite Kaolin, represented as particle size fractions (Fig. 11), soil-specific mass ρ_s, liquidity limit w_l, plasticity limit w_p, plasticity index PI and, activity A are shown in Table 1. These main geotechnical properties were meticulously determined through experiments conducted in the Geotechnics laboratory at the University of Palermo.

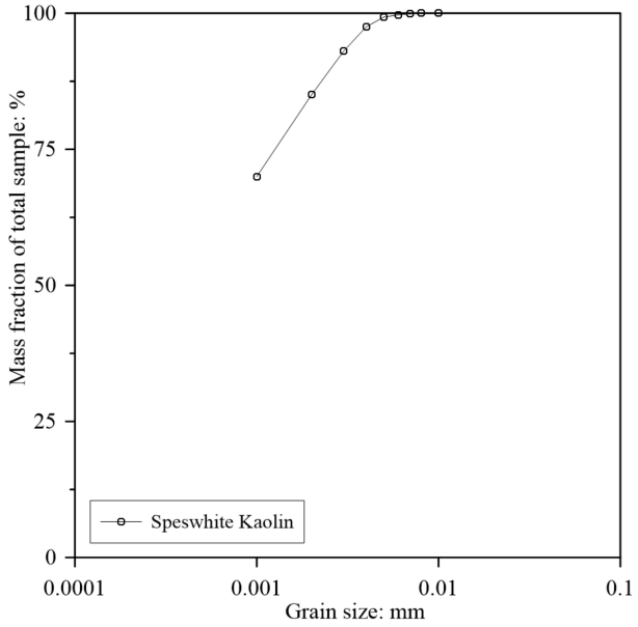

Fig. 11) Grain size distribution of the tested material.

Table 1) Geotechnical properties of the tested material.

Soil type	ρ_s	w_l	w_p	PI	A	Particle size fraction (%)		
	(Mg/m^3)	(%)	(%)	(%)	(%)	Sand	Silt	Clay
Speswhite Kaolin	2.6	58.8	31.7	27.1	0.35	0	24	76

3.2 Methodology

3.2.1 Description of the Triaxial Apparatus

The SP1 system (Fig. 12), designed for axial stress testing of cylindrical soil specimens under quasi-static conditions, comprises of three primary components: (1) a Bishop-Wesley type triaxial cell, (2) a control box housing a hydro-pneumatic pressure generation system and the electronic units for power supply, conditioning, and signal acquisition, and (3) a personal computer equipped with software for comprehensive equipment management.

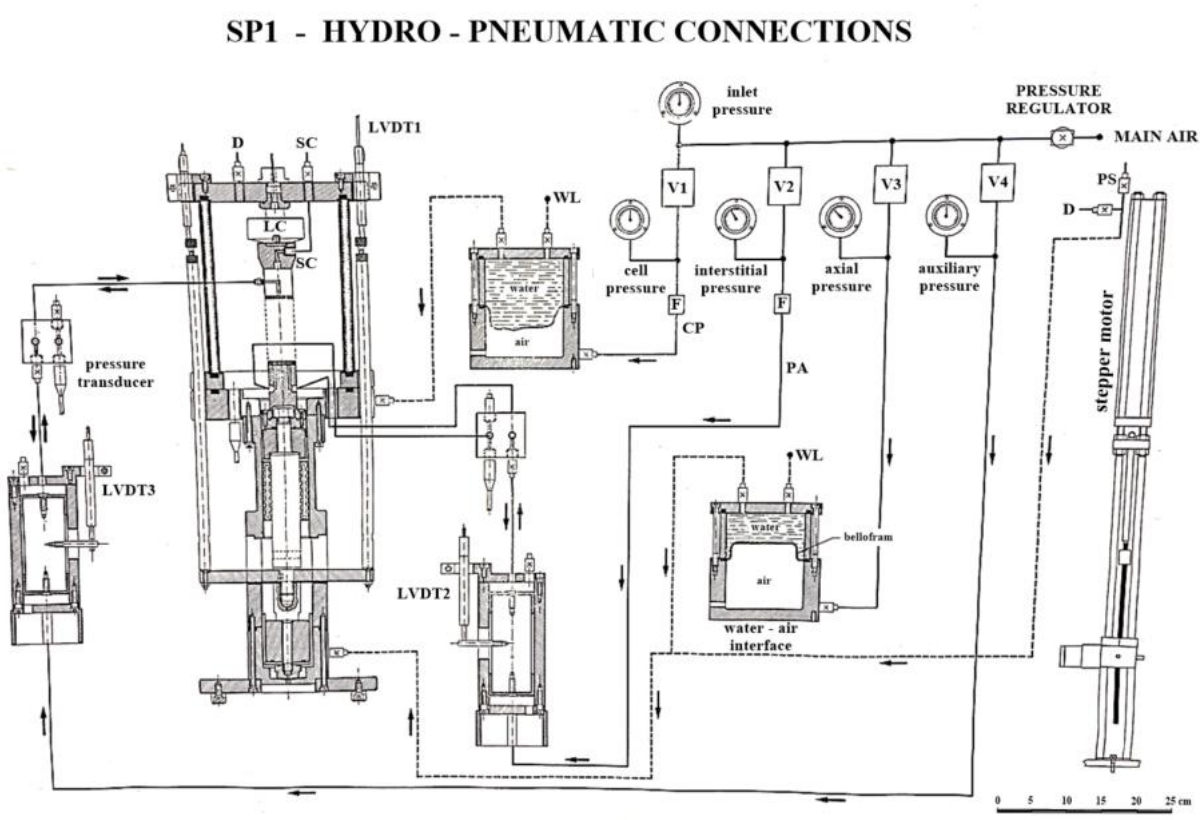

Fig. 12) Schematic view of the triaxial test device connections.

The Bishop-Wesley cell employs a hydraulic ram located in its pedestal to apply axial load, this design eliminates the need for an external motorized loading frame. The fluid supply to the ram is adjustable, allowing for a constant strain rate or load stress path, or any desired combination of axial and cell pressures. In particular, in this study, the stepper motor used for precise control of axial strain applied to the soil specimen and allows for the incremental and highly accurate axial displacement. For the tests, the stress path Bishop-Wesley triaxial cell was used, accommodating a maximum effective confining stress of σ'_c= 350 kPa. Cell pressure was generated by a bladder air-water interface system, which is powered by the 10-bar air compressor.

During the consolidation phase, drainage was permitted at both ends of the specimen. Pore water volume changes were measured in the Bishop-Wesley triaxial cells using two volume gauges, each equipped with a displacement transducer connected to the data acquisition system. This triaxial testing apparatus was used to determine the shear strength under both consolidated drained (CD) and consolidated undrained (CU) conditions.

3.2.2 Homogenous Specimens and Specimens with Pre-Existing Cut Preparation for Triaxial Testing

3.2.2.1 Densification of Reconstituted Material

In the initial phase, a slurry was prepared from Speswhite Kaolin, ensuring the water content was 1.5 times the liquid limit (Burland, 1990). To densify the reconstituted sample, a one-dimensional compression apparatus, the Consolidometer, was utilized (Fig. 13).

Fig. 13) Consolidometer; the 1D compression apparatus.

This process involved eight incremental steps in saturated condition, starting from 0.4 kPa and reaching a pressure of 320 kPa, with the objective of attaining a void ratio between 1.05 and 1.2 (Fig. 14). The entire densification process spanned approximately 20 days, allowing for each step's consolidation and precise control under the applied pressures. The unloading process was carried out under undrained conditions to ensure the sample's stability, which is essential for the successful extraction of the triaxial specimen in the subsequent step.

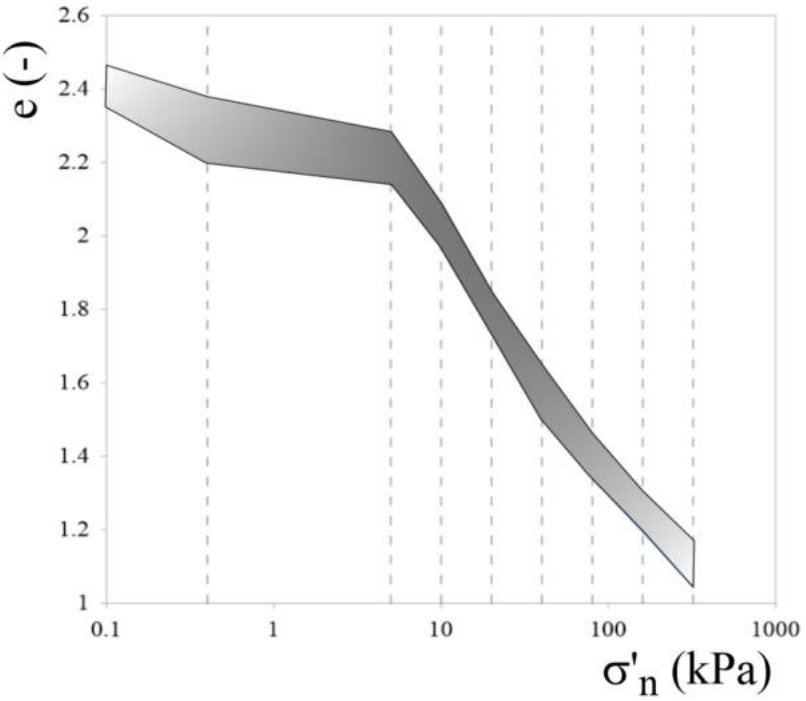

Fig. 14) Void ratio variations of the tested material during the densification process by Consolidometer.

3.2.2.2 Specimen Extraction and Installation in triaxial cell

After completing the consolidation tests, two to three cylindrical specimens, each measuring 38mm in diameter and 76mm in height, were extracted from each densified Consolidometer sample and then installed into the triaxial cell. To simulate real fault samples and analyze their shear strength and post-peak behaviour, artificial joints were introduced into each specimen before installation to triaxial cell. This involved precision cutting at various angles (0, 15, 30, 45, 60, and 75 degrees), as illustrated in (Fig. 15 and Fig. 16), using handmade holders for accurate and consistent cuts. In addition, we conducted tests on homogenous specimens without artificial joints for comparison (Fig. 16). This approach employs pre-existing failure planes to enable a detailed examination of their influence on the shear strength behaviour of the Speswhite Kaolin samples. The insights gained from these tests are anticipated to significantly contribute to understanding of fault mechanics and their responses to stress in geotechnical point of view.

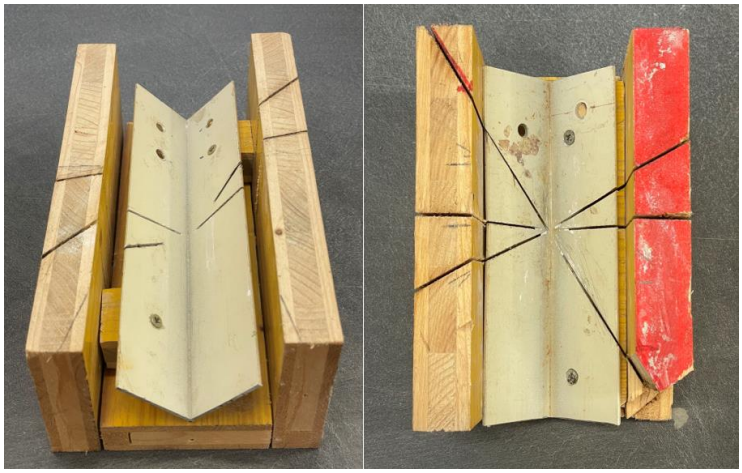

Fig. 15) Handmade holders to cut the specimens in different directions before installing into the triaxial cell.

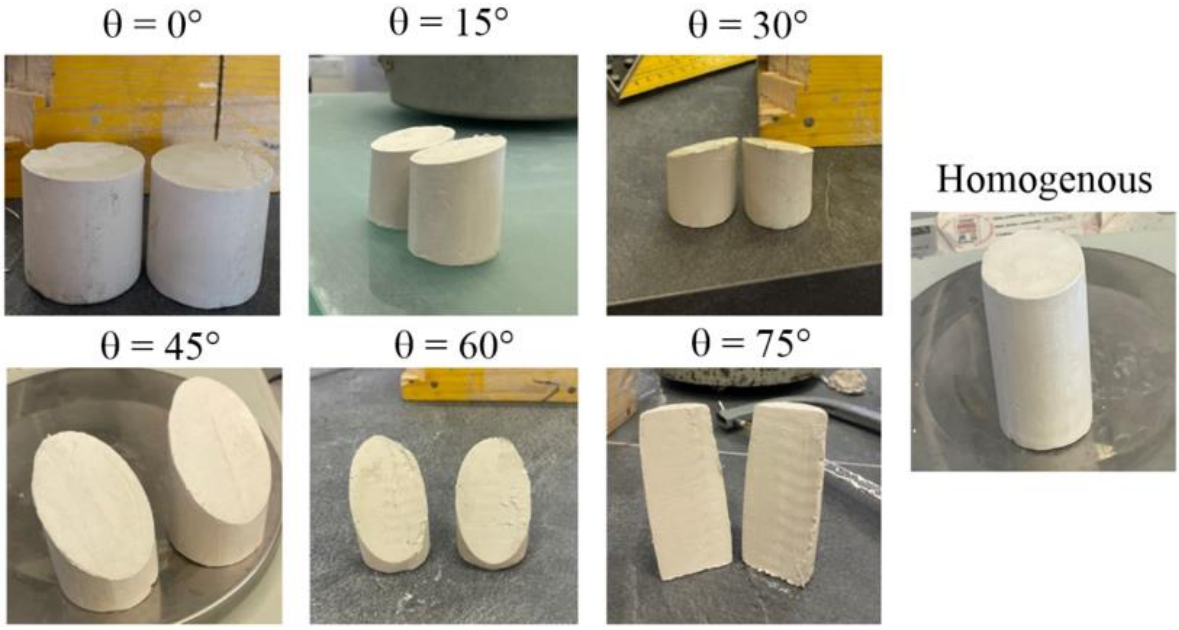

Fig. 16) Homogenous specimen and specimens with pre-existing failure plane before installing into the triaxial cell.

3.2.3 Phases of Triaxial Testing

3.2.3.1 Saturation Phase

In the saturation phase of the triaxial tests, the back pressure was employed to ensure thorough saturation of the soil specimens. This method effectively dissolves any air present within the specimen, as well as in the drainage line and pore pressure connections, enhancing test accuracy. The key advantages of this approach are (Head K. H. & Epps R. J., 2006):

1) Full saturation eliminates any separate air phase in the specimen's voids, crucial for accurate pore pressure measurements.
2) Air under the membrane dissolves, promoting uniformity across the specimen.

3) A sufficiently high initial back pressure prevents the pore pressure from falling below atmospheric levels during dilation. This is vital as it ensures that the measured pressures remain positive, critical for accurate data. The standard practice is to keep pore pressure from dropping below approximately 150 kPa.
4) In scenarios where the specimen dilates, particularly during drained tests, this method allows water to be drawn into the specimen smoothly, free from any obstruction by airlocks.

A back pressure of either 200 or 300 kPa was used, and to maintain an effective confining pressure of 40 kPa, a total confining pressure of either 240 or 340 kPa was employed during the saturation phase for both the consolidated drained and undrained triaxial tests.

3.2.3.2 Isotropic Consolidation Phase

The consolidation of a saturated specimen in a triaxial cell, an essential step before the shearing phase of both Consolidated Drained (CD) and Consolidated Undrained (CU) tests, typically follows a saturation stage to ensure full saturation, aiming for a Skempton's *B* value close to 1. In triaxial testing, isotropic consolidation is notably advantageous, ensuring uniform application of principal stresses through effective cell pressure (Lade, 2016). This method involves adjusting the effective stress by either increasing cell pressure, decreasing back pressure, or a combination of both, leading to specimen consolidation as excess pore pressure dissipates against a suitably set back pressure. Maintaining back pressure above either the final pore pressure from the saturation stage or a minimum of 300 kPa is crucial (Head K. H. & Epps R. J., 2006). In these experiments, a constant back pressure was maintained after saturation and increased cell pressure, consolidating specimens under effective confining stresses of 80, 160, and 350 kPa, suitable for both Consolidated Drained (CD) and Consolidated Undrained (CU) tests.

During the isotropic consolidation phase of triaxial testing, the precise determination of Time to Failure (t_f) is pivotal for setting the appropriate shearing rate. In drained conditions, the correct shearing rate is crucial to allow excess pore pressure to dissipate before reaching failure. Conversely, in undrained tests, the buildup of pore pressure is permitted, necessitating sufficient time for its equalization across the specimen. This time-dependent characteristic of the process is essential for ensuring precise measurements and analysis.

As detailed by Head K. H. & Epps R. J. (2006), the time for complete consolidation (t_{100}) can be theoretically deduced from the plot of volume change against the square root of time. This

is achieved by identifying the intersection point of two tangent lines: one horizontal line representing the end of consolidation, and another capturing the linear phase at the early stages of consolidation (Fig. 17).

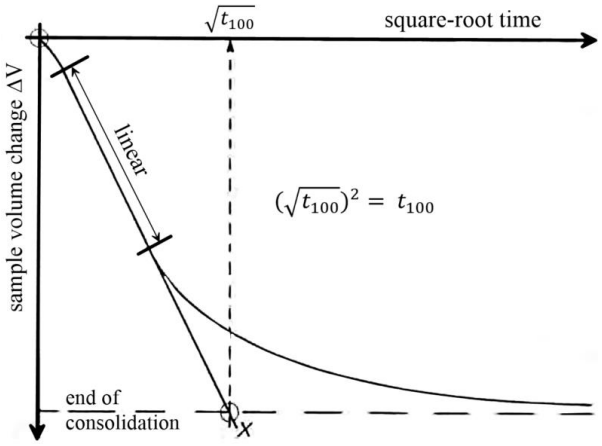

Fig. 17) Volume change versus square root time to find the time for compelete consolidation (t_{100}) (Head K. H. & Epps R. J., 2006).

By using the data from Table 2 and applying Equation 3.1, and Equation 3.2 for drained and undrained shearing conditions respectively, the time to failure (t_f) can be precisely determined for both conditions.

Table 2) Factors for calculating time to failure (t_f) (Head K. H. & Epps R. J., 2006).

Drainage conditions during consolidation	*Values of η*	*Values of λ*		*Values of F (for r = 2)*	
		L/D = 2	*L/D = r*	*Drained test*	*Undrained test*
From one end	0.75	1	$r^2/4$	8.5	0.53
✓ From both ends	3.0	4	r^2	8.5	2.1
From radial boundary only	32.0	64	64	12.7	1.43
From radial boundary and one end	36	80	$3.2(1+2r)^2$	14.2	1.8
From radial boundary and two ends	40.4	100	$4(1+2r)^2$	15.8	2.3

$$t_f = \left(\frac{5r^2\lambda}{\pi\eta}\right) t_{100} \tag{3.1}$$

$$t_f = (0.127r^2\lambda)\, t_{100} \tag{3.2}$$

In the experiments, where drainage was permitted from both ends and factors such as π, λ, η, and the specimen height-to-diameter ratio ($r = L/D = 2$) remained constant, Equation 3.1 can be simplified into Equation 3.3 for drained conditions and Equation 3.2 can be simplified into Equation 3.4 for undrained conditions.

$$t_f = Ft_{100} = 8.5t_{100} \tag{3.3}$$

$$t_f = Ft_{100} = 2.1t_{100} \tag{3.4}$$

It is also crucial to ensure that the axial strain rate does not exceed the threshold set by Equation 3.5 when determining shearing rates. This consideration ensures that the shearing is conducted at a rate that is representative of the specimen's response under the tested conditions.

$$\left(\varepsilon_f / t_f\right) \text{ (\%/minute)} \tag{3.5}$$

Where ε_f represents the strain at failure, and typical ranges of this strain at failure are illustrated in Table 3 (Head K. H. & Epps R. J., 2006). For this study, the ranges outlined for over-consolidated undisturbed clay, as presented in the figure, were used.

Table 3) Suggested failure strains in triaxial tests (Head K. H. & Epps R. J., 2006).

Soil type	*Typical ranges of strain at failure ε_f% (maximum deviator stress)*	
	CU test	CD test
Undisturbed clay		
✓ normally consolidated	15–20	15–20
✓ over-consolidated	20+	4–15
Remoulded clay	20–30	20–25
Brittle soils	1–5	1–5
Compacted 'boulder clay'		
dry of o.m.c*.)	3–10	4–6
wet of o.m.c.)	15–20	6–10
Compacted sandy silt	8–15	10–15
Saturated sand:		
dense	25+	5–7
loose	12–18	15–20

* o.m.c is optimum moisture content.

3.2.3.3 Drained Shearing Phase

In this test, water is allowed to drain out of or into the specimen while it is being sheared at a constant rate of axial deformation with the cell confining pressure remaining constant, so that no excess pore pressure (positive or negative) develops. The pore pressure remains substantially constant, but the volume of the specimen changes due to the movement of water.

Compression must be applied slowly enough to ensure that pore pressure changes due to shearing are negligible, so that the virtually fully drained condition (95% pore pressure dissipation) is applicable by the time failure is reached. The required rate of strain is usually very much slower than for an undrained test on a similar specimen under similar conditions (Head K. H. & Epps R. J., 2006).

3.2.3.4 Undrained shearing phase

In this test, no change of water content of the specimen is allowed while it is being sheared at a constant rate of axial deformation with the cell confining pressure remaining constant. If the specimen is fully saturated the undrained condition means that there is no change in its volume during compression. However, the increasing shear stresses resulting from the imposed axial load give rise to changes in pore water pressure, and therefore the effective stress changes are not equal to the changes in total stress. Compression must be applied slowly enough to allow pore pressure changes to equalise throughout the specimen by the time failure is reached. Pore pressure is measured at the base, and if the test is run too quickly the measurements will not be a true representation of the conditions within the middle of the specimen where the shear stresses have their most significant effect (Head K. H. & Epps R. J., 2006).

3.2.4 Conventional Method Interpretations

This section of the thesis explains two conventional methods for data interpretation, specifically selected to exclude considerations of plastic deformation effects. This approach is designed to facilitate a direct comparison with the sliding block method, which will be extensively discussed in Chapter 4. The early incorporation of plastic deformation effects could introduce unnecessary complexities, obscuring a clear comparison with the innovative sliding block analysis method that accounts for variations in the contact surface area between the upper and lower specimen blocks. The following subsections will detail the two foundational methods: the p'-q and τ-σ'_n stress path interpretations. In both methodologies, the soil specimen is modelled as a continuous medium throughout the shearing phase. However, this assumption introduces a notable limitation, particularly in post-peak conditions. The continuous medium hypothesis may not accurately represent the actual behaviour of the soil, especially when it undergoes significant structural changes after reaching peak strength.

3.2.4.1 p'-q Stress Path Interpretation

In the drained condition scenario, the soil is permitted to consolidate, allowing pore water pressure to dissipate without significantly affecting the soil's effective stress. This model emphasizes the relationship between deviatoric stress and axial strain, and how soil volume responds to applied stress. Key representations include plots of deviatoric stress (q) versus axial strain (ε_a), and volumetric strain (ε_v) versus axial strain (ε_a), reflecting the soil's elastic behaviour and shear strength parameters.

In contrast, under undrained conditions, soil consolidation is restricted, leading to significant changes in pore water pressure that directly influence effective stress, particularly due to the

closure of volumetric valves in triaxial testing equipment. In this context, the primary focus is on the immediate alterations in pore water pressure relative to effective stress. Therefore, essential graphical representations involve the deviatoric stress (q) versus axial strain (ε_a), and changes in pore water pressure (u_w) versus axial strain (ε_a).

The parameters tanβ and a are derived from the p'-q diagram, which plots mean effective stress (p') against deviatoric stress (q) (Fig. 18).

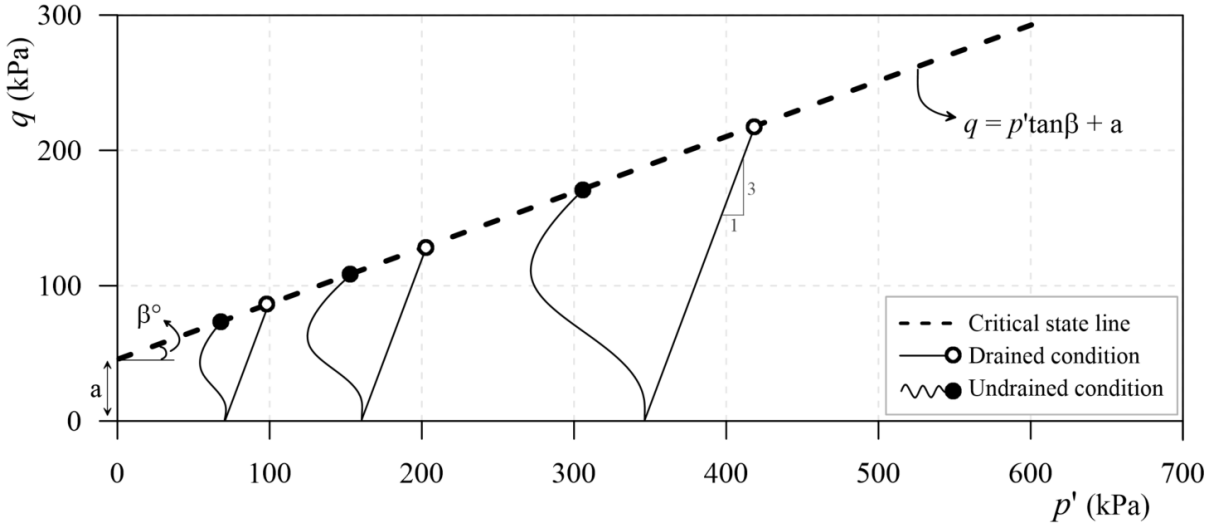

Fig. 18) Schematic view of critical state line in the p'-q space.

The parameter tanβ corresponds to the slope of the critical state line in the p'-q space, indicative of the soil's shear resistance at the critical state. Parameter a is associated with the point where the critical state line intersects the q-axis at zero mean effective stress. These parameters are calculated by analyzing shear behaviour of the soil at critical points (peak or post-peak) during consolidated drained and consolidated undrained triaxial tests. Observing the trends at these points and determining the best fit line allows for the calculation of tanβ and a, which are crucial for estimating Mohr-Coulomb parameters such as cohesion (c') and friction angle (φ'). The subsequent conversion of tanβ and a, into c' and φ', can be achieved using the following equations (3.6 and 3.7) (Favero et al., 2018).

$$\sin \phi' = \frac{3 \tan \beta}{\tan \beta + 6} \tag{3.6}$$

$$c' = \frac{a \,.\tan \phi'}{\tan \beta} \tag{3.7}$$

3.2.4.2 τ-σ'n Plane Interpretation

In the Mohr-Coulomb analysis, determining the intercept cohesion (c') and friction angle (φ') directly involves utilizing the shear stress (τ) versus normal stress (σ'_n) diagram on the failure plane. The Mohr-Coulomb criterion enables the calculation of shear and normal stresses on any plane (Fig. 19 and Fig. 20) within the soil mass (Equation 3.8 and 3.9). However, to accurately derive the shear parameters c' and φ', it is imperative to consider the orientation of the failure plane (θ) (Jaeger et. al., 2007).

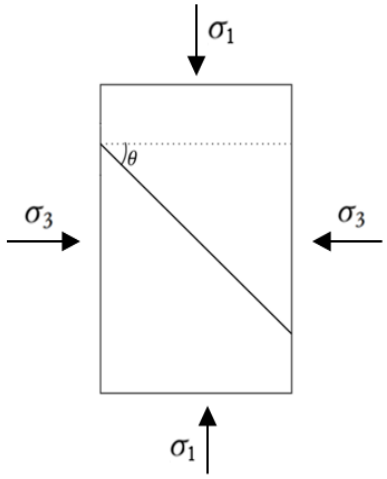

Fig. 19) Schematic view of axial and lateral stresses on the specimen before sliding starts.

$$\sigma_\theta = \frac{1}{2}(\sigma_1 + \sigma_3) + \frac{1}{2}(\sigma_1 - \sigma_3)\cos 2\theta \tag{3.8}$$

$$\tau_\theta = \frac{1}{2}(\sigma_1 - \sigma_3)\sin 2\theta \tag{3.9}$$

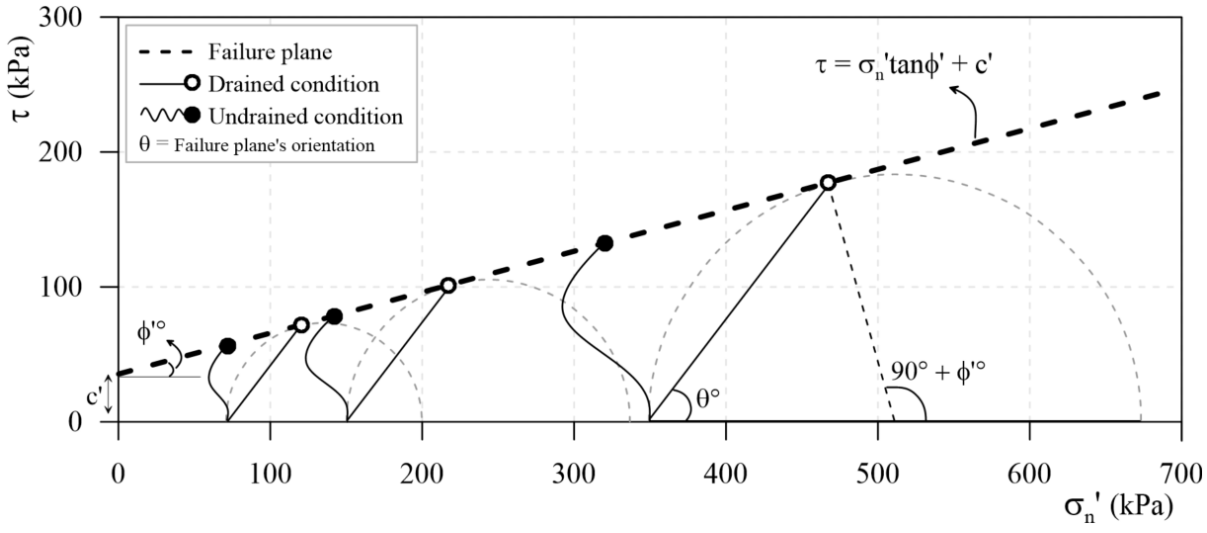

Fig. 20) Schematic view of failure envelope in the τ-σ'n plane.

3.3 Results and Discussion

3.3.1 Diagnostic Analysis

This section outlines the number of tests performed under drained and undrained conditions, and clarifies why specific tests will be highlighted in the results. Understanding this information is beneficial for grasping the scope and limitations of the experimental work, which aids in correctly interpreting the findings. The section describes all the tests that were conducted and indicates which ones were chosen for detailed analysis. Some tests were ignored because complete data collection was not possible, often due to experimental issues, as equipment malfunctions or power outages during the experiments. The selected tests for further interpretation are those that most effectively demonstrated shear strength behaviour and had successful data acquisition.

Initially, the triaxial tests were conducted under consolidated drained conditions with an effective confining pressure of 80 kPa. These tests covered both homogenous specimens (without pre-existing failure planes) and specimens with various inclinations of pre-existing failure planes (0, 15, 30, 45, 60, 75 degrees). To confirm repeatability, these tests were performed again.

Following the analysis of this test series, a new set of tests was initiated to address three challenging results (specimens with 30, 45, 60 degrees pre-existing failure plane). These challenges included sliding along the pre-existing failure plane, an unexpected post-sliding behaviour characterized by a mix of compression and sliding on the pre-existing failure plane, and the formation of new failure planes in specimens with 30- and 45-degrees artificial joints. Notably, new failure planes did not form in the specimen with 60-degree artificial joint. This new series, conducted at a higher effective confining pressure of 160 kPa, focused on pre-existing failure planes at 30, 45, and 60 degrees. It is important to note that homogenous specimens were investigated for all different effective confining pressures in both drained and undrained conditions.

The outcomes of these tests indicated that focusing on specimens with a 30-degree cut would be more effective for further investigation. This decision was based on observations that these specimens still exhibited sliding on the pre-existing failure plane and the formation of new failure planes. For the 45-degree cut specimens, the formation of new failure planes was not observed at this confining pressure. Additionally, the shear behaviour of the 60-degree specimens did not show significant variation compared to the previous test series. Therefore,

the specimens with 30-degree cuts were identified as the most challenging and consistent in terms of shear behaviour for further investigation.

Subsequently, specimens with a 30-degree cut and homogenous specimens were examined under an effective confining pressure of 350 kPa in drained conditions, and at 80, 160, and 350 kPa in undrained conditions. Below is a concise summary table of all the triaxial tests conducted in this research (Table 4).

It is important to note that specimens affected by power outages during the saturation or consolidation phases of the triaxial tests are not included in this table. The specimens ESM 81, ESM 91, ESM 111, ESM 121, ESM 122, ESM 131, ESM 132, ESM 141, ESM 151, ESM 171, ESM 172, ESM 181, ESM 192, ESM 201, ESM 211, ESM 222, and ESM 223 experienced power outages, which necessitated starting new tests with new specimens. For a complete test cycle, the densification process initially took on average, 20 days for each pair of specimens. In the triaxial tests, the average time required to saturate each specimen was 4 days, to consolidate each specimen was 2 days, and for the shearing phase, it took 7 days under drained conditions and 1 day under undrained conditions.

	Initial characteristics of specimens									Shearing phase					
Specimen	Effective confining pressure (kPa)	Pre-existing failure plane θ (°)	Diameter ×Height (mm×mm)	M (g)	γ (g/cm³)	γ_d (g/cm³)	Sr (%)	w_i (%)	Average axial strain rate (%/day)	Initial ε_v (%)	Sliding alongside the pre-existing failure plane	New failure plane formation		Final ε_a (%)	
												After sliding	No sliding		
ESM 22[1]	80	Homogenous	38.25×74.44	149.45	1.75	1.26	94	38.5	6.1	-2.17	✕		✔	26.9	CD
* ESM 51		Homogenous	38.36×75.24	145.64	1.68	1.16	93	44.4	5.9	0.43	✕		✔	12.4 PO[2]	
* ESM 62		0	37.75×74.57	145.84	1.74	1.19	100	46.4	3.4	-0.47	✕		✔	20.9	
ESM 72		0	37.83×74.17	144.50	1.73	1.20	99	44.4	5.1	-0.83	✕		✔	20.5	
* ESM 442		15	37.58×73.92	143.16	1.76	1.22	100	45.1	6.2	-1.39	✕		✔	27.0	
* ESM 61		30	37.71×74.01	143.42	1.74	1.19	100	46.4	5.4	-1.39	✔	✔		20.5	
ESM 82		30	37.57×75.04	145.76	1.75	1.21	100	44.3	2.6	0.45	✔	✔		11.9 PO	
ESM 92		45	37.37×72.87	138.95	1.74	1.20	99	44.8	3.2	0.53	✔	✔		12.6 PO	
ESM 101		45	37.94×75.27	144.58	1.70	1.16	97	46.2	5.6	0.20	✔	✔		31.0 DM[3]	
* ESM 112		45	38.13×75.06	145.96	1.70	1.15	99	47.4	4.5	-0.71	✔	✔		27.6	
ESM 52		60	37.56×76.03	146.20	1.73	1.20	99	44.4	1.8	-1.84	✔	✕		16.2	
* ESM 71		60	37.60×74.51	144.96	1.75	1.21	100	44.4	3.1	-0.68	✔	✕		16.5	
* ESM 102		75	37.93×74.94	145.02	1.71	1.17	98	46.2	3.2	-1.29	✕		✔	27.9	
* ESM 142	160	Homogenous	37.63×75.59	144.93	1.72	1.19	99	44.9	5.9	1.98	✕		✔	17.7 PO	
* ESM 161		30	37.84×76.01	145.28	1.70	1.15	99	48.2	6.4	2.67	✔	✔		19.5	
* ESM 162		45	37.88×75.60	145.15	1.70	1.15	99	48.1	5.4	2.69	✔	✕		28.4	
* ESM 152		60	37.70×75.37	146.20	1.73	1.20	98	44.1	5.5	1.76	✔	✕		23.0	
* ESM 191	350	Homogenous	37.62×74.89	143.86	1.73	1.19	100	45.8	5.0	5.38	✕		✔	21.4	
* ESM 182		30	37.68×75.64	146.30	1.73	1.19	100	45.3	5.9	5.47	✔	✔		24.3	
* ESM 221	80	Homogenous	37.39×72.98	140.60	1.75	1.22	100	44.1	21.5	-0.53	✕		✔	23.8	CU
* ESM 231		30	37.90×75.59	145.70	1.71	1.17	98	46.4	21.1	0.19	✔	✔		19.4	
* ESM 203	160	Homogenous	37.97×75.55	145.70	1.70	1.18	96	44.8	20.8	1.42	✕		✔	23.5	
* ESM 202		30	37.67×75.06	145.26	1.74	1.20	100	44.7	21.4	1.09	✔	✔		23.2	
* ESM 212	350	Homogenous	37.65×74.79	145.42	1.75	1.21	100	44.6	18.2	4.37	✕		✔	21.6	
* ESM 213		30	37.42×75.61	145.53	1.75	1.21	100	44.6	21.0	4.06	✔	✕		24.9	

*: Specimens selected for detailed analysis.

1: This specimen was densified up to 640 kPa; others up to 320 kPa.

2: Power Outage.

3: Device Malfunction occurred in some parts of the shearing phase.

Table 4) Summary of triaxial tests conducted in this study.

For a better comprehension of each step in the triaxial tests, a schematic view of the total stress path (*TSP*) and effective stress path (*ESP*) on the *p*-*q* and *p*'-*q* planes are illustrated in Fig. 21. The stress paths on the *p*'-*q* and *p*-*q* planes are identical in both drained and undrained conditions during the saturation and consolidation phases. Additionally, the *p*-*q* path during the shearing phase remains consistent across both conditions. However, in the shearing phase, the *p*'-*q* path for the consolidated drained condition runs parallel to the *p*-*q* path, this parallelism does not hold for undrained conditions. In undrained scenario, the *p*'-*q* path diverges due to the development of excess pore pressures, resulting in a non-linear path varying for each specimen. Therefore, presenting a uniform schematic view of the *p*'-*q* path during the shearing phase for undrained conditions is impractical.

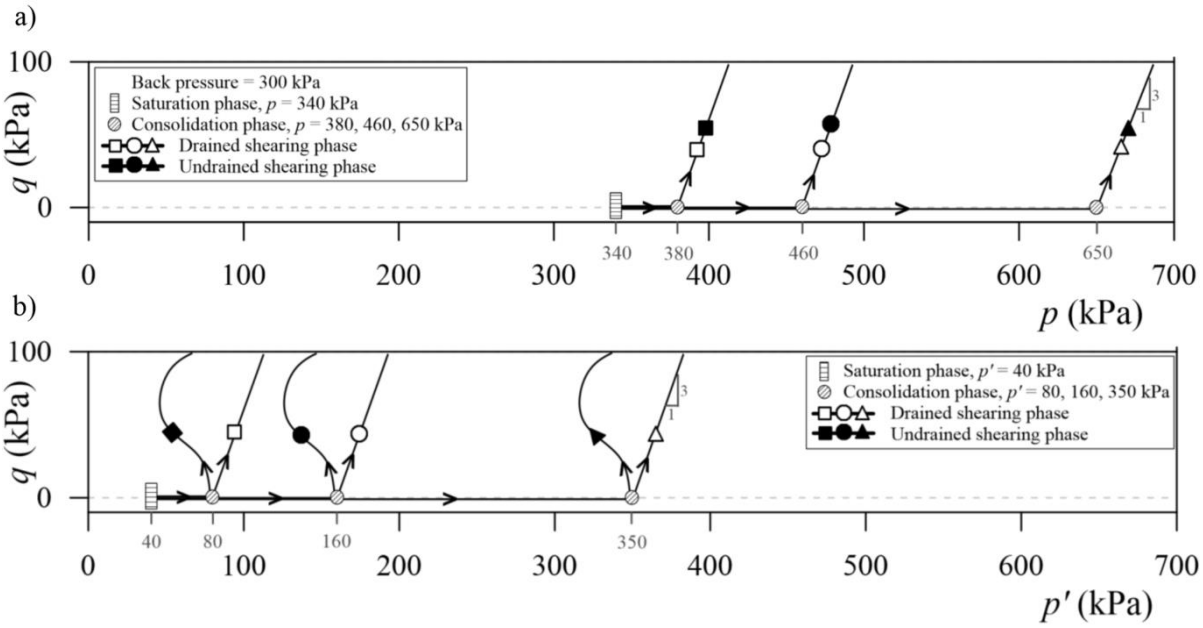

Fig. 21) Schematic view of a) total stress path (TSP) b) effective stress path (ESP).

In Fig. 16, the square, circular, and triangular symbols represent specimens consolidated under effective confining pressures of 80, 160, and 350 kPa, respectively, or under total confining pressures of 380, 460, and 650 kPa, respectively. Solid symbols indicate tests conducted under undrained conditions, while hollow symbols denote those conducted under drained conditions.

3.3.2 Saturation Phase

Compaction of Speswhite Kaolin was conducted in a saturated state using the Consolidometer (Section 3.2.2.1). After installing this densified material in the triaxial cell, confirming its saturation was crucial, as this study focused on examining the shear strength in saturated conditions. A back pressure of 200 kPa and a confining pressure of 240 kPa were applied, resulting in an effective confining pressure of 40 kPa across the specimen. The importance of

sufficient back pressure in triaxial testing was emphasized, in Section 3.2.3.1. However, a challenge was encountered when most specimens did not reach sufficient saturation levels (Fig. 22). *B*-checks indicated that a 200 kPa back pressure was inadequate for some specimens, shown by the *B* parameter consistently remaining below 0.95. Thus, for specimens not achieving a *B* parameter of 0.95 or higher, the back pressure was raised to 300 kPa and confining pressure to 340 kPa; this adjustment maintained the effective confining pressure at 40 kPa, ensuring no alteration in the concept of effective pressures. This increase was primarily aimed at enhancing water penetration into the specimen pores.

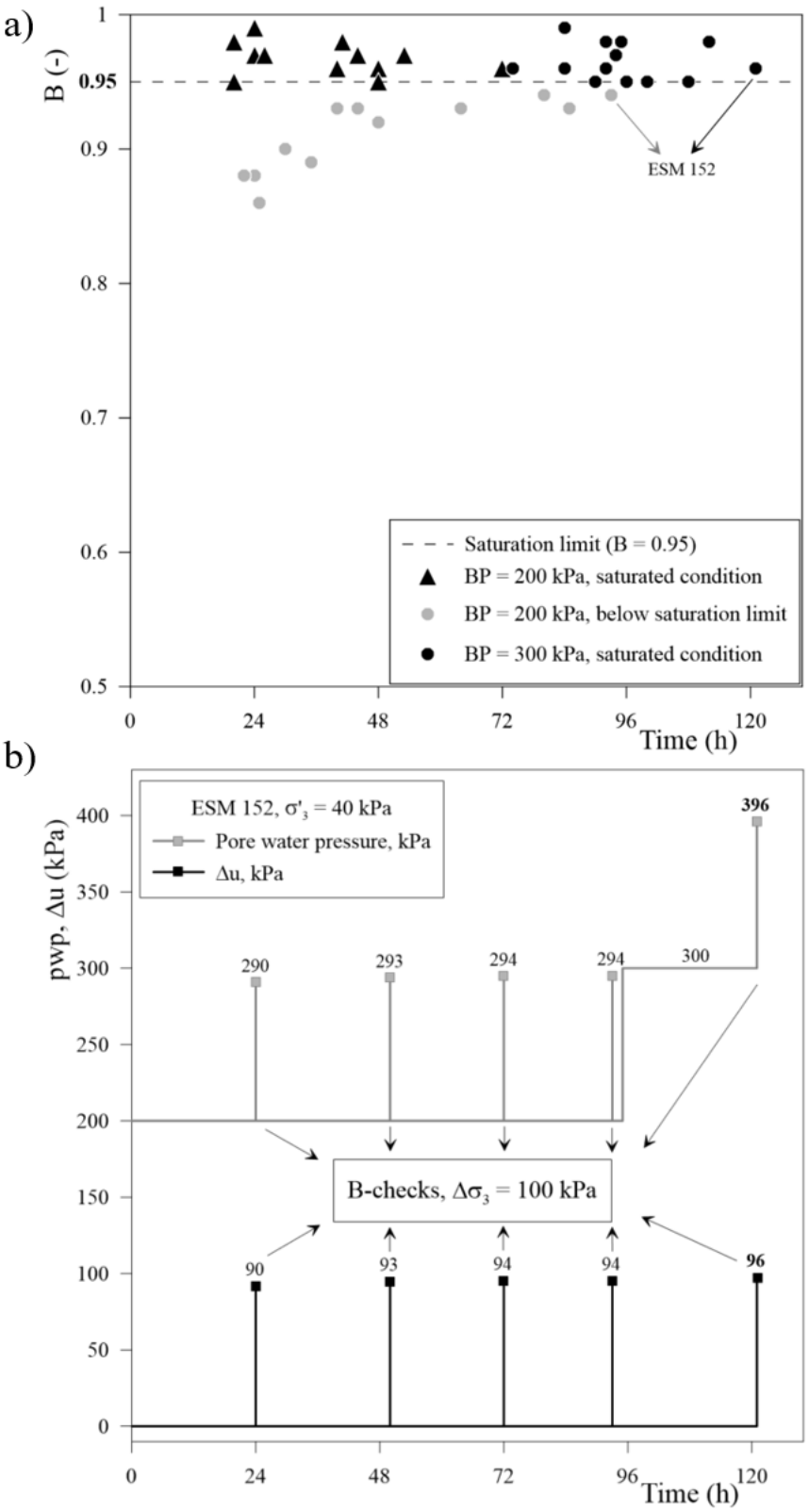

Fig. 22) a) B-checks for all the specimens in the saturation phase, b) An example of excess pore pressure and pore water pressures during saturation phase (ESM152).

In Fig. 22a, black triangles represent specimens that achieved the B parameter of 0.95 or higher under a 200 kPa back pressure. Conversely, grey circles indicate specimens that did not reach

adequate saturation, with a B parameter below 0.95. For these specimens, a back pressure of 300 kPa was subsequently applied. Once they attained adequate saturation levels, indicated by black circles, they were ready for the next phase: consolidation.

Fig. 22b displays the *B*-check intervals and the evolution of pore water pressure during the saturation phase for specimen ESM 152. The graph shows that between days 2 and 4, under a 200 kPa back pressure, the Skempton *B* parameter remained fairly constant, indicating a plateau in the saturation process. To improve the saturation level of this specimen, increasing the back pressure to 300 kPa was necessary. This increase effectively facilitated higher saturation, as demonstrated by the changes observed in pore water pressure readings during the final *B*-check interval.

3.3.3 Isotropic Consolidation Phase

Starting from this section, the primary focus will be on the specimens marked with an asterisk (*) in Table 4, involving a detailed analysis of 19 specimens. To clarify the triaxial testing plan, these specimens are categorized in two ways: The first categorization, based on boundary and shearing conditions, includes 13 specimens tested under drained conditions (Fig. 23a) and 6 under undrained conditions (Fig. 23b). The second categorization, based on the homogeneity and orientation of pre-existing failure planes, includes 6 homogenous specimens, 6 specimens with a 30-degree pre-existing failure plane, 2 specimens each with 45 and 60-degree pre-existing failure planes, and 1 specimen each with 0, 15, and 75-degree pre-existing failure planes.

After confirming the specimens' saturation (as detailed in Section 3.3.2), the consolidation stage begins. This stage involves increasing the confining pressure while maintaining the same back pressures as in the saturation phase. The consolidation analysis is presented through graphs plotting time on a logarithmic scale against volumetric change, essential for verifying that the specimens have achieved a near-steady state with minimal volumetric changes, demonstrated by attaining linearity in log time, as a requirement for progressing to the shearing phase.

Tests conducted with an 80 kPa effective confining pressure (Fig. 23) revealed slight swelling over time after reaching a steady state. This swelling could potentially be due to soil suction increasing following the compaction up to 320 kPa and immediate undrained unloading in the Consolidometer, leading to an increased tendency of the material to absorb water. The low effective confining pressure, which initially causes contraction, may not sustain it long-term,

contributing to this swelling tendency. Furthermore, these specimens did not achieve saturation at effective confining pressures below 40 kPa. The small gap between the 40 kPa in the saturation stage and 80 kPa in the consolidation stage could contribute to this swelling. However, it is encouraging that these specimens exhibited contractive behaviour in the initial stages of the shearing phase (Section 3.3.4), suggesting that the consolidation process was mostly effective. It should also be noted that the volumetric changes observed in real-time are less noticeable than those depicted on the logarithmic scale in Fig. 23.

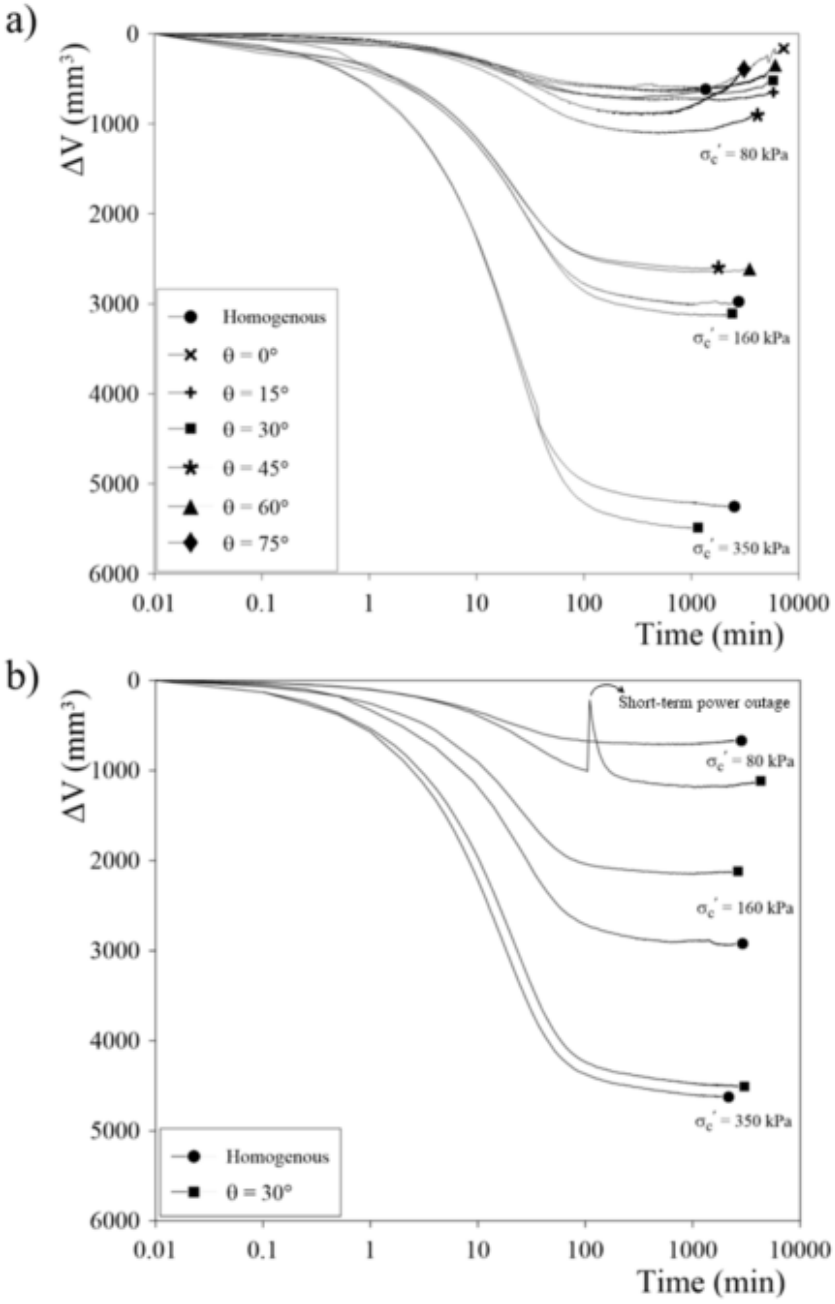

Fig. 23) Consolidation stage of a) CD tests, b) CU tests.

In Fig. 23, the consolidation phase for subsequent drained and undrained tests at 160 kPa and 350 kPa effective confining pressures is also presented. Notably, at these two higher confining pressures, the specimens do not exhibit the swelling observed at 80 kPa effective confining pressure. As time progresses, they reach equilibrium, indicating their suitability for the shearing phase. This consistent behaviour during the consolidation phase at the higher confining pressures suggests that the swelling issue previously identified has been resolved. The increased volumetric changes observed in the specimens under these higher confining pressures additionally support the reliability of the results. In Table 5, the average axial strain rate employed in this study is compared with the maximum allowable axial strain rates suggested by Head K. H. and Epps R. J., (2006), based on the t_{100} values of the specimens.

Table 5) Comparing the maximum allowed axial strain rates suggested by Head K. H. & Epps R. J., (2006) and average axial strain rate used in this study.

Specimen	Effective confining pressure (kPa)	Pre-existing failure plane θ (°)	End of consolidation t_{100} (min)	F (-)	Time to failure t_f (min)	Max. allowed axial strain rate ε_f/t_f (%/day)	Avg. axial strain rate used in this study (%/day)	
ESM 51	80	Homogenous	64	7.85	502.5	11.4	6.1	CD
ESM 62		0	64	8.07	516.9	11.1	3.4	
ESM 442		15	64	7.94	508.3	11.3	6.2	
ESM 61		30	56.25	7.87	442.7	13.0	5.4	
ESM 112		45	72.25	7.96	575.5	10.0	4.5	
ESM 71		60	56.25	8.18	460.2	12.5	3.1	
ESM 102		75	90.25	8.08	729.6	7.9	3.2	
ESM 142	160	Homogenous	64	8.63	552.8	10.4	5.9	
ESM 161		30	72.25	8.63	624	9.2	6.4	
ESM 162		45	56.25	8.41	473.4	12.1	5.4	
ESM 152		60	56.25	8.47	476.7	12.1	5.5	
ESM 191	350	Homogenous	56.25	8.33	468.6	46	5.0	
ESM 182		30	64	8.61	551.3	39	5.9	
ESM 221	80	Homogenous	49	1.84	90.3	318	21.5	CU
ESM 231		30	81	2.01	162.7	176	21.1	
ESM 203	160	Homogenous	64	2.19	140.2	205	20.8	
ESM 202		30	56.25	2.00	112.6	255	21.4	
ESM 212	350	Homogenous	49	1.98	96.9	222	18.2	
ESM 213		30	56.25	2.11	119.1	181	21.0	

3.3.4 Drained Shearing Phase

In this section, as highlighted in Section 3.3.3, the focus is on the specimens marked with an asterisk (*) in Table 4. During the shearing phase, the response of deviatoric stress to axial strains in homogenous specimens and those without sliding along pre-existing failure planes

can be categorized into three distinct conditions: 1) pre-peak, 2) peak, and 3) post-peak. Conversely, for specimens that experience sliding along their pre-existing failure planes, the response is divided into five conditions: 1) pre-sliding, 2) onset of sliding, 3) post-sliding, 4) peak, and 5) post-peak.

To clarify the shearing behaviour, an initial comparison is made between specimens without sliding along pre-existing failure planes and homogenous specimens in drained condition with 80 kPa effective confining pressure, as shown in Fig. 24. It is observed that their shearing behaviour is generally similar, with only slight differences (Fig. 24a). Due to this similarity, further investigation of these particular orientations of pre-existing failure planes was not continued. Instead, this study shifted focus to specimens with 30, 45, and 60-degree pre-existing failure planes, which exhibited distinct shearing behaviours.

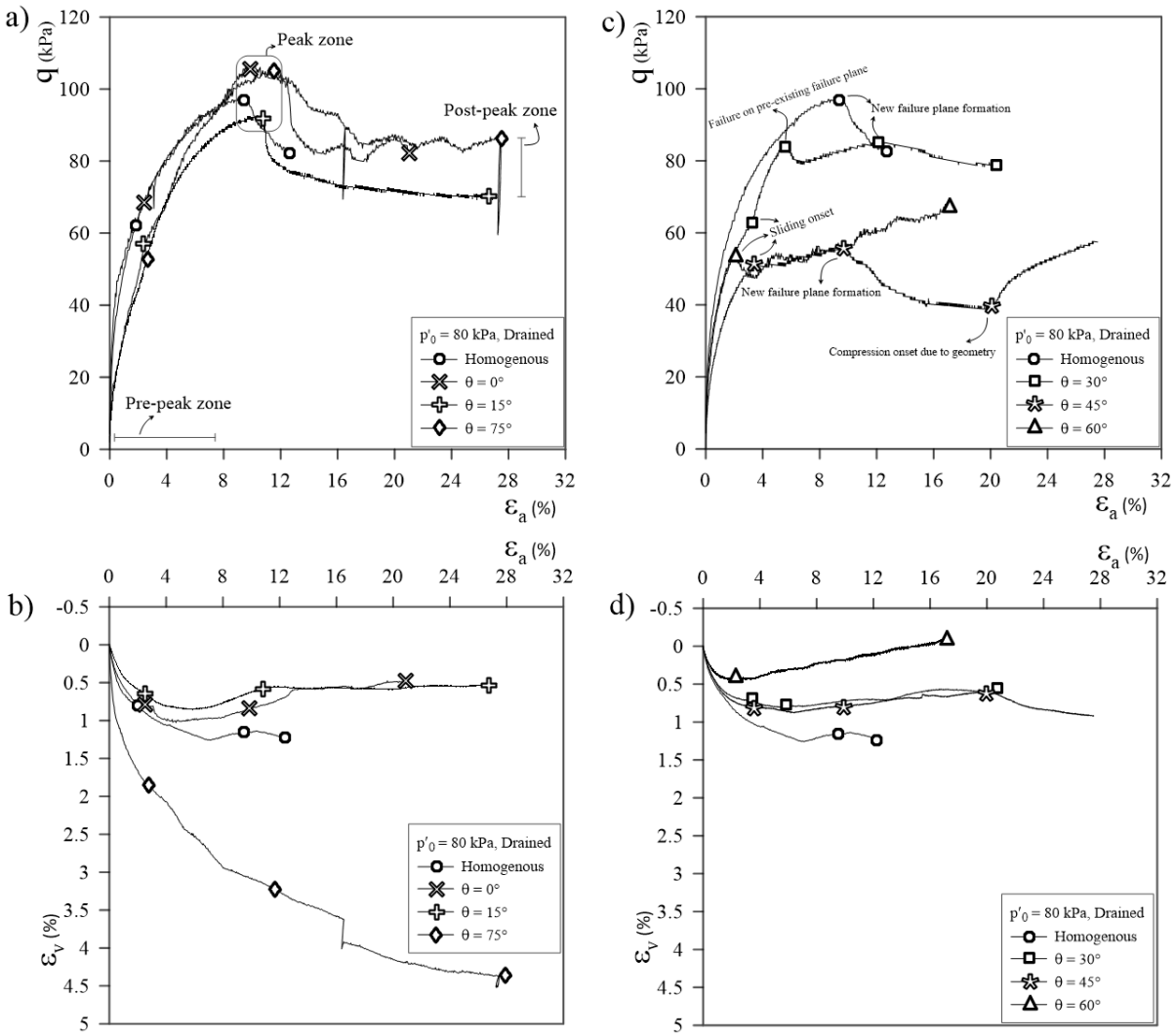

Fig. 24) Shearing behaviour for specimens under p'$_0$ = 80 kPa in drained condition: a,c) Deviatoric stress (q) versus axial strains (ε_a), b,d) volumetric strains (ε_v) versus axial strains (ε_a).

Regarding the specimen with a 75-degree pre-existing failure plane, it should be noted that in standard triaxial tests with a height-to-diameter ratio of 2, the maximum cutting angle without intersecting the top and bottom of the sample is approximately 63.4 degrees. This geometric limitation means a 75-degree pre-existing failure plane cannot experience sliding on its pre-existing failure plane. When examining the volumetric behaviour of this specimen, it exhibits more variation compared to others, which could be due to the geometric constraint or possibly inaccurate data acquisition. Consequently, the data for this specimen, as presented in Fig. 24b, should be interpreted with caution.

To interpret the volumetric strain behaviour observed in other specimens shown in Fig. 24b and Fig. 24d, it is clear that after initial contraction in the pre-peak zone, a slight dilatant behaviour begins just before reaching the peak or after sliding onset. This pattern may be attributed to the low effective confining pressures, which aligns with observations made during the consolidation of these specimens (Fig. 23a).

In the analysis of shearing behaviour of specimens with 30, 45, and 60-degree pre-existing failure planes, consolidated under an 80 kPa effective confining pressure, it was observed that sliding commenced along these planes prior to the formation of new failure planes, as illustrated in Fig. 24c and Fig. 24d. This resulted in shearing behaviour distinct from that of homogeneous specimens. Each specimen demonstrated unique shearing behaviour after the onset of sliding, which will be detailed separately in this section.

For the specimen with a 30-degree pre-existing failure plane, a peak was reached after the onset of sliding, indicating the maximum strength of this plane. Subsequently, at 12% axial strain, a new failure plane formed. The increase in deviatoric stress after sliding onset suggests simultaneous compression and sliding. This combination resulted in shearing behaviour distinct from that observed in the specimens shown in Fig. 24a. Due to the sliding along the pre-existing failure plane, the specimen did not retain its original cylindrical shape, and the stress release after the formation of the new failure plane was limited. Consequently, the deviatoric stress values for the peak and post-peak conditions appeared mostly similar.

It is important to note that in all specimens, once a new failure plane forms, sliding along the pre-existing failure plane stops. Subsequently, sliding occurs exclusively on the newly formed failure plane, without any concurrent compression.

Moving to the specimen with a 45-degree pre-existing failure plane, a similar pattern was observed where sliding onset came before the formation of a new failure plane at about 10%

axial strain, prior to reaching maximum strength on the pre-existing plane. Compared to the 30-degree specimen, this one exhibited a gentler slope after the onset of sliding, suggesting less dominant compression on the pre-existing failure plane.

Notably, after the formation of the new failure plane, stress release in the 45-degree specimen was less constrained than in the 30-degree specimen. As testing progressed, the significant sliding along the new failure plane forced the specimen to exhibit compressive behaviour once more. The complexity of interpreting these results is heightened by considerable geometric changes and a marked departure from the specimen's original cylindrical shape.

In the analysis of the specimen with a 60-degree pre-existing failure plane, sliding onset was observed. However, unlike other specimens, this specimen did not form a new failure plane, continuing to experience a combination of sliding and compression in the post-sliding condition. Its slope pattern after the onset of sliding was similar to that of the 45-degree specimen, yet it notably did not form a new failure plane.

Initially, after the onset of sliding, the 60-degree specimen exhibited a slight stress release, followed by a continuous combination of sliding and compression until the end of the test. This contrasts with the 45-degree specimen, where such stress release was not observed. This difference could be attributed to the increased stress concentration around the pre-existing failure plane, (Pilkey, W. D. et al., 2008). The stress concentration in steeper discontinuities, as in the 60-degree specimen, is typically higher compared to lower inclinations, underscoring the significant impact of a single pre-existing failure plane on the homogeneity and stress response in soft soils.

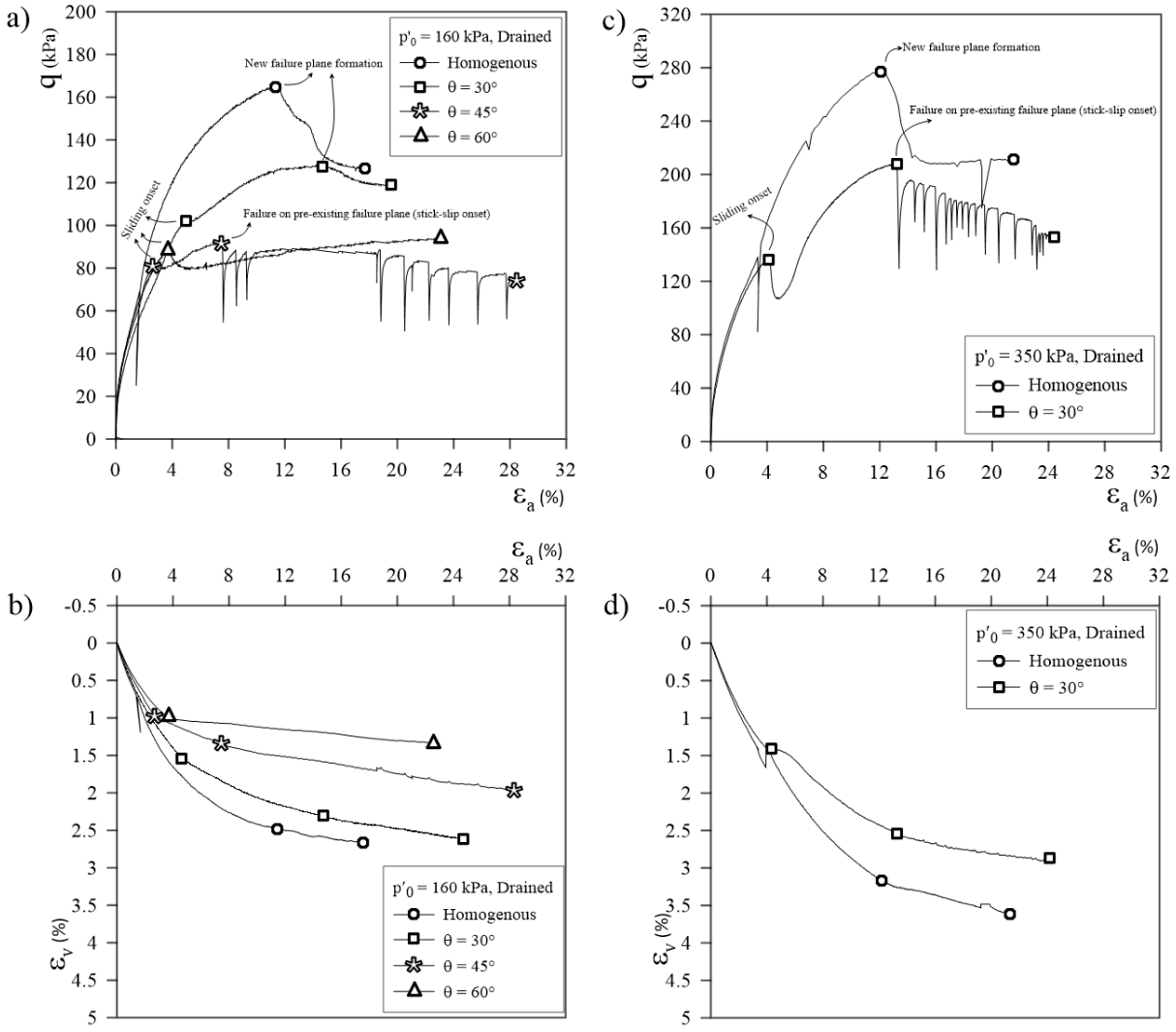

Fig. 25) Shearing behaviour for specimens under p'$_0$ = 160 and 350 kPa in drained condition: a,c) Deviatoric stress (q) versus axial strains (ε_a), b,d) volumetric strains (ε_v) versus axial strains (ε_a).

As discussed in Section 3.3.1, specimens with 30, 45, and 60-degree pre-existing failure planes, along with a homogeneous specimen, underwent consolidated drained triaxial testing under a higher effective confining pressure of 160 kPa. Fig. 25a and Fig. 25b, clearly demonstrates that their shearing behaviour significantly differs from that of the homogeneous specimen.

Upon the onset of sliding along the pre-existing failure planes, the shearing behaviour of the 30-degree specimen closely aligns with its response under an 80 kPa confining pressure, as shown in Fig. 21a. The primary distinction is a more pronounced sliding over compression, indicated by the reduced slope of increasing deviatoric stress in the post-sliding phase and the delayed formation of a new failure plane at 15% axial strain.

The 45-degree specimen, under the increased effective confining pressure, initially mirrors the behaviour of its lower pressure counterpart (Fig. 24a). After the onset of sliding, the peak indicates the maximum strength of this plane, and the emerging stick-slip shearing behaviour

suggests that a new failure plane will not form. This behaviour, characterized by alternating phases of sliding and compression, features significant immediate stress drops, denoting exclusive sliding along the pre-existing failure plane, followed by a compression phase until the specimen regains its previous shear strength. This stick-slip behaviour, which inhibits the formation of a new failure plane, leads to a progressive reduction in shear strength, likely due to clay particles rearrangement. This phenomenon closely simulates seismic responses observed in faults and highlights its potential for causing destructive site vibrations (McGarr and Fletcher, 2004).

In contrast, the 60-degree specimen exhibits no significant change in shearing behaviour under the increased effective confining pressure compared to its lower pressure counterpart (Fig. 24a). Fig. 25b provides additional insights, especially when compared with Fig. 24b. The higher effective confining pressure results in larger volumetric strain changes, reducing data acquisition errors. Post-sliding phase analysis reveals that the steepest slope in Fig. 22b is observed in the 30-degree specimen, with the 60-degree specimen showing a gentle slope. This indicates that in the post-sliding phase, where sliding and compression combine, the compressive component is more pronounced in specimens with lower-angle pre-existing failure planes due to higher volumetric strain changes.

The final series of consolidated drained tests, conducted with an effective confining pressure of 350 kPa, focused on the specimen with a 30-degree pre-existing failure plane, along with a homogeneous specimen for comparison, as detailed in Section 3.3.1.

Observations from Fig. 25c reveals notable differences in the shearing behaviour of the 30-degree pre-existing failure plane specimen compared to its behaviour under lower effective confining pressures (seen in Fig. 24c and Fig. 25a). Across all tests, the onset of sliding occurred at approximately the same axial strain range, 4% to 6%. However, under the increased effective confining pressure of 350 kPa, a significant stress release was noted at the sliding onset. This phenomenon is likely due to the enhanced interlocking of the specimen's upper and lower blocks, along with increased stress concentration near the pre-existing failure planes. Following this initial stress release, there was an observable increase in deviatoric stress, suggesting a combined effect of sliding and compression.

Contrasting with earlier tests where the 30-degree specimens formed new failure planes upon reaching the post-peak zone of the homogeneous specimen (Fig. 24c and Fig. 25a), the latest test at 350 kPa did not lead to new failure plane formation. Instead, a stick-slip behaviour

similar to that seen in the 45-degree specimen tested under 160 kPa (Fig. 25a) was observed. This behaviour, characterized by a cyclic pattern of separated sliding and compression, resulted in a gradual decrease in deviatoric stress. This mirrored the shearing behaviour observed in the 45-degree specimen under 160 kPa effective confining pressure.

Considering the observed shearing behaviours, it can be concluded that specimens with pre-existing failure planes in consolidated drained conditions are unlikely to form new failure planes at 350 kPa effective confining pressure. This suggests that under normally consolidated conditions, the formation of new failure planes in these specimens becomes restricted as confining pressure increases. In contrast, homogeneous specimens continue to form new failure planes under similar conditions.

Specifically, at 80 kPa effective confining pressure, specimens with 30 and 45-degree pre-existing failure planes formed new failure planes. At 160 kPa, only the 30-degree specimen formed a new plane, whereas at 350 kPa, even this specimen failed to form a new failure plane. This trend indicates that while homogeneous specimens consistently form new failure planes under increased confining pressures, the ability to form new failure planes in specimens with pre-existing failure planes is limited.

It is noteworthy that these specimens were compacted using 1-D consolidation by a Consolidometer up to 320 kPa. Consequently, the 350 kPa effective confining pressure lies beyond the onset of the normally consolidated range. The formation of new failure plane in homogeneous specimen at this pressure is consistent with their consolidation history, and is not considered unusual behaviour. However, it is important to highlight that specimens with pre-existing failure planes demonstrate increased sensitivity to the rise in confining pressure. Upon entering the normally consolidated range, it becomes unlikely to observe both subsequent mechanisms (sliding along the pre-existing failure plane and the formation of a new failure plane), in specimens with pre-existing failure planes, regardless of the inclination of these planes.

3.3.5 Undrained Shearing Phase

In the undrained shearing phase, Fig. 26 offers the first interpretation of data during the undrained shearing phase for both homogeneous specimens and those with a 30-degree pre-existing failure plane. This Fig. highlights the variations in deviatoric stresses and excess pore water pressures relative to axial strains throughout the undrained shearing condition. In terms of deviatoric stress, the behaviour corresponds to that observed under drained conditions when

considering the schematic representation. At 80 kPa initial effective mean stress, the onset of sliding leads to failure on the pre-existing failure plane at about 8 percent axial strain, followed by the formation of a new failure plane at 12 percent axial strain. For higher initial effective mean stresses of 160 kPa and 350 kPa, new failure planes appear subsequent to the sliding onset. This differs from the drained condition at 350 kPa, where stick-slip behaviour rather than new plane formation was observed. Regarding excess pore water pressures, for initial mean effective stresses of 80 and 160 kPa, variations due to sliding onset on the 30-degree failure planes are limited earlier compared to homogeneous specimens. Yet, both homogeneous and 30-degree specimens exhibit similar post-peak and post-sliding behaviours. Specifically, at an initial stress of 350 kPa, the behaviour of both specimen is consistent across all phases of the shearing process (Fig. 26).

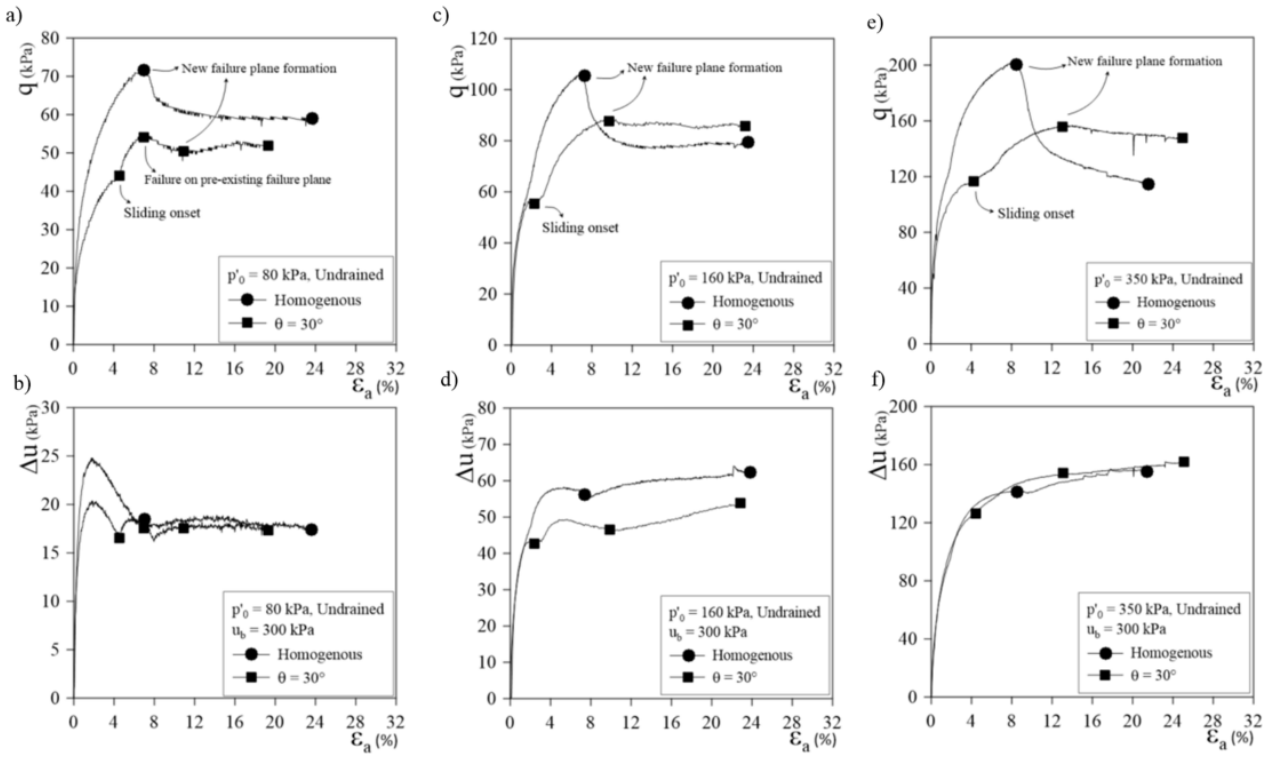

Fig. 26) Shearing behaviour for specimens under p'0 = 80,160 and 350 kPa in undrained condition: a,c,e) Deviatoric stress (q) versus axial strains (εa), b,d,f) excess pore water pressure (Δu) versus axial strains (εa).

Chapter 4

Application of the Sliding Block Method

4.1 Introduction

The primary focus of Chapter 4 is on developing an advanced method for interpreting the post-peak phase of triaxial tests. As explored in Section 3.2.4, conventional interpretations consider the specimen to be a continuous cylindrical medium throughout the test. This perspective, however, leads to inaccuracies in assessing post-peak shear strength, particularly in specimens with newly formed or pre-existing failure planes. Upon the formation of failure plane in homogeneous specimens or the onset of sliding in specimens with pre-existing failure planes, the specimen transforms from a continuous cylindrical medium to two interactive blocks, moving relative to each other along their interface. Understanding this dynamic interaction, which is influenced by the changing contact area due to vertical axial displacement, is essential for accurately determining the specimen's shear strength and behaviour in the post-peak phase.

The transformation of the specimen from a continuous medium to two distinct blocks, upon the failure plane's formation in homogeneous specimens or the onset of sliding in specimens with pre-existing failure planes, results in two noteworthy changes: firstly, a reduction in the contact area between the blocks, and secondly, potential variations in force equilibrium. The chapter explores these two aspects:

Force Balance Correction on the newly formed and pre-existing failure planes: This task focused on calculating the normal (N) and tangential (T) forces on these planes, identifying any change in equilibrium and the emergence of new forces.

Contact Area Correction on the newly formed and pre-existing failure planes: This task involved developing a method to precisely calculate the changing contact area between the two specimen blocks as a function of axial displacement (Δz). This is crucial to comprehend the evolving interaction between the blocks during the test.

These revisions are essential to understand the real shear stresses and the specimen's response during the post-peak or post-sliding phase. The implications of this precise interpretation method are profound, offering deeper insights into the mechanical behaviour of specimens. It also indicates that conventional methods of determining shear strength parameters might be overly cautious, thus contributing to a more comprehensive understanding of soil mechanics in geotechnical engineering.

4.2 Force Balance Revision

Regarding to Jaeger (2007), Equations 3.8 and 3.9, Section 3.2.4.2, in the shearing phase, normal and tangential stresses on an arbitrary plane (σ_θ, τ_θ) can show as Equations 4.1 and 4.2 (Fig. 27):

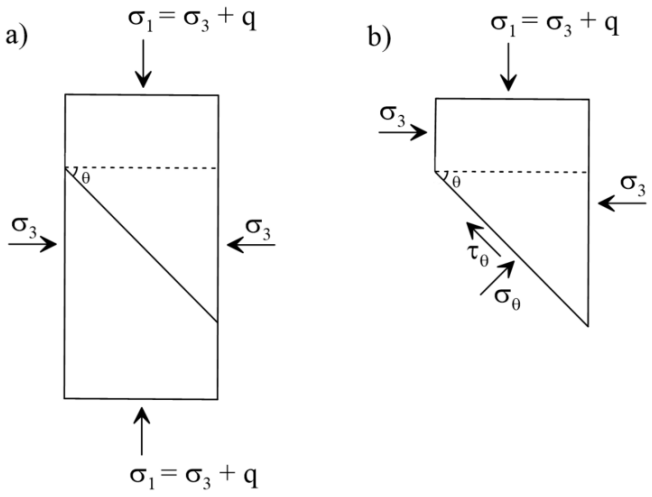

Fig. 27) a) stresses acting on the surfaces of the specimen during shearing condition, b) stresses acting on the top block surfaces of the specimen during shearing condition.

$$\sigma_\theta = (\sigma_3) + \left[\frac{1}{2}(q)(1 + cos2\theta)\right] \tag{4.1}$$

$$\tau_\theta = \frac{1}{2}(q)sin2\theta \tag{4.2}$$

From Equations 4.1 and 4.2, it can be concluded that confining pressure and deviatoric stress are two independent variables (for more detailed information, see Appendix A). To compute the normal and tangential stresses on the plane of failure, if:

$$\sigma_\theta = (\sigma_\theta)_c + (\sigma_\theta)_q \tag{4.3}$$

$$\tau_\theta = (\tau_\theta)_c + (\tau_\theta)_q \tag{4.4}$$

where $(\sigma_\theta)_c = \sigma_3$, $(\sigma_\theta)_q = \left[\frac{1}{2}(q)(1 + cos2\theta)\right]$, $(\tau_\theta)_c = 0$, and $(\tau_\theta)_q = \frac{1}{2}(q)sin2\theta$.

To consider the effect of variation of failure plane's contact area or pre-existing failure plane's contact area (A_θ), in all phases of shearing condition, the Equations 4.1 and 4.2 is replaced by the normal (N_θ) and tangential forces (T_θ) acting on an arbitrary plane, inclined at an angle θ from the horizontal axis (Equation 4.5 and Equation 4.6):

$$N_\theta = N_c + N_q \tag{4.5}$$

$$T_\theta = T_q \tag{4.6}$$

where N_c and N_q, are the normal forces acting on an arbitrary plane due to confining pressure and deviatoric stress, respectively. Also, T_q is the tangential force acting on an arbitrary plane due to the deviatoric stress.

The force equilibrium can be analyzed across three distinct phases of the shearing stage to encompass all potential conditions, considering that the confining pressure (σ_3) remains constant throughout this stage. These phases focus specifically on variations in deviatoric stress (q): the initial phase ($q = 0$), the pre-peak or pre-sliding phase ($q > 0$), and the post-peak or post-sliding phase ($q > 0$):

- **Initial phase ($q = 0$):**

$$N_\theta = N_c = \sigma_3 A_\theta \tag{4.7}$$

$$T_\theta = 0 \tag{4.8}$$

Equations 4.7 and 4.8 represent the normal (N_θ) and tangential (T_θ) forces acting on an arbitrary plane, inclined at an angle θ from the horizontal axis, at the initial phase ($q = 0$) of the shearing stage (for more detailed information, see Appendix A).

- **pre-peak or pre-sliding phase ($q > 0$):**

$$N_\theta = N_c + N_q = \sigma_3 A_\theta + F_q cos\theta \tag{4.9}$$

$$T_\theta = T_q = F_q sin\theta \tag{4.10}$$

Equations 4.9 and 4.10 represent the normal (N_θ) and tangential (T_θ) forces acting on an arbitrary plane, inclined at an angle θ from the horizontal axis, during the pre-peak or pre-sliding phase ($q > 0$) of the shearing stage (for more detailed information, see Appendix A).

- **post-peak or post-sliding phase ($q > 0$):**

In this scenario, as the first approach, the analysis follows the same methodology as outlined in Equations 4.9 and 4.10. However, it is crucial to account for the variations in the contact area (A_θ) resulting from the sliding of the top block over the bottom block during the post-peak or post-sliding phase. Consequently, changes in the contact area influence the normal force, potentially increasing its value as described in Equation 4.9. Conversely, these changes do not affect the tangential force, as indicated in Equation 4.10 (for more detailed information, see Appendix A).

In the second approach for this phase, Fig. 28 illustrates the forces acting on the surfaces of the top block. Here, F_q represents the axial load recorded by the submerged load cell in the triaxial

apparatus. F_{TS} is the force resulting from the confining pressure on the top surface of the top block, while F_{L1} and F_{L2} are the lateral forces due to the confining pressure acting on the upper and lower parts of the top block, respectively. S denotes the force resulting from the confining pressure on the new or pre-existing failure plane, which is not in the contact with the bottom block.

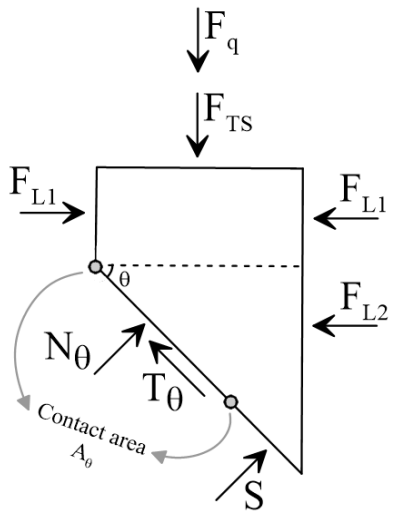

Fig. 28) Forces acting on the top block in the post-peak or post-sliding phase (q>0).

$$N_\theta = -S + \left[\left(F_q + F_{TS}\right)cos\theta\right] + \left[\left(F_{L2}\right)sin\theta\right] \quad (4.11)$$

$$T_\theta = \left[\left(F_q + F_{TS}\right)sin\theta\right] - \left[\left(F_{L2}\right)cos\theta\right] \quad (4.12)$$

where, N_θ, and T_θ represent the normal and tangential forces acting on either a new or a pre-existing failure plane, as detailed in Equations 4.11 and 4.12, respectively. It is also essential to describe the forces F_{TS}, F_{L2} and S, which are explained in Equations 4.13, 4.14 and 4.15:

$$S = \sigma_3(A_{\theta i} - A_\theta) \quad (4.13)$$

$$F_{TS} = \sigma_3 \pi r^2 \quad (4.14)$$

$$F_{L2} = \sigma_3(A_{\theta i} sin\theta) = \sigma_3 \pi r^2 tan\theta \quad (4.15)$$

where $A_{\theta i}$ represents the initial contact area at the sliding onset. Integrating Equations 4.13, 4.14. and 4.15 into Equations 4.11 and 4.12 demonstrates that both approaches yield identical results. Consequently, N_θ and T_θ correspond to the values derived in Equations 4.9 and 4.10 (for more detailed information, see Appendix A).

The simplified force equilibrium is depicted in Fig. 29:

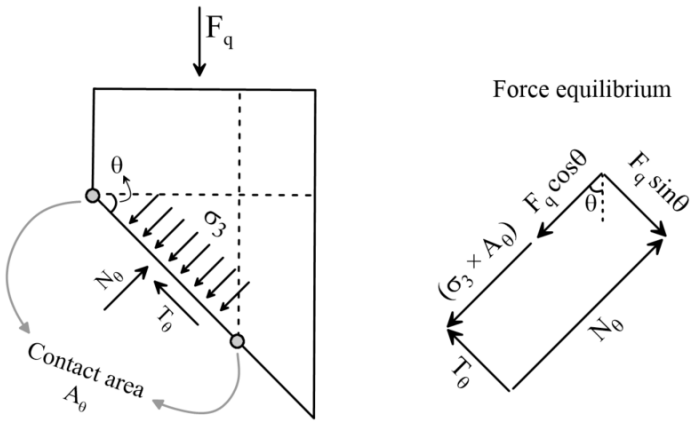

Fig. 29) The simplified force equilibrium.

4.2.1 Pore Water Pressure Effect

Pore water pressure (u), which consists of back pressure (u_b) and excess pore water pressure (Δu), impacts force (N_θ', T_θ) equilibriums as shown on Fig. 30 (N_θ' is the normal force acting on the failure plane by considering the effect of pore water pressure):

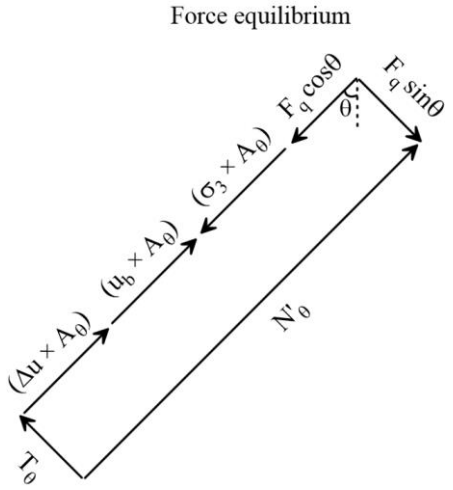

Fig. 30) The simplified force equilibrium by considering the effect of pore water pressure.

Given that the confining pressure and back pressure remain constant during the shearing phase, the effective confining pressure (σ_3') is defined as the difference between the confining pressure and back pressure ($\sigma_3' - u_b$). Thus, Fig. 31 serves as an alternative representation of Fig. 30:

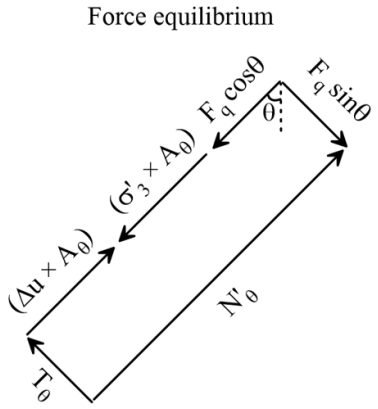

Fig. 31) Alternative representation of Fig. 30.

$$N_\theta{}' = F_q cos\theta + [(\sigma_3{}' - \Delta u)A_\theta] \tag{4.16}$$

$$T_\theta = F_q sin\theta \tag{4.17}$$

Examination of Equations 4.16 and 4.17 reveals that pore water pressure has no effect on the tangential force acting on a new or pre-existing failure plane. .

4.2.1.1 Total (τ_θ, σ_θ) stress path on the pre-existing failure plane in both pre-sliding and post-sliding phase

The total stress path inclination is equal to:

$$\left[\frac{\tau_\theta}{(\sigma_\theta - \sigma_3)}\right] = tan\theta \tag{4.18}$$

Equation 4.18 indicates that in both drained and undrained conditions, the plane inclination solely determines the inclination of the total stress path, with no variation between the sliding block model and conventional methods. However, the sliding block model, as detailed in Section 4.3, accounts for the actual contact area, which gradually decreases compared to conventional methods during the post-sliding phase. Consequently, the total stress states reached in the sliding block model are at higher levels, though the inclination of the total stress path remains consistent.

4.2.1.2 Effective (τ_θ, σ_θ') stress path on the pre-existing failure plane in both pre-sliding and post-sliding phase

The effective stress path inclination is equal to:

$$\left[\frac{\tau_\theta}{(\sigma_\theta{}' - \sigma_3{}')}\right] = \left[\frac{(F_q sin\theta)}{(F_q cos\theta - \Delta u A_\theta)}\right] \tag{4.19}$$

Examining Equation 4.19 reveals that in undrained conditions, where excess pore water pressure is not zero ($\Delta u \neq 0$), four factors influence the inclination of the effective stress path. These include axial force (F_q), plane inclination (θ), excess pore water pressure (Δu), and contact area (A_θ). The sliding block model differentiates itself from conventional methods by accounting for the actual contact area, which gradually decreases starting from the onset of sliding, as detailed in Section 4.3. Due to this approach, the impact of excess pore water pressure on the effective stress path inclination is more significant in the sliding block model than in conventional methods, resulting in steeper inclinations and higher stress states.

In drained conditions, where ($\Delta u = 0$), the inclination of the effective stress path inclination shows that in drained conditions, the inclination of the effective stress path is determined entirely by the plane inclination, and it matches the total stress path inclination (Equation 4.18). There is no difference in the effective stress path inclination between the sliding block model and conventional methods. However, as detailed in Section 4.3, the sliding block model considers the actual contact area, which gradually decreases in comparison to conventional methods during the post-sliding phase. As a result, the effective stress states achieved in the sliding block model are higher, although the inclination of the effective stress path remains the same.

4.2.2 New Failure Plane Formation in the Post-Sliding Phase

- Initial phase:

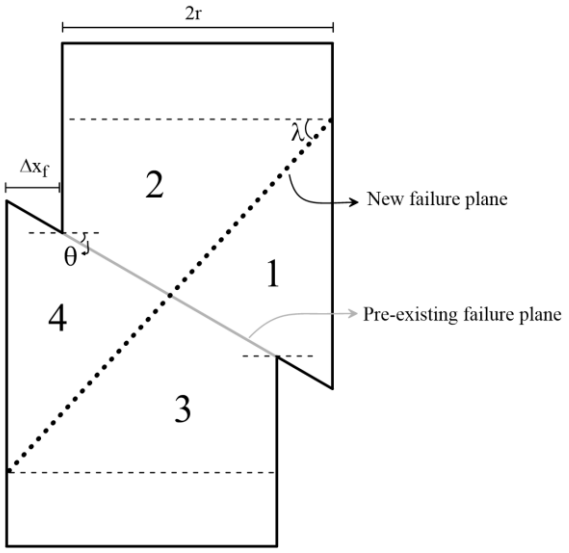

Fig. 32) Schematic view of new failure plane formation in the post-sliding phase.

Assumption:

The new failure plane forms symmetrically, dividing A_θ into two equal halves. Consequently, the area of 1 equals the area of 4, and the area of 2 equals the area of 3 (Fig. 32).

Force equilibrium (Fig. 33):

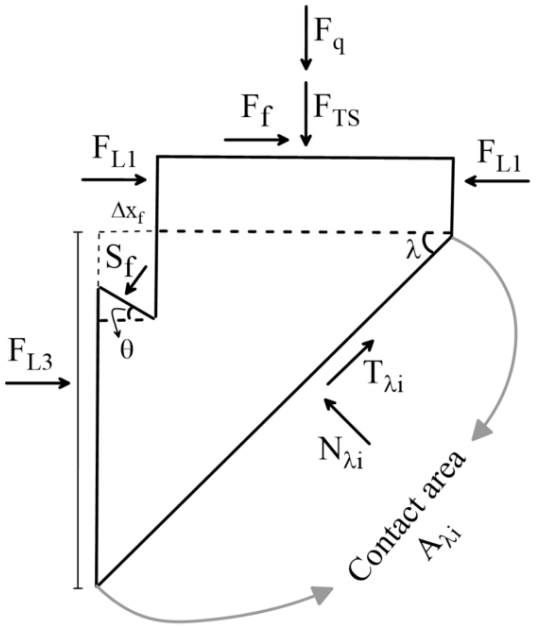

Fig. 33) Forces acting on the top block in the initial phase of new failure plane formation in the post-sliding phase.

$$N_{\lambda i} = \left[\left(F_q + F_{TS} + S_f cos\theta\right)cos\lambda\right] + \left[\left(F_{L3} + F_f\right)sin\lambda\right] - \left(S_f sin\theta sin\lambda\right) \quad (4.20)$$

$$T_{\lambda i} = \left[\left(F_q + F_{TS} + S_f cos\theta\right)sin\lambda\right] - \left[\left(F_{L3} + F_f\right)cos\lambda\right] + \left(S_f sin\theta cos\lambda\right) \quad (4.21)$$

where, $N_{\lambda i}$ and $T_{\lambda i}$ represent the initial normal and tangential forces acting on the new failure plane in post-sliding phase, as detailed in Equations 4.20 and 4.21, respectively. F_f is the friction force resulting from the friction between specimen's top surface and the porous stone, S_f denotes the final force resulting from the confining pressure on the pre-existing failure plane, which is not in the contact with the bottom block and F_{L3} is the lateral force due to the confining pressure acting on a part of the top block. It is also essential to describe these forces which are explained in Equations 4.22, 4.23 and 4.24:

$$S_f = \sigma_3\left(A_{\theta i} - A_{\theta f}\right) \quad (4.22)$$

$$F_f = F_q \mu_{mp} \quad (4.23)$$

$$F_{L3} = \sigma_3 A_{\lambda i} sin\lambda \quad (4.24)$$

where, $A_{\theta f}$ is A_θ, at final position in the post-sliding phase. μ_{mp} is the assumed maximum friction between top surface of Speswhite Kaolin specimens and the porous stone, and it is set 0.245 for this study. This value is justified as it falls between the residual internal friction of

approximately 0.15 and the peak internal friction of about 0.27 for Speswhite Kaolin. This parameter is considered when Δx_f > 3 mm, otherwise considered as zero (Δx_f is Δx at final position in the post-sliding phase).

- Final phase:

  Force equilibrium (Fig. 34):

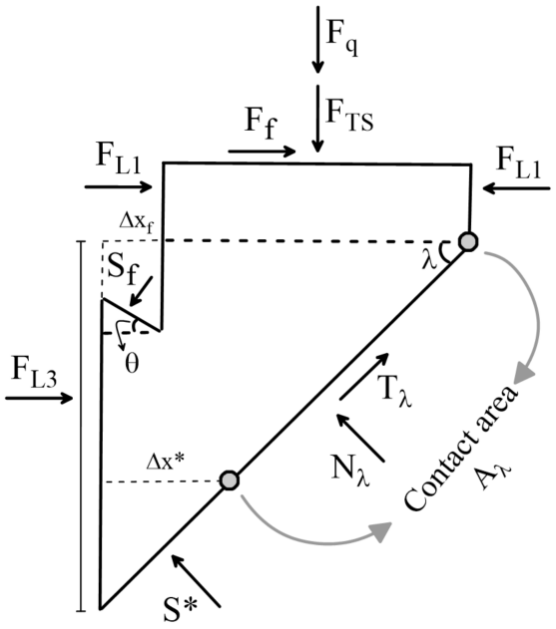

Fig. 34) Forces acting on the top block after the initial phase of the new failure plane formation in the post-sliding phase.

$$N_\lambda = -(S^*) + \left[\left(F_q + F_{TS} + S_f cos\theta\right)cos\lambda\right] + \left[\left(F_{L3} + F_f\right)sin\lambda\right] - \left(S_f sin\theta sin\lambda\right) \quad (4.25)$$

$$T_\lambda = \left[\left(F_q + F_{TS} + S_f cos\theta\right)sin\lambda\right] - \left[\left(F_{L3} + F_f\right)cos\lambda\right] + \left(S_f sin\theta cos\lambda\right) \quad (4.26)$$

where, N_λ and T_λ represent the normal and tangential forces acting on the new failure plane in post-sliding phase, as detailed in Equations 4.25 and 4.26, respectively. S^* denotes the force resulting from the confining pressure on the new failure plane in post-sliding phase, which is not in the contact with the bottom block, where $A_{\lambda i}$ is A_λ at initial phase of new failure plane formation (Equation 4.27). Calculation of the other forces are the same as the initial phase (for more detailed information, see Appendix A).

$$S^* = \sigma_3 \times (A_{\lambda i} - A_\lambda) \quad (4.27)$$

4.3 Area Correction

In this section, calculations are focused on determining the contact area for two distinct phases of the shearing condition: the pre-peak or pre-sliding phase, and the post-peak or post-sliding

phase. It is important to note that in the initial phase (when $q = 0$), calculating the contact area is not necessary since the normal and tangential stresses on the failure plane do not depend on the contact area. During the saturation and consolidation phases, radial strains are measured by observing the volume variations. Prior to the application of deviatoric stress, variations in the contact area are not critical in the stress calculations on each plane, as the normal stress is consistently equal to σ_3, and shear stress remains zero. Nonetheless, documenting the area's changes during these phases is essential. The initial area of the specimen at the onset of the failure stage serves as a baseline for observing subsequent variations. Accurately determining the deviatoric stress during the failure stage depends on this baseline measurement. The area calculation becomes essential in the pre-peak or pre-sliding phase, and post-peak or post-sliding phase, as outlined below.

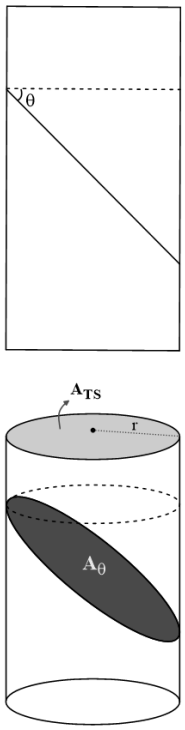

Fig. 35) 2-D and 3-D view of the pre-existing failure plane in the initial phase of the shearing stage (pre-sliding phase).

In the pre-sliding phase as depicted in Fig. 35, the contact area, denoted as A_θ, is calculated through its projection on the specimen's top surface area ($A_{TS} = \pi r^2$). Specifically, A_θ can be expressed as $A_{TS} / cos\theta$, where the radius of the specimen is the critical variable influencing this area. The radius is subject to change due to variations in axial (ε_a), and volumetric (ε_v) strains, with ε_v defined as $\varepsilon_a + 2\varepsilon_r$, and the radius r calculated using $r = r_i + r_i\varepsilon_r$. Here, r_i represents the initial radius, and ε_r, is the radial strain. The volumetric and axial variations are

accurately measured by Volume Gauges and Linear Variable Differential Transformers (LVDTs), respectively, ensuring precise data acquisition during the test.

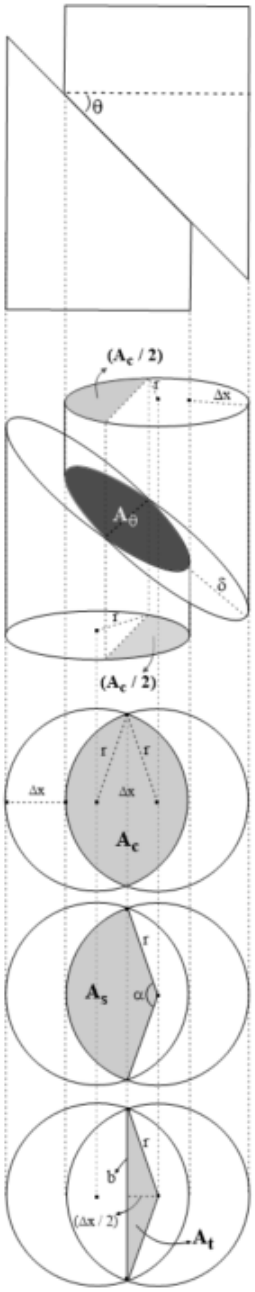

$A_\theta = A_c / \cos\theta$

$A_c = 2(A_s - A_t)$

$A_s = (\alpha/360°)r^2$

$\alpha = 2\arcsin(b / 2r)$

$A_t = (b / 2)(\Delta x / 2)$

$(b / 2)^2 = (r)^2 - (\Delta x / 2)^2$

$(b / 2) = \sqrt{(r)^2 - (\Delta x / 2)^2} = \sqrt{[r + (\Delta x / 2)][r - (\Delta x /2)]}$

Fig. 36) 2-D and 3-D view of pre-existing failure plane in the post-sliding or post-peak phase of shearing stage and the calculation of it.

In the post-sliding and post-peak phase as shown in Fig. 36, the contact area, denoted as A_θ, is determined through its projection onto the specimen's top and bottom surface areas. The combined contact area, A_c, is split equally between the top and bottom surfaces, where $\left(\frac{A_c}{2}\right)^{top} = \left(\frac{A_c}{2}\right)^{bottom}$. Therefore, A_θ is calculated as $A_c / cos\theta$.

To compute $\left(\frac{A_c}{2}\right)$, the illustration in Fig. 34 introduces two distinct areas: A_s and A_t. The calculation for $\left(\frac{A_c}{2}\right)$ involves finding the difference between these areas ($A_s - A_t$). The Fig. 36 clearly shows the method for calculating these areas. For A_s, the radius r and the angle α, are determining factors and for A_t, the triangle's base b, and the horizontal displacement of the upper block Δx, are the key variables. The angle α is determined by the triangle's base b, and the radius r, while b is determined by Δx and r. Therefore, the calculation of A_θ primarily relies on monitoring Δx and r.

4.3.1 Mixture of Compression and Sliding in Post-Sliding Phase

In the post-sliding and post-peak phases, the calculation of Δx and r vary. During the post-sliding phase, the sliding behaviour is a mixture of compression and sliding, as indicated by the increasing axial load. However, in the post-peak phase, sliding occurs without compression. This is characterized by an initial decrease in axial load following the formation of a new failure plane, after which the axial load stabilizes and remains constant.

In saturated triaxial tests, volumetric strains are equivalent to the sum of axial strains and twice the radial strains ($\varepsilon_v = \varepsilon_a + 2\varepsilon_r$). Conventional data interpretation does not distinguish between the pre-sliding/pre-peak and post-sliding/post-peak phases when applying this formula. However, the sliding block method differentiates these phases by relying on axial strains resulting from compression (ε_{ac}) instead of axial strains recorded by LVDT (ε_a) when applying this formula. In other words, in the sliding block method, this relationship is modified to ($\varepsilon_v = \varepsilon_{ac} + 2\varepsilon_r$).

Assuming that axial strains recorded by LVDTs (ε_a) represent the total axial deformation, which is the sum of strains from the effect of compression (ε_{ac}) and sliding (ε_{as}) on the observed reduction of height, different phases exhibit distinct characteristics. During pre-peak or pre-sliding phases, axial strains recorded by LVDTs correspond solely to strains from compression ($\varepsilon_a = \varepsilon_{ac}$), as there is no sliding. In the post-peak phase, recorded axial strains are attributed to sliding alone ($\varepsilon_a = \varepsilon_{as}$), as compressive strains cease. However, in the post-sliding phase, axial strains recorded by LVDTs reflect a combination of strains from both compression and sliding ($\varepsilon_a = \varepsilon_{ac} + \varepsilon_{as}$).

Returning to the calculations of radius (r) and horizontal displacement (Δx), the radius for all phases is determined using ($\varepsilon_v = \varepsilon_{ac} + 2\varepsilon_r$), where r is dependent on the axial compression

strain (ε_{ac}). As for Δx, it is calculated as the product of vertical displacement (Δz) and the cotangent of the angle of pre-existing failure plane or new failure plane ($\Delta x = \Delta z cot\theta$), as illustrated in Fig. 37. Essentially, the calculation of Δx hinges on the axial sliding strain (ε_{as}).

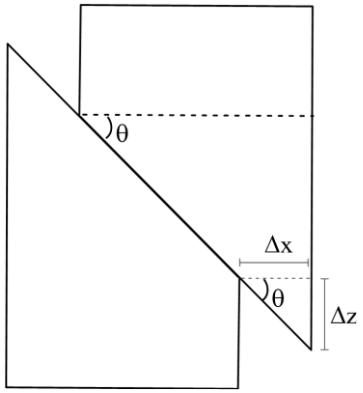

Fig. 37) Schematic view of horizontal (Δx) and vertical displacement (Δz) of top block in the post-peak or post-sliding phase.

The calculation of radius (r) and displacement (Δx), especially in the post-sliding phase where a mix of compression and sliding occurs, demands careful consideration. Identifying the coefficients of compression and sliding is key in this phase. For drained tests, the observed volumetric changes (ε_v), axial load (F_q), can guide the determination of these coefficients. Additionally, for undrained tests, excess pore water pressure (Δu) alongside the axial load (F_q) serves this purpose. A comparative analysis of these observed factors in the post-sliding phase of specimens with pre-existing failure planes against the pre-peak phase of their homogeneous counterparts cannot clarify the proportion of axial strains (measured by LVDTs) attributable to compression and to sliding. Due to the observed similarity in Young's Modulus of these specimens during the initial phase of the failure stage, the approximate predictions derived from comparing the pre-peak phase of homogeneous specimens with the post-sliding phase of specimens with pre-existing failure planes are likely to be accurate but the best way to find more accurate data about the portion of compression and sliding can be achieved from the real pictures of specimens after tests have finished.

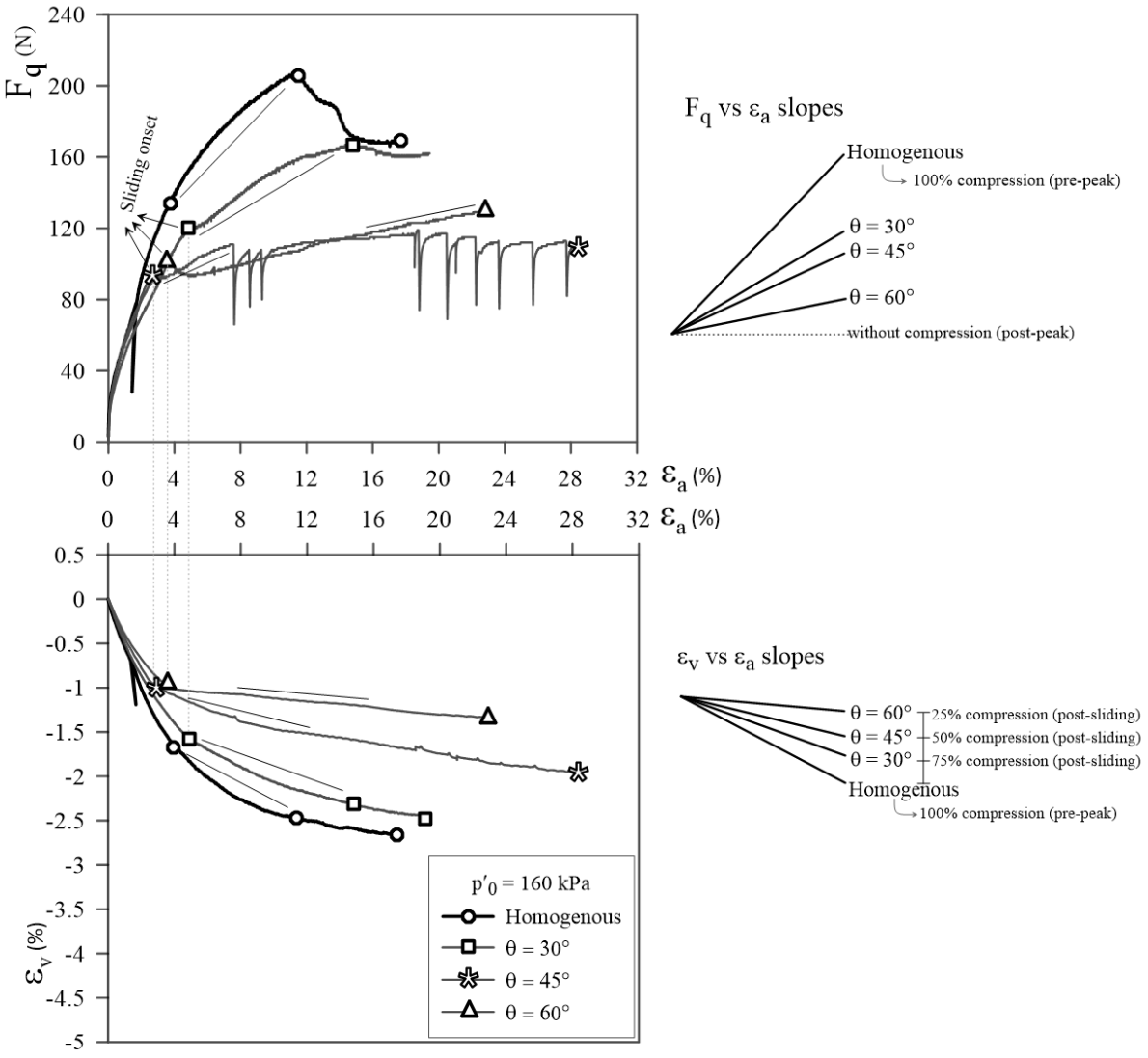

Fig. 38) Interpretation of compression and sliding portions in the post-sliding phase based on the a) axial force (F_q) versus axial strains (ε_a), b) volumetric strains (ε_v) versus axial strains (ε_a).

In drained conditions, for example with p'_0 = 160 kPa, as depicted in Fig. 38, data interpretation is graphically based and therefore not highly precise. However, a noticeable trend can be observed from the slopes of F_q versus ε_a, indicating that all specimens undergo compression in the post-sliding phase (Fig. 38a). The variations in the contact area between the upper and lower blocks differs for each orientation of pre-existing failure planes, mean that relying solely on axial load during post-sliding may not provide a complete picture. Furthermore (Fig. 38b), the slopes of ε_v versus ε_a reveal equal volumetric changes for every 15-degree increase in the pre-existing failure plane inclination during post-sliding. For a rough estimate, in post-sliding, specimens with a 60-degree pre-existing failure plane are assumed to experience approximately 25% compression, those with 45 degrees around 50%, and 30 degrees about 75%. While these estimations are not exact, they closely approximate the actual behaviour.

One hypothesis regarding specimens experiencing sliding along pre-existing failure planes is that the linearity of their behaviour in both the axial force versus axial strain and volumetric strain versus axial strain graphs during the post-sliding phase can indicate the probability of new failure plane formation. Specifically, if these graphs display linear trends in the post-sliding phase, it suggests that new failure plane formation is unlikely (45- and 60-degree pre-existing failure plane with 160 kPa effective confining pressure in drained condition). Conversely, if the graphs exhibit curved patterns during this phase, it implies the progression of plastic strains and the potential for new failure plane development (30-degree pre-existing failure plane with 160 kPa effective confining pressure in drained condition).

To enhance precision in estimating the portions of compression and sliding, individual examination of each data set is recommended. Insight into the proportion of compression and sliding during post-sliding is gained by comparing the secant slopes of axial force versus axial strain in the post-sliding phase to those in the pre-sliding phase. The Table 6 illustrates these proportions for the post-sliding phase. Notably, the absence of a positive slope in the axial force versus axial strain graph indicates the absence of compression, suggesting that sliding is the only occurring mechanism. This assumption leads to the conclusion that the post-sliding phase involves a combination of compression and sliding in all cases, while the post-peak phase is characterized exclusively by sliding behaviour.

The data presented in Table 6 illustrate a trend for specimens with 30-degree pre-existing failure plane: as effective confining pressures increase, there is a decrease in the compression component and an increase in the sliding component in specimens. To develop a mathematical model that integrates the impact of effective confining pressures, Young's Modulus, and post-sliding phase behaviour, further study is required. This includes examining specimens under varied confining pressures or with pre-existing failure planes, using diverse materials or Speswhite Kaolin with different densities.

Table 6) Compression and sliding portion by comparing axial forces (F_q).

Specimen	Effective confining pressure (kPa)	Pre-existing failure plane θ (°)	Post-sliding (on the pre-existing failure plane)							Post-peak (on the new failure plane)							
			Recorded ε_a ($\varepsilon_a = \varepsilon_{ac} + \varepsilon_{as}$)			Compression (%)	Sliding (%)	ε_{ac}[1] (%)	ε_{as}[2] (%)	Recorded ε_a ($\varepsilon_a = \varepsilon_{ac} + \varepsilon_{as}$)			Compression (%)	Sliding (%)	ε_{ac} (%)	ε_{as} (%)	
			Onset (%)	End (%)	End – Onset (%)					Onset (%)	End (%)	End – Onset (%)					
ESM 51	80	Homogenous	-	-	-	-	-	-	-	9.0	12.4	3.4	0	100	0	3.4	CD
ESM 62		0	-	-	-	-	-	-	-	9.7	20.9	11.2	0	100	0	11.2	
ESM 442		15	-	-	-	-	-	-	-	10.4	27	16.6	0	100	0	16.6	
ESM 61		30	3.2	12.2	9	59	41	5.3	3.7	12.2	20.9	8.7	0	100	0	15.4	
ESM 112		45	3.4	9.2	5.8	10	90	0.6	5.2	9.2	19.9	10.7	0	100	0	10.7	
ESM 71		60	2	16.5	14.5	6	94	0.9	13.6	-	-	-	-	-	-	-	
ESM 102		75	-	-	-	-	-	-	-	11.4	27.9	16.5	0	100	0	16.5	
ESM 142	160	Homogenous	-	-	-	-	-	-	-	11.2	17.7	6.5	0	100	0	6.5	
ESM 161		30	5.1	14.3	9.2	21	79	1.91	7.29	14.3	19.5	5.2	0	100	0	5.2	
ESM 162*		45	2.7	7.4	4.7	10	90	0.5	4.2	7.4	28.4	21	0	100	0	21	
ESM 152		60	3.7	23	19.3	5	95	1	18.3	-	-	-	-	-	-	-	
ESM 191	350	Homogenous	-	-	-	-	-	-	-	12	21.4	9.4	0	100	0	9.4	
ESM 182*		30	4	12.9	8.9	30	70	2.7	6.2	12.9	24.3		0	100	0	11.4	
ESM 221	80	Homogenous	-	-	-	-	-	-	-	7	23.8	16.8	0	100	0	16.8	CU
ESM 231		30	4.6	7	2.4	47	53	1.1	1.3	7	19.4	12.4	0	100	0	12.4	
ESM 203	160	Homogenous	-	-	-	-	-	-	-	6.7	23.5	16.8	0	100	0	16.8	
ESM 202		30	2.6	10	7.4	26	74	1.9	5.5	10	23.2	13.2	0	100	0	13.2	
ESM 212	350	Homogenous	-	-	-	-	-	-	-	8.3	21.6	13.3	0	100	0	13.3	
ESM 213		30	5.4	13.5	8.1	25	75	2	6.1	13.5	24.9	11.4	0	100	0	11.4	

1: Effect on the radius variation ($\varepsilon_v = \varepsilon_{ac} + 2\varepsilon_r$).

2: Effect on the variation of Δx ($\Delta x = \Delta z \times \cot\theta = \varepsilon_{as} \times h \times \cot\theta$).

*: After the post-sliding phase, no new failure plane forms; instead, stick-slip behaviour, indicative of failure of pre-existing plane with no subsequent new failure plane formation, was observed.

In this study, to enhance the accuracy of data interpretation, the real images of the specimens in their final phase were utilized (Fig. 39, Fig. 40, and Fig. 41).

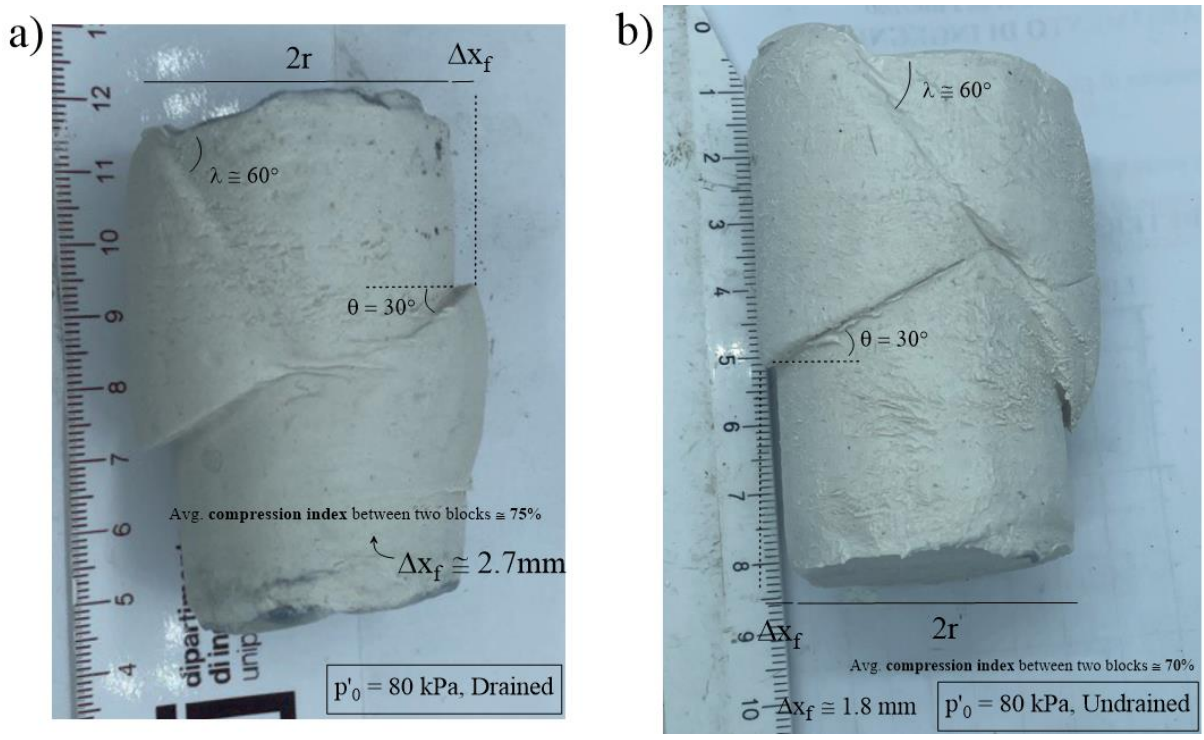

Fig. 39) Final phase of the specimens with 30-deg pre-existing failure plane and $p'_0 = 80$ kPa: a)CD, b)CU.

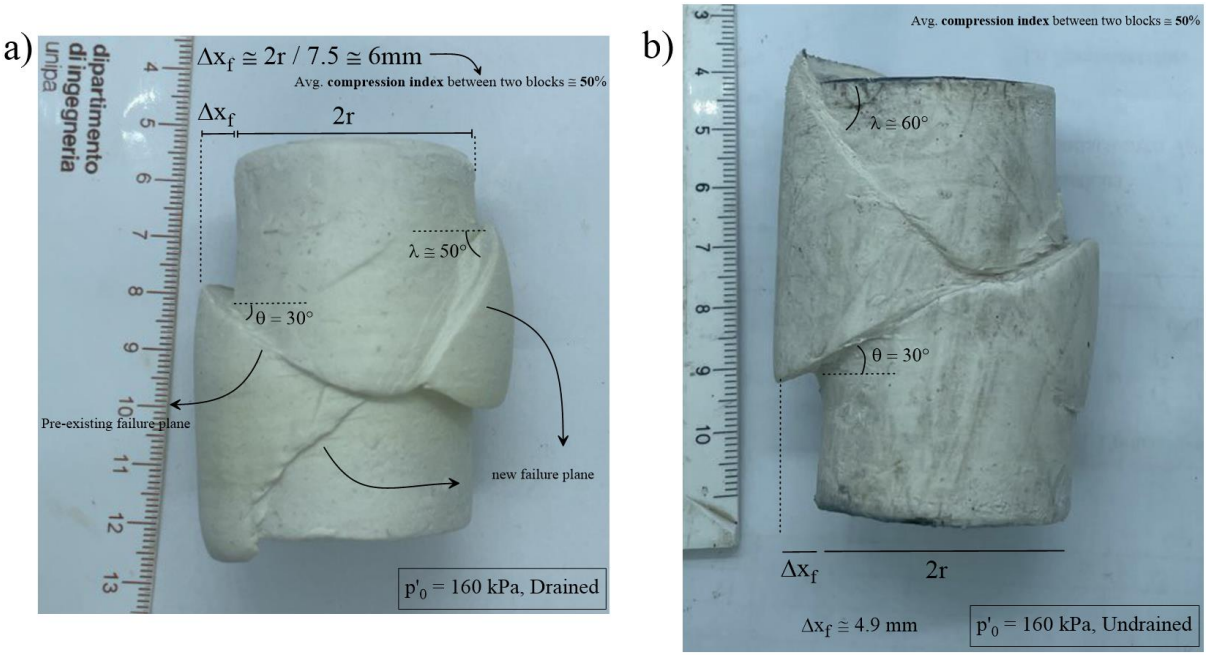

Fig. 40) Fnal phase of the specimens with 30-deg pre-existing failure plane and $p'_0 = 160$ kPa: a) CD, b) CU.

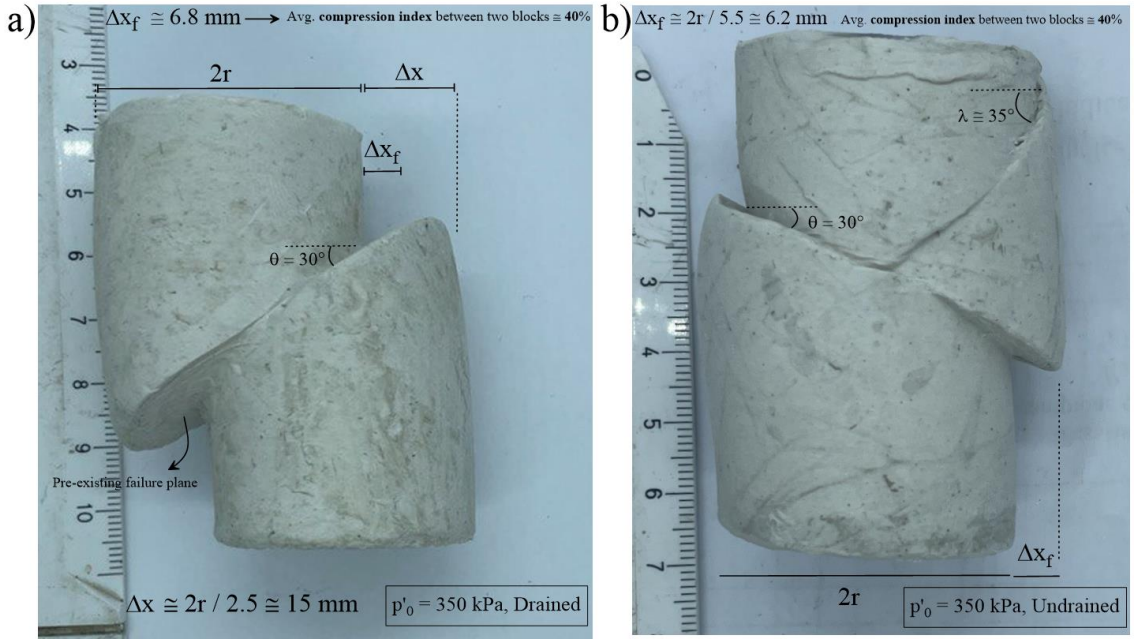

Fig. 41) Final phase of the specimens with 30-deg pre-existing failure plane and p'$_0$ = 350 kPa: a)CD, b)CU.

Table 7) Compression and sliding portions by using the final image of specimens (used for sliding block method interpretation in this study).

Specimen	Effective confining pressure (kPa)	Pre-existing failure plane θ (°)	Post-sliding (on the pre-existing failure plane)			
			Δx_f (mm)	Compression (%)	Sliding (%)	
ESM 51	80	Homogenous	-	-	-	CD
ESM 62		0	-	-	-	
ESM 442		15	-	-	-	
ESM 61		30	2.9	75	25	
ESM 112		45	3.8	40	60	
ESM 71		60	5.9	25	75	
ESM 102		75	-	-	-	
ESM 142	160	Homogenous	-	-	-	
ESM 161		30	6.1	50	50	
ESM 162		45	3.2	30	70	
ESM 152		60	7.9	20	80	
ESM 191	350	Homogenous	-	-	-	
ESM 182		30	6.9	40	60	
ESM 221	80	Homogenous	-	-	-	CU
ESM 231		30	1.8	75	25	
ESM 203	160	Homogenous	-	-	-	
ESM 202		30	4.9	50	50	
ESM 212	350	Homogenous	-	-	-	
ESM 213		30	6.3	40	60	

Image analysis helps in accurately determining the portions of compression and sliding, yielded similar results for both drained and undrained conditions. This suggests that excess pore water pressure has a negligible effect on the proportions of compression and sliding in post-sliding phase (Table 7).

The calculation procedure for the contact area of the new failure plane in post-sliding phase in initial and final phase, is illustrated in Fig. 42 and Fig. 43.

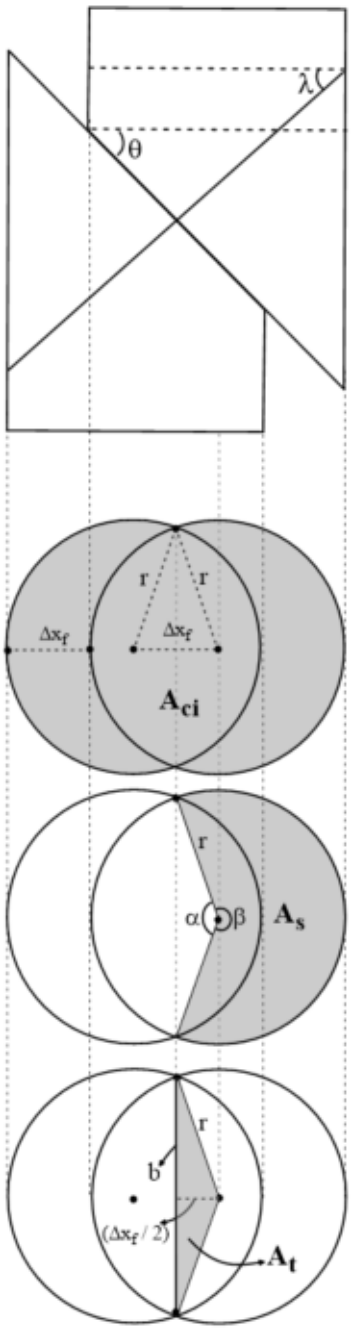

$$A_{\lambda i} = A_{ci} / \cos\lambda$$

$$A_{ci} = 2(A_s + A_t)$$

$$A_s = (\beta/360°)r^2$$

$$\beta = 2\pi - \alpha$$

$$\alpha = 2\arcsin(b / 2r)$$

$$A_t = (b / 2)(\Delta x_f / 2)$$

$$(b / 2)^2 = (r)^2 - (\Delta x_f / 2)^2$$

$$(b / 2) = \sqrt{(r)^2 - (\Delta x_f / 2)^2} = \sqrt{[r + (\Delta x_f / 2)][r - (\Delta x_f / 2)]}$$

Fig. 42) 2-D and 3-D view of the initial phase of the contact area of the new failure plane in the post-sliding phase and its calculations.

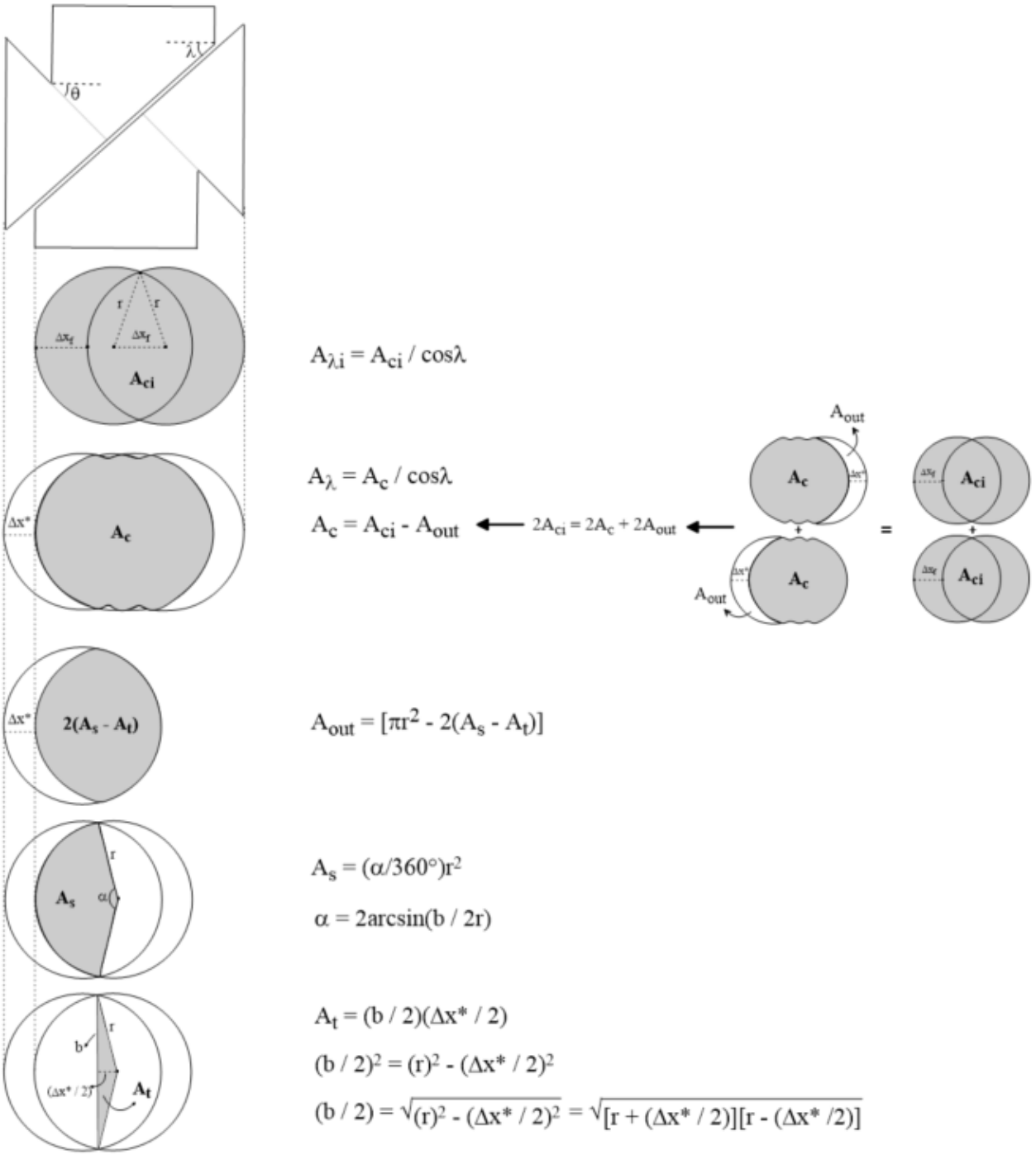

Fig. 43) 2-D and 3-D view after the initial phase of the contact area of the new failure plane in the post-sliding phase and its calculations.

4.4 Application of the Sliding Block Method on the *p,p′-q* Graphs

To incorporate the sliding block method into the *p,p′-q* stress path analysis, the first step is to adjust the calculation of the deviatoric stress, q. These modifications to q then clarify corresponding alterations in p and p'. The deviatoric stress is determined based on the load (in kN) acting on the average horizontal cross-sectional area of the specimen, represented as πr^2. In the pre-peak and pre-sliding phases, this cross-sectional area, and consequently the load F_q, align with the conventional methodology, indicating no deviations at these stages. However, from the peak or sliding onset point, variations diverge from conventional methods. Here, changes in the specimen's radius (r) are considered (Table 7), deviating from traditional approaches, and are essential in accurately reflecting the deviatoric stress in the specimen post-peak or post-sliding phases. For monitoring radius variations at every stage of the shearing condition in triaxial tests, ($\varepsilon_v = \varepsilon_{ac} + 2\varepsilon_r$) is consistently applied.

In this section, the internal friction angle (ϕ') and cohesion (c') are evaluated using the p'-q plane for both the Sliding Block Model (SBM) and the Conventional Method (CM). Fig. 45 displays results from the sliding onset, while Fig. 44 examines peaks from specimens that were either homogeneous or did not undergo sliding on pre-existing failure planes, demonstrating consistent results between the SBM and CM up to the sliding onset and at the peak stress points. Fig. 46 determines these parameters using the failure of the pre-existing failure planes through both SBM and CM. Fig. 47 further extends this analysis by considering the new failure formation during the post-sliding phase. Finally, Fig. 48 and Fig. 49 investigate these parameters in the post-peak phase, immediately after the stress drop and at 5% beyond the stress drop, utilizing both the SBM and CM, respectively (for more detailed information, see Appendix B).

4.4.1 Comparison between Conventional Method Results and Sliding Block Method

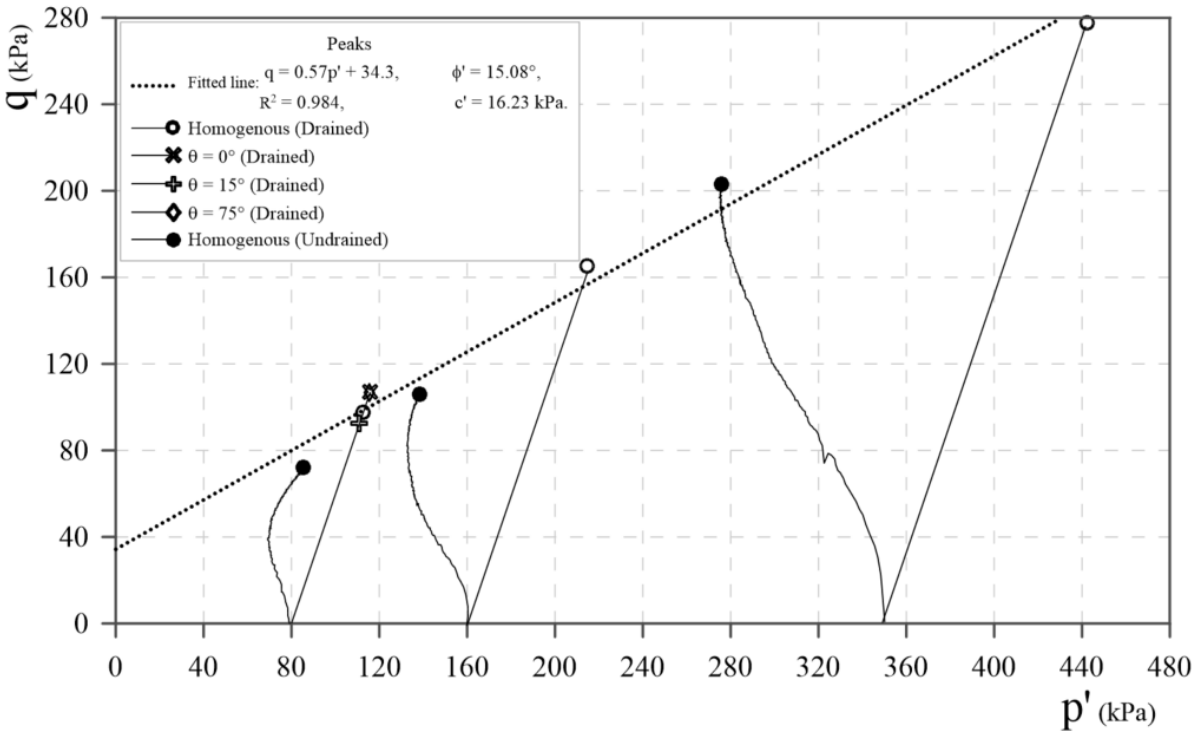

Fig. 44) Determination of Internal friction angle (ϕ') and cohesion (c') using peaks from both sliding block model (SBM) and Conventional Method (CM) perspectives on p'-q plane.

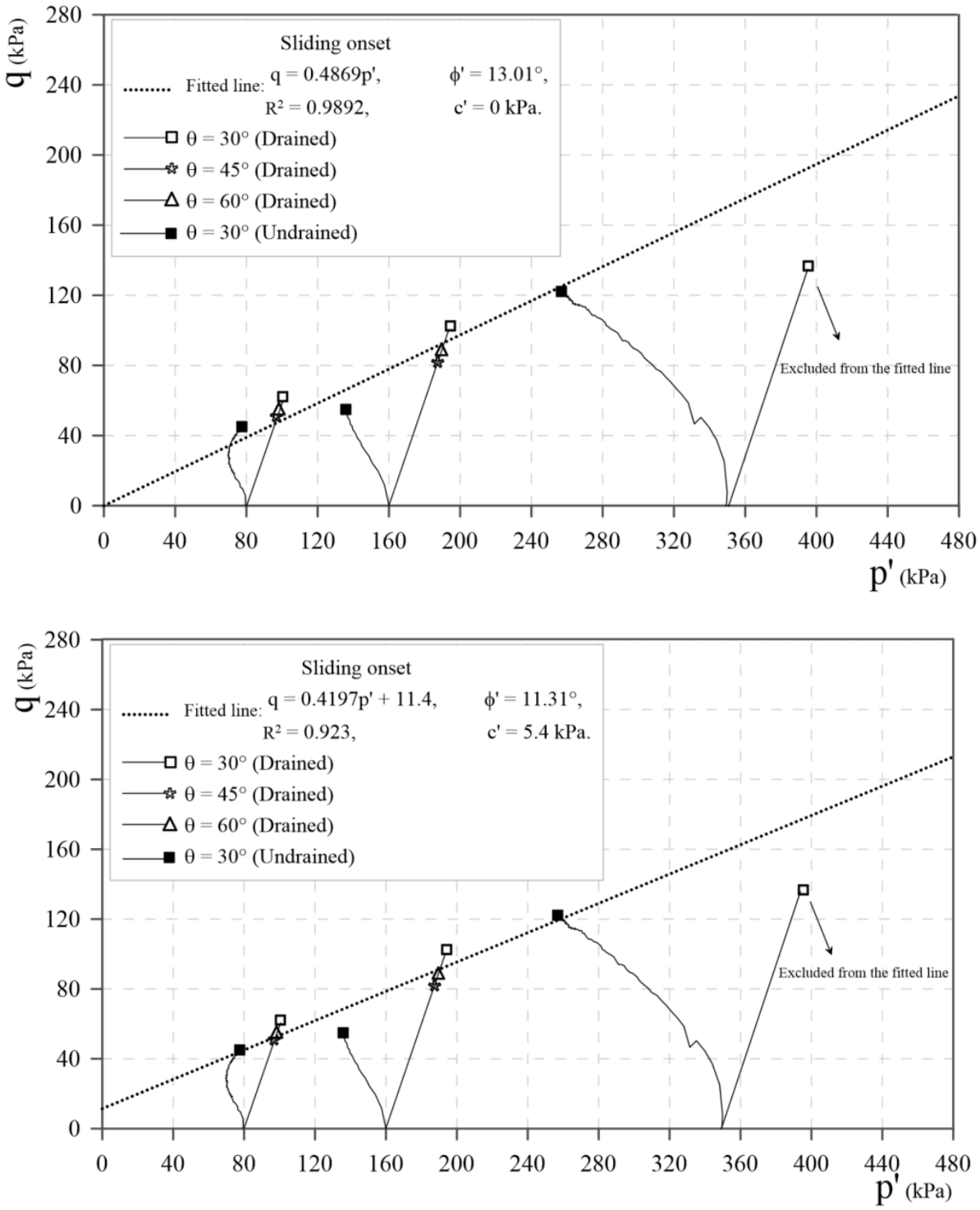

Fig. 45) Determination of Internal friction angle (ϕ') and cohesion (c') using sliding onset on the pre-existing failure planes from both sliding block model (SBM) and Conventional Method (CM) perspectives on p'-q plane (best fitted line and fitted line from origin.

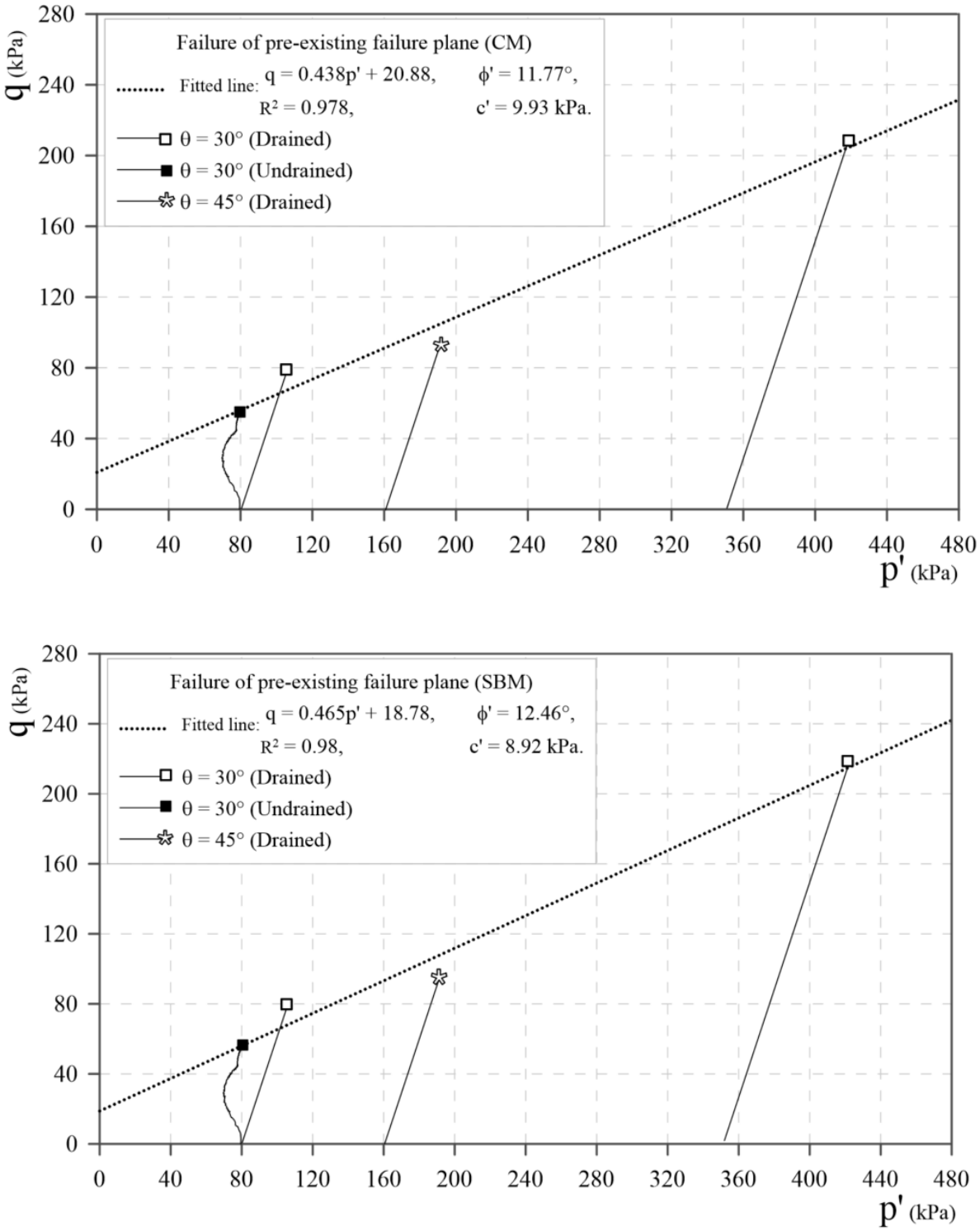

Fig. 46) Determination of Internal friction angle (ϕ') and cohesion (c') using the failure of the pre-existing failure plane from both sliding block model (SBM) and Conventional Method (CM) perspectives on p'-q plane.

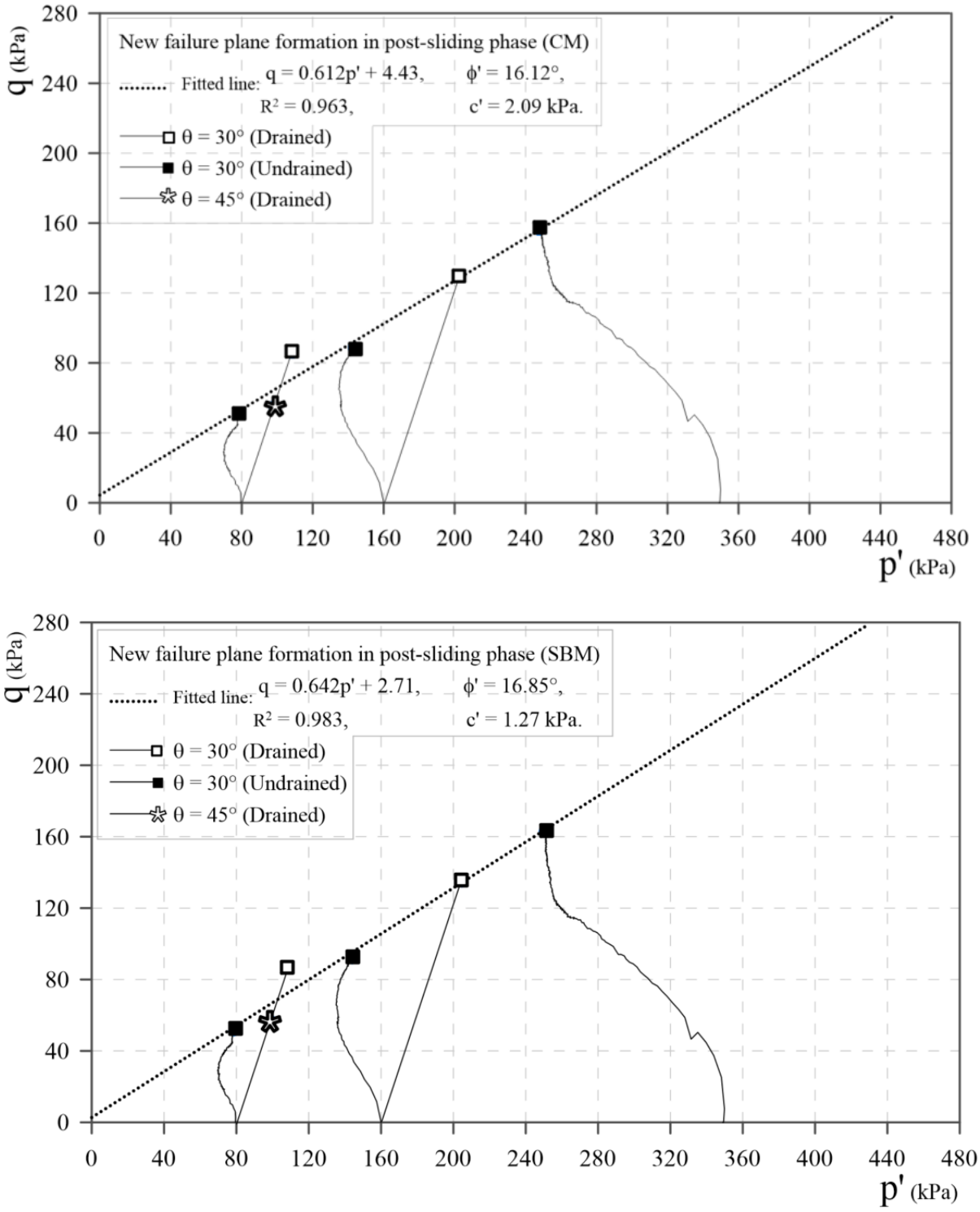

Fig. 47) Determination of Internal friction angle (ϕ') and cohesion (c') using new failure plane formation from both sliding block model (SBM) and Conventional Method (CM) perspectives on p'-q plane.

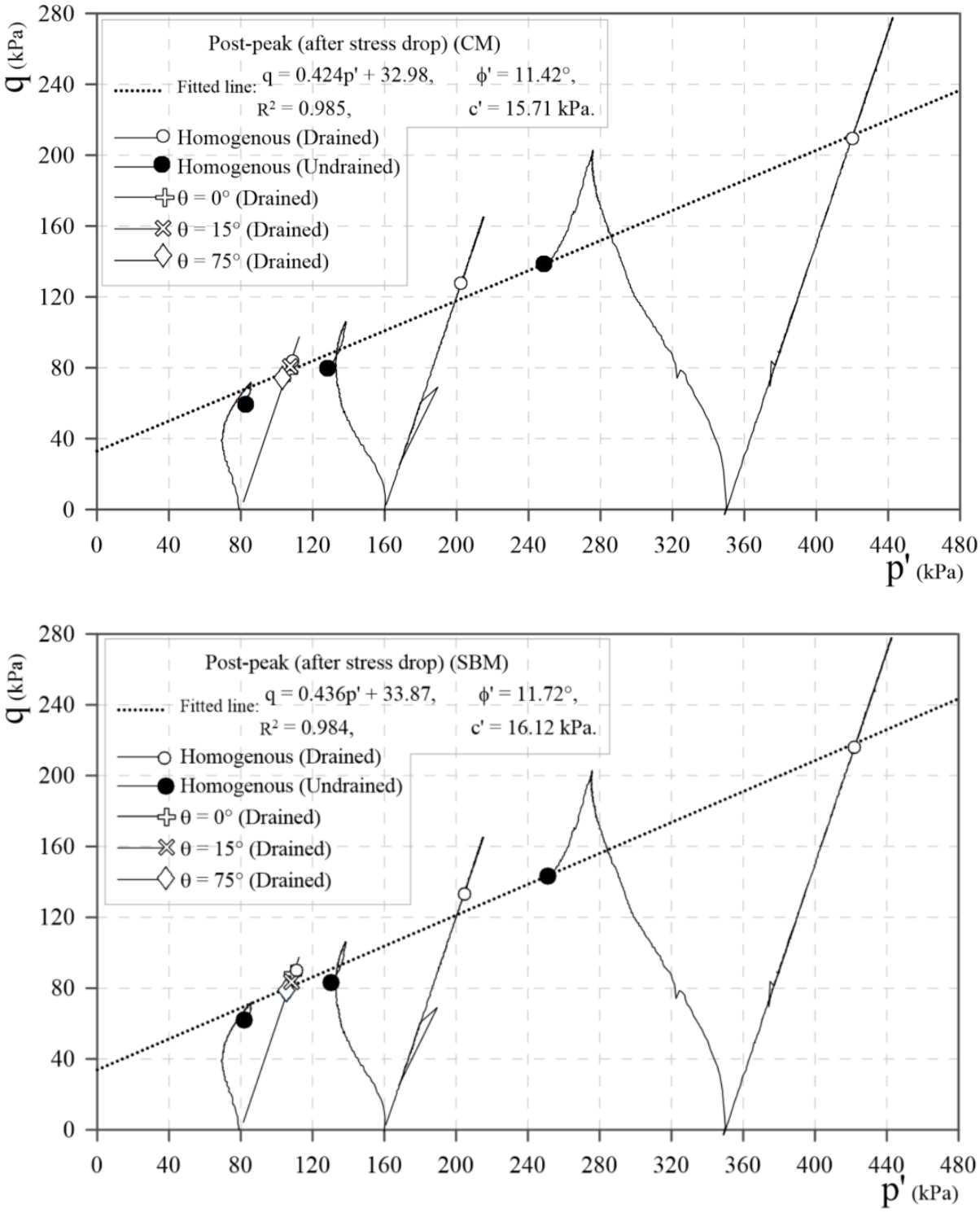

Fig. 48) Determination of Internal friction angle (ϕ') and cohesion (c') using post-peaks (after stress drop) from both sliding block model (SBM) and Conventional Method (CM) perspectives on p'-q plane.

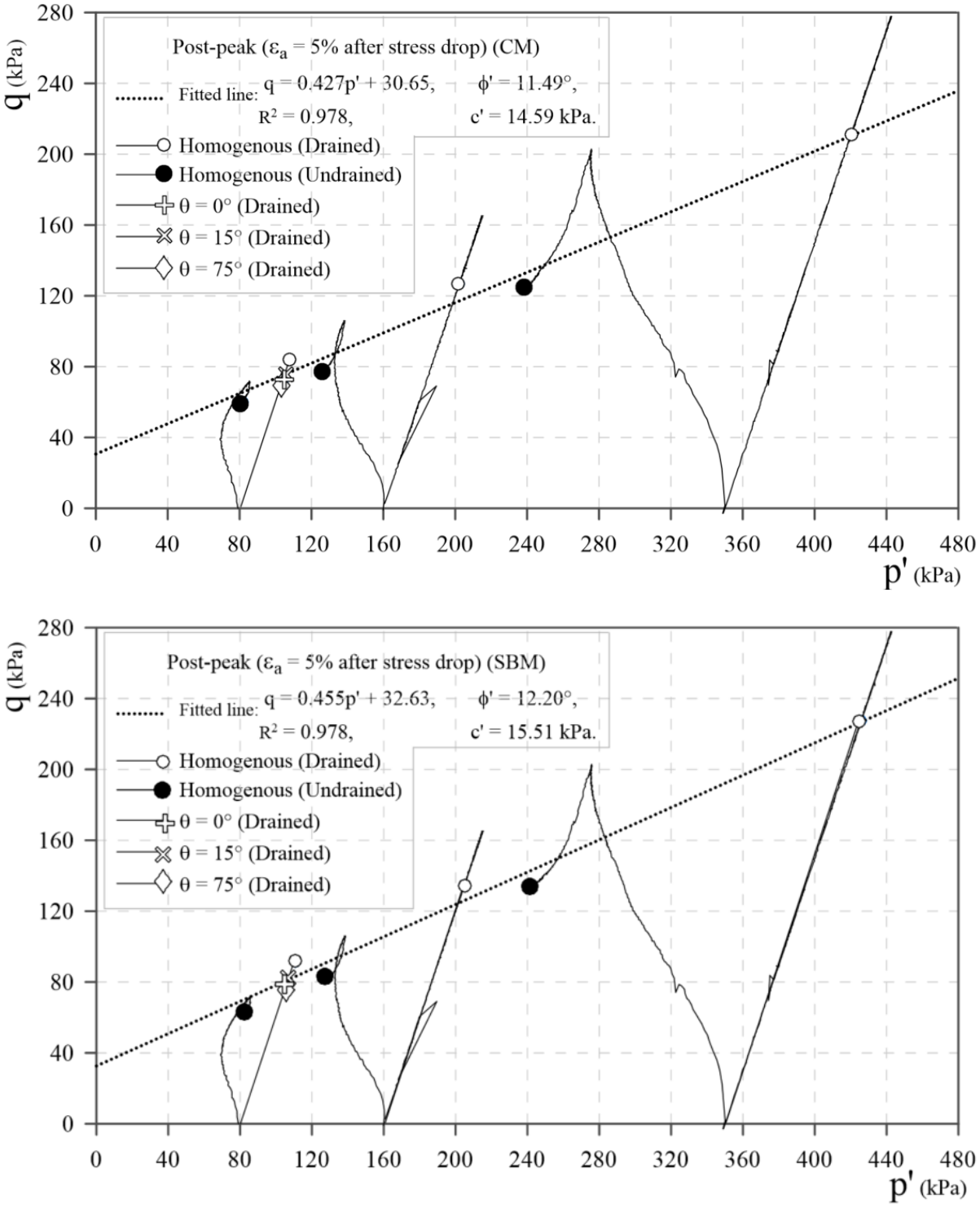

Fig. 49) Determination of Internal friction angle (ϕ') and cohesion (c') using post-peaks (5% after stress drop) from both sliding block model (SBM) and Conventional Method (CM) perspectives on p'-q plane.

4.5 Application of the Sliding Blocks Method on τ-σ'_n Graphs

In this section, the internal friction angle (ϕ') and cohesion (c') are determined using the τ-σ'_n plane for both the Sliding Block Model (SBM) and the Conventional Method (CM). Fig. 50 presents results obtained at the sliding onset, while Fig. 51 analyzes peaks from specimens that either did not experience sliding on their pre-existing failure planes or were homogeneous, illustrating consistent results between the SBM and CM up to the sliding onset and at the peaks. Fig. 52 exclusively utilizes the SBM for deriving these parameters. Fig. 53 extends this analysis by incorporating the effects of new failure formation during the post-sliding phase, considering friction between the top surface of the specimen and the porous stone. It is demonstrated that including friction in the analysis leads to more reliable results. Finally, Fig. 54 and Fig. 55 explore these parameters in the post-peak phase, immediately after the stress drop and at 5% beyond the stress drop, employing both the SBM and CM, respectively (for more detailed information, see Appendix B).

4.5.1 Comparison between Conventional Method Results and Sliding Block Method

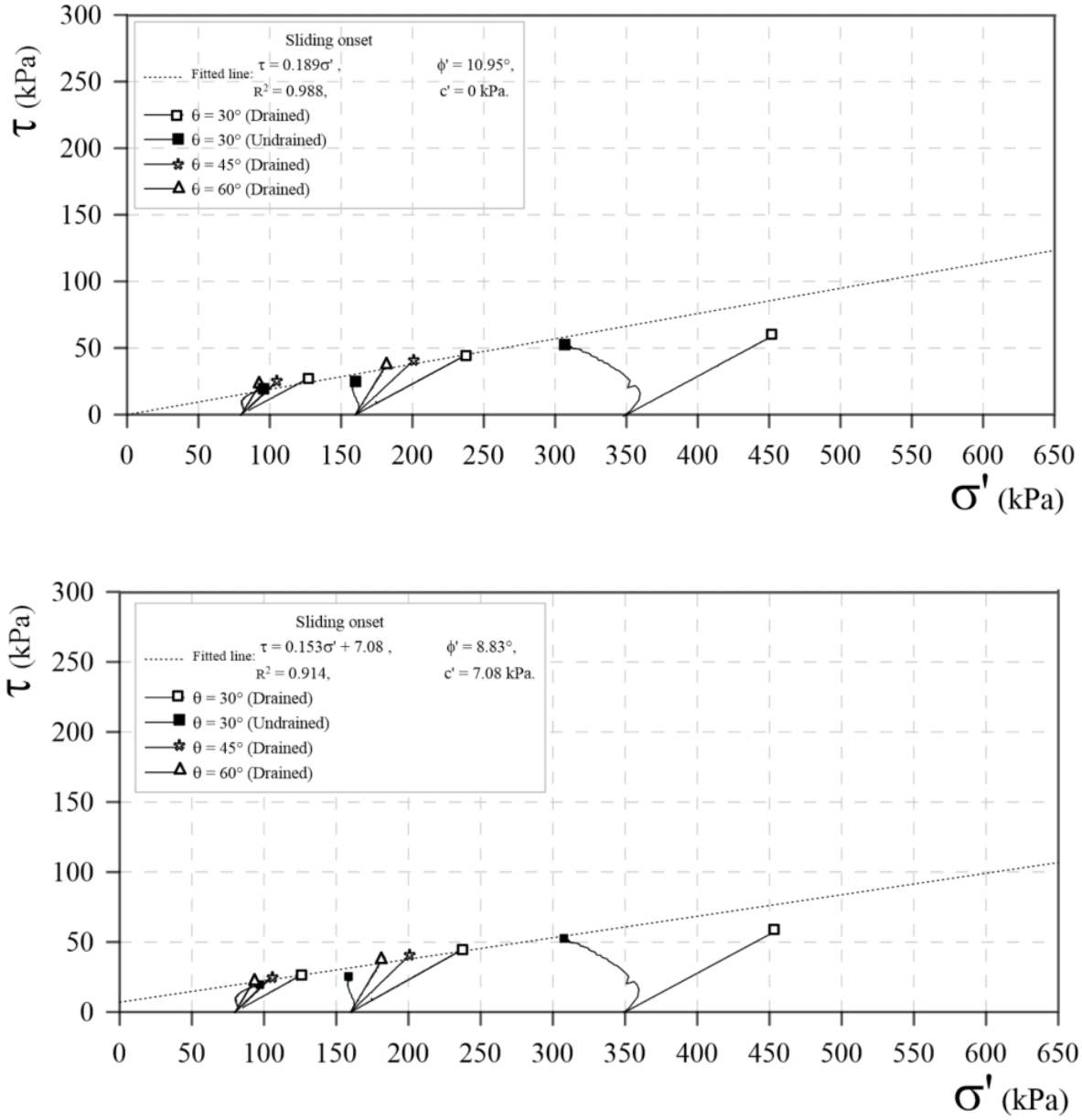

Fig. 50) Determination of Internal friction angle (ϕ') and cohesion (c') using sliding onset on the pre-existing failure planes from both sliding block model (SBM) and Conventional Method (CM) perspectives (best fitted line and fitted line from origin.

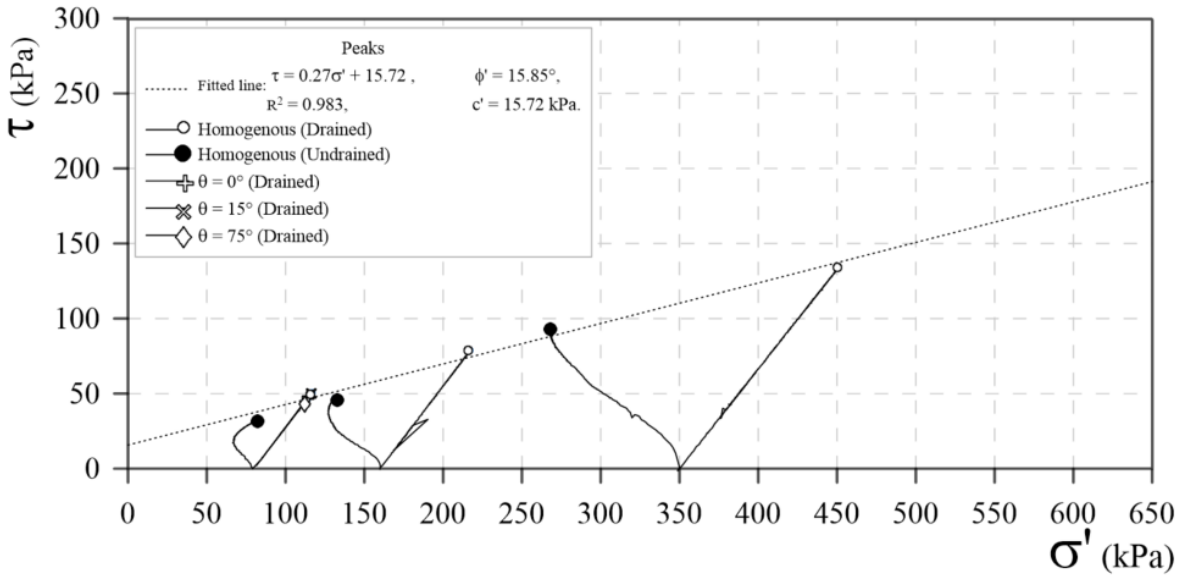

Fig. 51) Determination of Internal friction angle (ϕ') and cohesion (c') using peaks from both sliding block model (SBM) and Conventional Method (CM) perspectives.

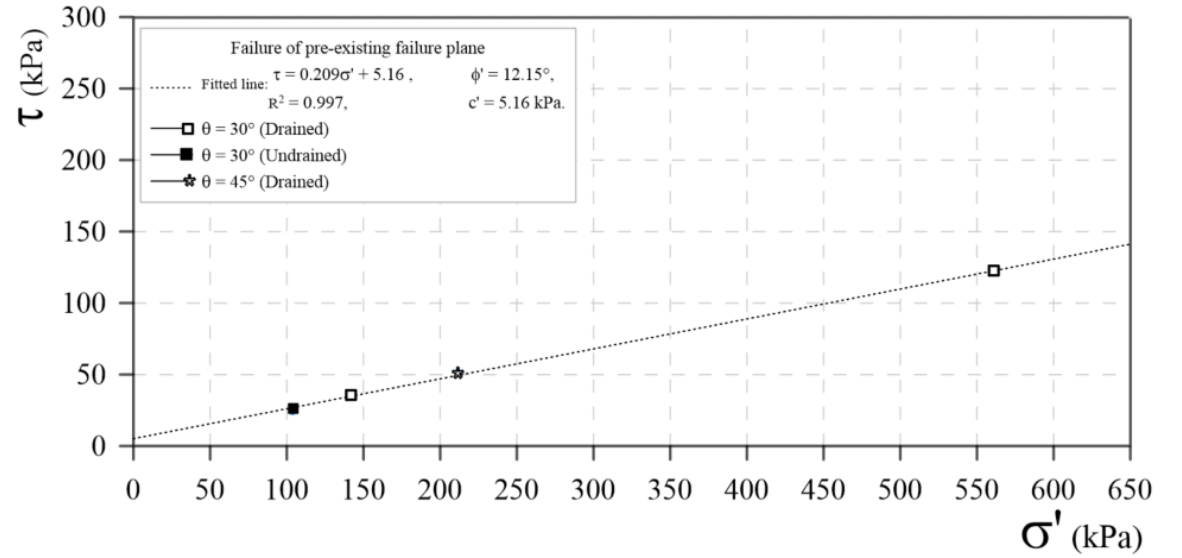

Fig. 52) Determination of Internal friction angle (ϕ') and cohesion (c') using the failure of the pre-existing failure plane from both sliding block model (SBM) and Conventional Method (CM) perspectives.

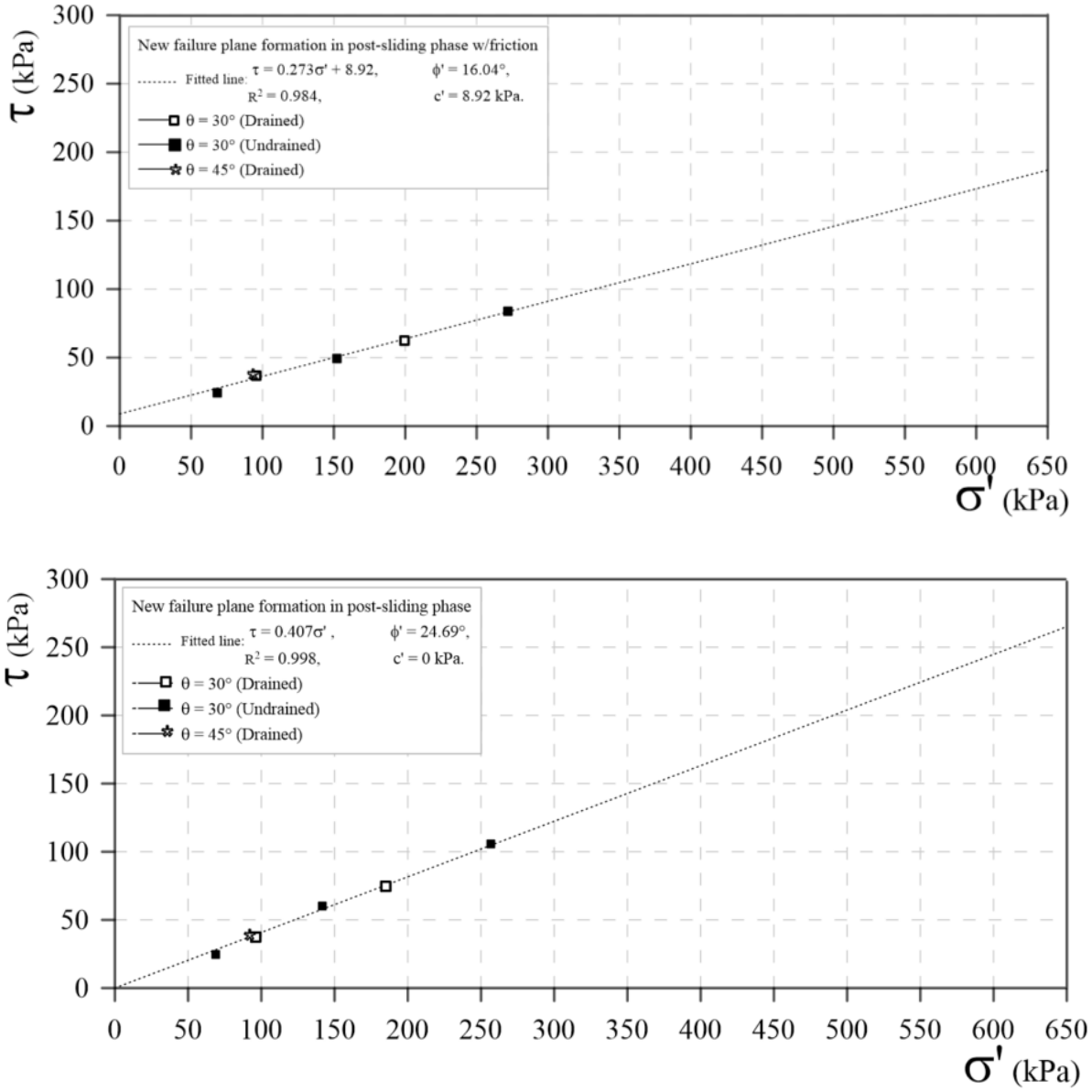

Fig. 53) Determination of Internal friction angle (ϕ') and cohesion (c') using new failure plane formation from both sliding block model (SBM) perspective with and without considering the friction on the top surface of the specimen.

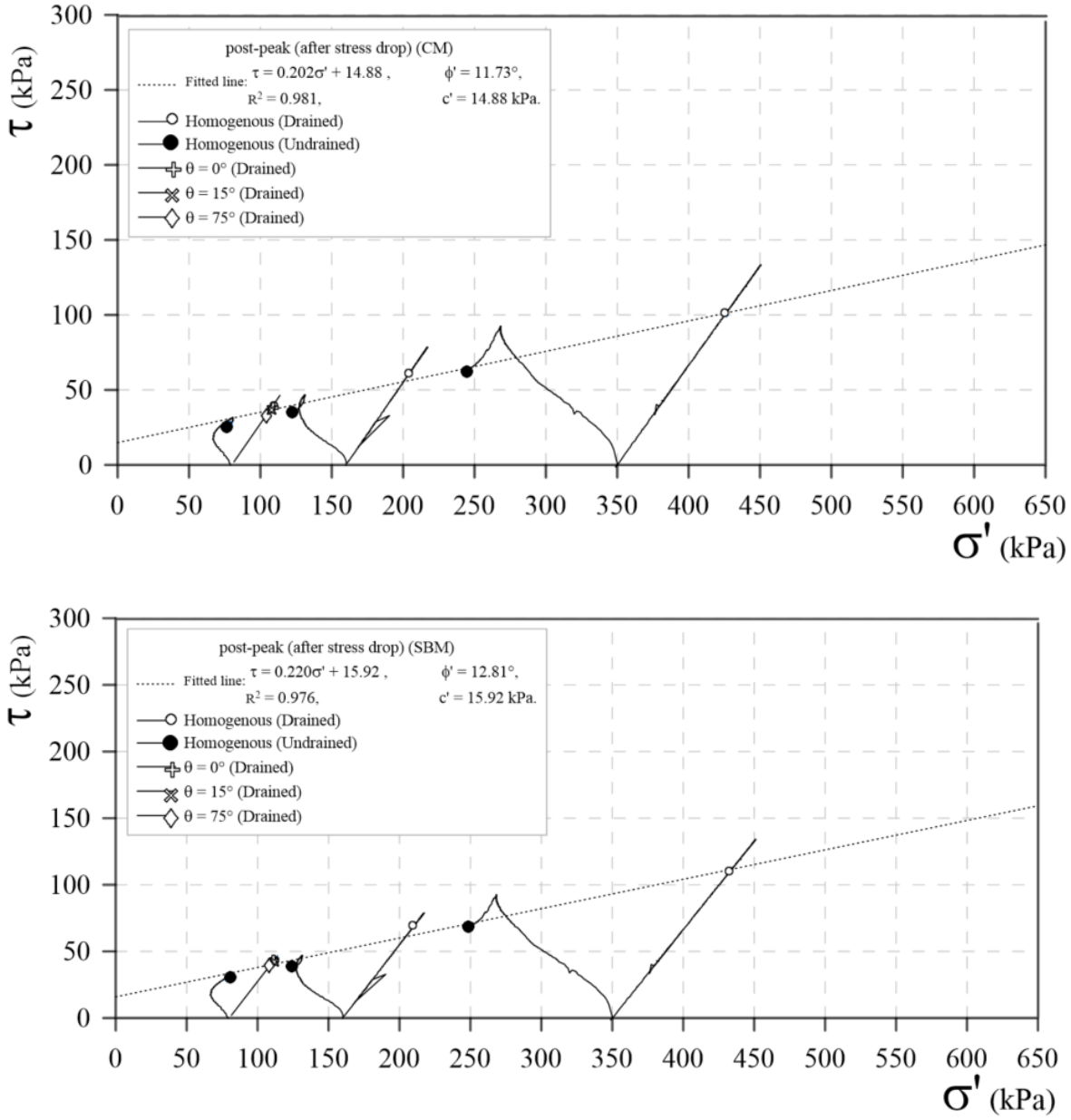

Fig. 54) Determination of Internal friction angle (ϕ') and cohesion (c') using post-peaks (after stress drop) from both sliding block model (SBM) and Conventional Method (CM) perspectives.

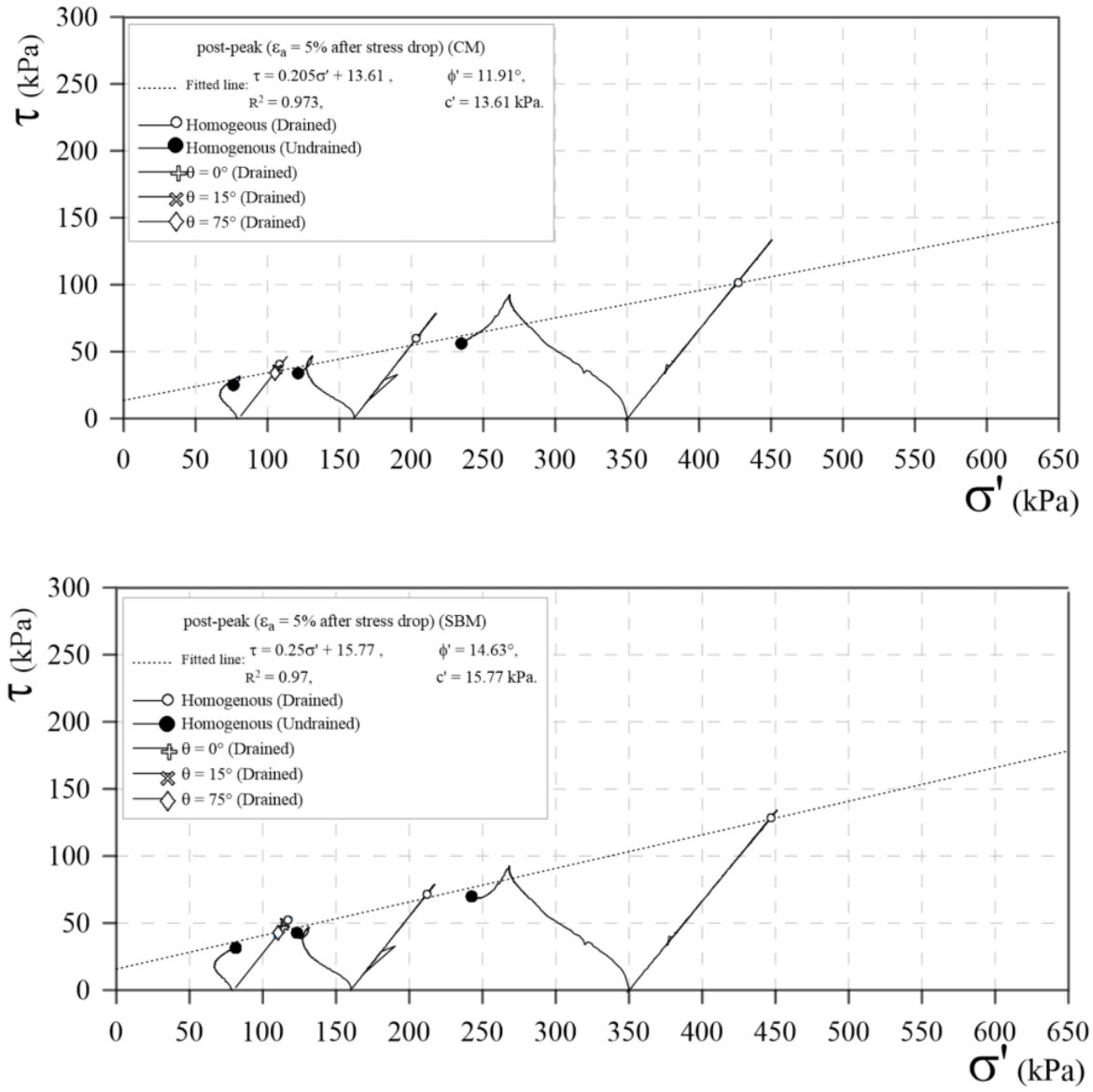

Fig. 55) Determination of Internal friction angle (ϕ') and cohesion (c') using post-peaks (5% after stress drop) from both sliding block model (SBM) and Conventional Method (CM) perspectives.

Chapter 5

Conclusion and perspective

This thesis has demonstrated that the sliding block method effectively interprets shearing behaviour data from triaxial testing, providing a more accurate representation of stress states. This method could potentially be applied to other shearing tests, due to its comprehensive area correction that accounts for the actual forces acting on each surface of the specimens. Enhancing the interpretation of shearing behaviour data from triaxial tests can significantly benefit from considering the friction between the specimen's top surface and the porous stone.

For homogeneous specimens, especially during the formation of new failure planes, this friction likely reaches the maximum potential between the top surface and the porous stone. Acknowledging this friction can refine interpretations made by the sliding block method, leading to more realistic results. In contrast, for specimens with pre-existing failure planes, the friction does not achieve its maximum until the onset of sliding. At this point, specimens with a 30-degree pre-existing failure plane exhibit higher friction compared to those with a 60-degree plane due to the onset of sliding occurring at higher deviatoric stresses for gentler inclinations.

Moreover, in the post-sliding phase, if a specimen is to form a new failure plane, the friction will peak, followed by the formation of a new failure plane. Conversely, for specimens with a 60-degree pre-existing failure plane, where a new failure plane does not form, the friction remains relatively constant post-sliding onset. This stability in friction levels contributes to the constant inclination of deviatoric stress observed throughout the test after the onset of sliding.

In conclusion, the sliding block method provides a realistic approach to interpreting data on shearing behaviour when the role of friction between the top surface of the specimen and the porous stone is taken into account. This inclusion enhances the method's accuracy and applicability to various geological and civil engineering scenarios.

References

ASTM International. (2016). Standard test method for performing laboratory direct shear strength tests of rock specimens under constant normal force (ASTM D5607-16). West Conshohocken, PA: ASTM International. https://doi.org/10.1520/D5607-16

ASTM International. (2021). ASTM D6467-21: Standard test method for torsional ring shear test to determine drained residual shear strength of fine-grained soils. https://doi.org/10.1520/D6467-21E01

Atapour, H., & Moosavi, M. (2013). Some effects of shearing velocity on the shear stress-deformation behaviour of hard–soft artificial material interfaces. *Geotechnical and Geological Engineering, 31*(5), 1603–1615. https://doi.org/10.1007/s10706-013-9687-6

Babanouri, N., Karimi Nasab, S., Baghbanan, A., & Mohamadi, H. R. (2011). Over-consolidation effect on shear behaviour of rock joints. *International Journal of Rock Mechanics and Mining Sciences, 48*(8), 1283–1291. https://doi.org/10.1016/j.ijrmms.2011.09.010

Bandis, S. C., Lumsden, A. C., & Barton, N. R. (1983). Fundamentals of rock joint deformation. *International Journal of Rock Mechanics and Mining Sciences & Geomechanics Abstracts, 20*(6), 249–268. https://doi.org/10.1016/0148-9062(83)90595-8

Barton, N. (1973). Review of a new shear-strength criterion for rock joints. *Engineering Geology, 7*(4), 287–332. https://doi.org/10.1016/0013-7952(73)90013-6

Barton, N. (1974). A review of the shear strength of filled discontinuities in rock. Norwegian Geotechnical Institute, Publication No. 105, Oslo.

Barton, N., & Choubey, V. (1977). The shear strength of rock joints in theory and practice. *Rock Mechanics, 10*(1–2), 1–54. https://doi.org/10.1007/BF01261801

Bieniawski, Z. T., Denkhaus, H. G., & Vogler, U. W. (1969). Failure of fractured rock. *International Journal of Rock Mechanics and Mining Sciences & Geomechanics Abstracts, 6*(3), 323-341. https://doi.org/10.1016/0148-9062(69)90009-6

Brace, W. F., & Byerlee, J. D. (1966). Stick-slip as a mechanism for earthquakes. *Science, 153*(3739), 990-992. https://doi.org/10.1126/science.153.3739.990

Burland, J. B. (1990). On the compressibility and shear strength of natural clays. *Geotechnique, 40*(3), 329–378. https://doi.org/10.1680/geot.1990.40.3.329

Byerlee, J. D., & Brace, W. F. (1968). Stick slip, stable sliding and earthquakes: Effects of rock type, pressure, strain rate, and stiffness. *Journal of Geophysical Research, 73*, 6031-6041. https://doi.org/10.1029/JB073i018p06031

Chandler, R. J. (1966). The measurement of residual strength in triaxial compression. *Géotechnique, 16*(3), 181-186.

Cheng, Q. (1997). Multifractal modeling and lacunarity analysis. *Mathematical Geology, 29*(7), 919–932. https://doi.org/10.1023/A:1022355723781

Coduto, D., Yeung, M., & Kitch, W. A. (2011). *Geotechnical engineering: Principles & practices* (2nd ed.). Prentice Hall.

Crawford, A. M., & Curran, J. H. (1981). The influence of shear velocity on the frictional resistance of rock discontinuities. *International Journal of Rock Mechanics and Mining Sciences & Geomechanics Abstracts, 18*(6), 505–515. https://doi.org/10.1016/0148-9062(81)90514-3

De Toledo, P. E., De Freitas, M. H., & Colcolough, G. (1993). Laboratory testing and parameters controlling the shear strength of filled rock joints. *Géotechnique, 43*(1), 1–19. https://doi.org/10.1680/geot.1993.43.1.1

Favero, V., Ferrari, A., & Laloui, L. (2018). Anisotropic behaviour of Opalinus clay through consolidated and drained triaxial testing in saturated conditions. *Rock Mechanics and Rock Engineering, 51*(5), 1305–1319. https://doi.org/10.1007/s00603-017-1398-5

Fernandes, F. C., de Moura, B. L. R., de Almeida, M. de S. S., Souza Junior, L. de O., Tarazona, S. F. M., de Almeida, M. C. F., & Barros, J. M. de C. (2023). Determination of the dynamic parameters of Speswhite kaolin with resonant column and centrifuge tests. *Soils and Rocks, 46*(2). https://doi.org/10.28927/SR.2023.013422

Georgiannou, V. N., & Burland, J. B. (2001). A laboratory study of post-rupture strength. *Géotechnique, 51*(8), 665-675.

Goodman, R. E. (1970). The deformability of joints. In *Determination of the In Situ Modulus of Deformation of Rock* (pp. 174–196). ASTM STP 447, American Society for Testing Materials. https://doi.org/10.1520/STP29147S

Grasselli, G. (2002). Shear strength of rock joints based on quantified surface description. *Rock Mechanics and Rock Engineering, 35*(1), 1-18. https://doi.org/10.1007/s00603-002-0021-6

Grasselli, G., & Egger, P. (2003). Constitutive law for the shear strength of rock joints based on three-dimensional surface parameters. *International Journal of Rock Mechanics and Mining Sciences, 40*(1), 25–40. https://doi.org/10.1016/S1365-1609(02)00101-6

Haque, A. (1999). Shear behaviour of soft rock joints under constant normal stiffness.

Head, K. H., & Epps, R. J. (2006). *Manual of soil laboratory testing-effective stress tests* (3rd ed., Vol. 3).

Heuze, F. E. (1979). Dilatant effects of rock joints. Proceedings of the 4th ISRM Congress.

Indraratna, B., & Haque, A. (1997). Experimental study of shear behaviour of rock joints under constant normal stiffness conditions. *International Journal of Rock Mechanics and Mining Sciences, 34*(3-4), 141.e1-141.e14. https://doi.org/10.1016/S1365-1609(97)00068-3

International Society for Rock Mechanics Commission on Standardization of Laboratory and Field Tests. (1978). *International Journal of Rock Mechanics and Mining Sciences & Geomechanics Abstracts, 15*(6), 319–368. https://doi.org/10.1016/0148-9062(78)91472-9

Jaeger, J. C., Cook, N. G. W., & Zimmerman, R. (2007). *Fundamentals of rock mechanics* (4th ed.). Blackwell Publishing Limited. ISBN: 978-0632057597.

Jiang, Q., Feng, X., Gong, Y., Song, L., Ran, S., & Cui, J. (2016a). Reverse modelling of natural rock joints using 3D scanning and 3D printing. *Computers and Geotechnics, 73*, 210-220. https://doi.org/10.1016/j.compgeo.2015.12.004

Jiang, Q., Feng, X., Song, L., Gong, Y., Zheng, H., & Cui, J. (2016b). Modeling rock specimens through 3D printing: Tentative experiments and prospects. *Acta Mechanica Sinica, 32*, 101-111. https://doi.org/10.1007/s10409-015-0501-7

Jiang, Y., Xiao, J., Tanabashi, Y., & Mizokami, T. (2004). Development of an automated servo-controlled direct shear apparatus applying a constant normal stiffness condition. *International Journal of Rock Mechanics and Mining Sciences, 41*(2), 275–286. https://doi.org/10.1016/j.ijrmms.2003.08.004

Johnston, I., Lam, T., & Williams, A. (1987). Constant normal stiffness direct shear testing for socketed pile design in weak rock. *Geotechnique, 37*(1), 83-89. https://doi.org/10.1680/geot.1987.37.1.83

Kanji, M. (1974). Unconventional laboratory tests for the determination of the shear strength of soil-rock contacts. *Proceedings of the 3rd Congress of the International Society for Rock Mechanics*, 241–247.

Kim, D. H., Gratchev, I., Balasubramaniam, A., & Chung, M. (2015). Determination of mobilized asperity parameters to define rock joint shear strength in low normal stress conditions. In *Proceedings of the 12th ANZ Conference on Geomechanics*, Wellington, New Zealand (pp. 1145-1152).

Kodikara, J. K., & Johnston, I. W. (1994). Shear behaviour of irregular triangular rock-concrete joints. *International Journal of Rock Mechanics and Mining Sciences & Geomechanics Abstracts, 31*, 313-322. https://doi.org/10.1016/0148-9062(94)92211-8

Ladanyi, B., & Archambault, G. (1977). Shear strength and deformability of filled indented joints. *International Symposium on the Geotechnics of Structurally Complex Formations*, 317–326.

Lade, P. V. (2016). *Triaxial testing of soils*. John Wiley & Sons, Ltd.

Li, Y., Oh, J., Mitra, R., & Hebblewhite, B. (2015). Experimental studies on the mechanical behaviour of rock joints with various openings. *Rock Mechanics and Rock Engineering, 48*(2), 437-447. https://doi.org/10.1007/s00603-014-0597-6

Maerz, N. H., Franklin, J. A., & Bennett, C. P. (1990). Joint roughness measurement using shadow profilometry. *International Journal of Rock Mechanics and Mining Sciences & Geomechanics Abstracts, 27*(5), 329–343. https://doi.org/10.1016/0148-9062(90)92708-M

Maksimovic, M. (1996). The shear strength components of a rough rock joint. *International Journal of Rock Mechanics and Mining Sciences & Geomechanics Abstracts, 33*(8), 769e83. https://doi.org/10.1016/0148-9062(96)00051-8

McGarr, A., & Fletcher, J. B. (2004). Stick-slip as a mechanism for earthquakes revisited. *Bulletin of the Seismological Society of America, 94*(5), 1854-1860. https://doi.org/10.1785/0120040121

Mochizuki, A., Ma, X., & Sokkheang, S. (2011). Failure of a cut slope and deterioration of shear strength due to weathering. In *Proceedings of the TC302 Symposium Osaka 2011: International Symposium on Backwards Problem in Geotechnical Engineering and Monitoring of Geo-Construction.*

Mulabdic, M. (1993). Area correction in triaxial testing. Linköping: Statens geotekniska institut. ISSN 1100-6692.

Mylvaganam, J. (2007). Shear behaviour of normally consolidated and overconsolidated infilled rock joints under undrained triaxial conditions [PhD Thesis]. University of Wollongong.

Papaliangas, T., Hencher, S. R., Lumsden, A. C., & Manolopoulou, S. (1993). The effect of frictional fill thickness on the shear strength of rock discontinuities. *International Journal of Rock Mechanics and Mining Sciences & Geomechanics Abstracts, 30*(2), 81–91. https://doi.org/10.1016/0148-9062(93)90702-F

Patton, F. D. (1966). Multiple modes of shear failure in rock. *Proceedings of the 1st ISRM Congress.*

Pellet, F., Keshavarz, M., & Boulon, M. (2013). Influence of humidity conditions on shear strength of clay rock discontinuities. *Engineering Geology, 157*, 33–38.

Phien-Wej, N., Shrestha, U., & Rantucci, G. (1990). Effect of infill thickness on shear behaviour of rock joints. *Rock Joints*, 289–294. https://doi.org/10.1097/00004872-198412000-00012

Pilkey, W. D., Pilkey, D. F., & Peterson, R. E. (2008). *Peterson's stress concentration factors* (3rd ed.). John Wiley & Sons.

Premadasa, W. N. (2013). The influence of infill saturation on the shear strength of soil-infilled rock joints [Doctor of Philosophy (Ph.D.)]. University of Wollongong.

Shrivastava, A. K., & Rao, K. S. (2015). Shear behaviour of rock joints under CNL and CNS boundary conditions. *Geotechnical and Geological Engineering, 33*(5), 1205–1220. https://doi.org/10.1007/s10706-015-9896-2

Skempton, A. W. (1964). Long-term stability of clay slopes, Fourth Rankine Lecture. *Geotechnique, 14*(2), 77–102. https://doi.org/10.1680/geot.1964.14.2.77

Skinas, C., Bandis, S., & Demiris, C. (1990). Experimental investigations and modelling of rock joint behaviour under constant stiffness. In *Proceedings of Rock Joints, Loen, Norway* (pp. 301-308).

Stark, T. D., & Eid, H. T. (1994). Drained residual strength of cohesive soils. *Journal of Geotechnical Engineering, 120*(5), 856-871.

Stark, T. D., & Hussain, M. (2010). Drained residual strength for landslides. In *GeoFlorida 2010: Advances in Analysis, Modeling & Design (GSP 199)* (pp. 3217-3226). American Society of Civil Engineers.

Tang, Z. C., & Wong, L. N. Y. (2016). New criterion for evaluating the peak shear strength of rock joints under different contact states. *Rock Mechanics and Rock Engineering, 49*(4), 1191–1199. https://doi.org/10.1007/s00603-015-0811-1

Tiwari, R. P., & Rao, K. S. (2006). Post failure behaviour of a rock mass under the influence of triaxial and true triaxial confinement. *Engineering Geology, 84*, 112-129.

Tse, R., & Cruden, D. M. (1979). Estimating joint roughness coefficients. *International Journal of Rock Mechanics and Mining Sciences & Geomechanics Abstracts, 16*(5), 303–307. https://doi.org/10.1016/0148-9062(79)90241-9

Tutluoglu, L., Öge, I. F., & Karpuz, C. (2015). Relationship between pre-failure and post-failure mechanical properties of rock material of different origin. *Rock Mechanics and Rock Engineering, 48*(1), 121-141. https://doi.org/10.1007/s00603-014-0549-1

Urmi, Z. A., Saeidi, A., Yerro, A., & Chavali, R. V. P. (2023). Prediction of post-peak stress-strain behaviour for sensitive clays. *Engineering Geology, 323*, 107221.

Xie, H. P., & Pariseau, W. G. (1995). Fractal estimation of joint roughness coefficients. *International Journal of Rock Mechanics and Mining Sciences & Geomechanics Abstracts*.

Yang, Z. Y., Lo, S. C., & Di, C. C. (2001). Reassessing the joint roughness coefficient (JRC) estimation using Z2. *Rock Mechanics and Rock Engineering, 34*(3), 243–251. https://doi.org/10.1007/s006030170012

Zandarin, M. T., Alonso, E., & Olivella, S. (2013). A constitutive law for rock joints considering the effects of suction and roughness on strength parameters. *International Journal of Rock Mechanics and Mining Sciences, 60*, 333-344.

Zhang, H., & Li, C. C. (2019). Effects of confining stress on the post-peak behaviour and fracture angle of Fauske marble and Iddefjord granite. *Rock Mechanics and Rock Engineering, 52*, 1377–1385. https://doi.org/10.1007/s00603-018-1695-7

Zhang, X., Jiang, Q., Chen, N., Wei, W., & Feng, X. (2016). Laboratory investigation on shear behaviour of rock joints and a new peak shear strength criterion. *Rock Mechanics and Rock Engineering, 49*(9), 3495–3512. https://doi.org/10.1007/s00603-016-1012-2

Appendix A: Force Balance Revision

Appendix A provides detailed explanations relevant to Section 4.2. It serves as a verification resource for the equations, enhancing their reliability and offering insights into the derivation of each formula.

To derive Equations 4.1 and 4.2 from Equations 3.8 and 3.9, given that $\sigma_1 = \sigma_3 + q$, the derivation process is as follows:

$$\sigma_\theta = \frac{1}{2}(\sigma_1 + \sigma_3) + \frac{1}{2}(\sigma_1 - \sigma_3)cos2\theta \tag{3.8}$$

$$\tau_\theta = \frac{1}{2}(\sigma_1 - \sigma_3)sin2\theta \tag{3.9}$$

$$\sigma_\theta = \frac{1}{2}(\sigma_3 + q + \sigma_3) + \frac{1}{2}(\sigma_3 + q - \sigma_3)cos2\theta$$

$$\tau_\theta = \frac{1}{2}(\sigma_3 + q - \sigma_3)sin2\theta$$

$$\sigma_\theta = (\sigma_3) + \left[\frac{1}{2}(q)(1 + cos2\theta)\right] \tag{4.1}$$

$$\tau_\theta = \frac{1}{2}(q)sin2\theta \tag{4.2}$$

The derivation process for Equations 4.7, 4.8, 4.9, and 4.10 is as follows:

The force equilibrium can be shown as Fig. A1, where $\sigma_3 = (\sigma_3)_{L1} = (\sigma_3)_{L2} = (\sigma_3)_{TS}$.

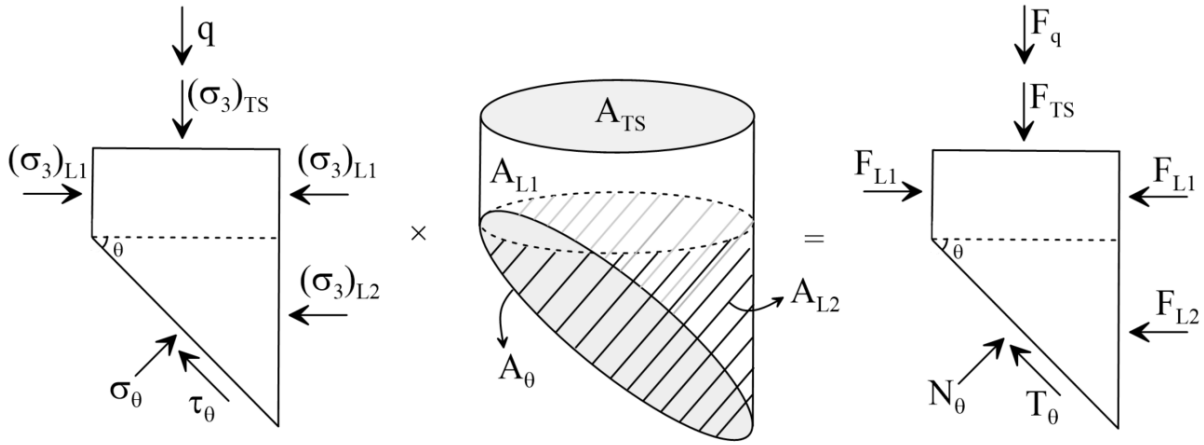

Fig. A1) Stresses acting on the top block of specimen and their acting surfaces which they can be shown as force.

It can be written in 3 phases to cover all the phases of shearing stage (confining pressure is constant and equal to σ_3), 1) initial phase ($q = 0$), 2) pre-peak or pre-sliding phase ($q > 0$), and 3) post-peak or post-sliding phase ($q > 0$):

1) Initial phase ($q = 0$):

$\sigma_\theta = (\sigma_\theta)_c \rightarrow N_\theta = N_c$, and $\tau_\theta = 0 \rightarrow T_\theta = 0$, so the force equilibrium is the same as the Fig. A2, where N_{ch} and N_{cv} are the horizontal and vertical components of N_c, respectively.

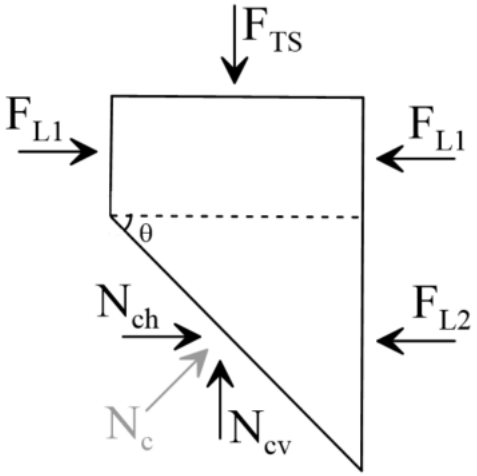

Fig. A2) Forces acting on the top block in the initial phase of shearing stage (q=0).

From this force equilibrium for the initial phase,

Horizontal: $N_{ch} - F_{L2} = 0 \rightarrow N_{ch} = F_{L2}$,

Vertical: $N_{cv} - F_{TS} = 0 \rightarrow N_{cv} = F_{TS}$.

$\rightarrow N_c = \left(\frac{N_{cv}}{cos\theta}\right) = \left(\frac{N_{ch}}{sin\theta}\right) = \left(\frac{F_{TS}}{cos\theta}\right) = \left(\frac{F_{L3}}{sin\theta}\right)$

$\rightarrow N_\theta = \left(\frac{F_{TS}}{cos\theta}\right) = \left(\frac{F_{L3}}{sin\theta}\right)$, and $T_\theta = 0$.

Note:

According to $N_{ch} = F_{L2}$, and equal σ_3 in all directions, $\rightarrow (\sigma_\theta)_{ch} \times (A_\theta)_h = (\sigma_3)_{L2} \times (A_{L2})'$.

$(\sigma_\theta)_{ch} = (\sigma_3)_{L2} \rightarrow (A_\theta)_h = (A_{L2})'$, $(A_\theta)_{ch}$ is the effective area for horizontal component of force on the failure plane (N_{ch}).

$(A_{L2})'$ is the effective area of the force F_{L2}. This means that the schematic view of the effective area of force F_{L2} was not shown correctly in Fig. A2. To find the correct effective area of F_{L2}, by referring to the equation $(A_\theta)_h = (A_{L2})'$, it is evident that the effective area for horizontal component of force on the failure plane (N_{ch}), is equal to effective area of the force (F_{L2}), and it is shown in the Fig. A3.

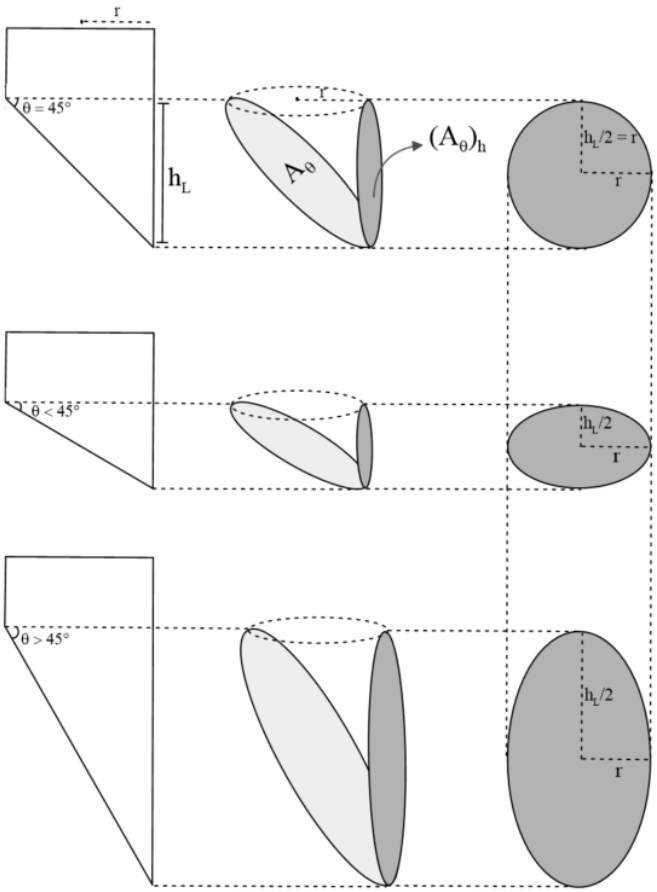

Fig. A3) Effective area of the lateral force (F_{L2}).

In Fig. A3, the projections of the contact area onto a flat lateral surface are depicted. Fig. A4 illustrates the approach of considering a flat surface in place of the lateral surface, clearly demonstrating that the projections shown in Fig. A3 are equivalent to those in Fig. A4.

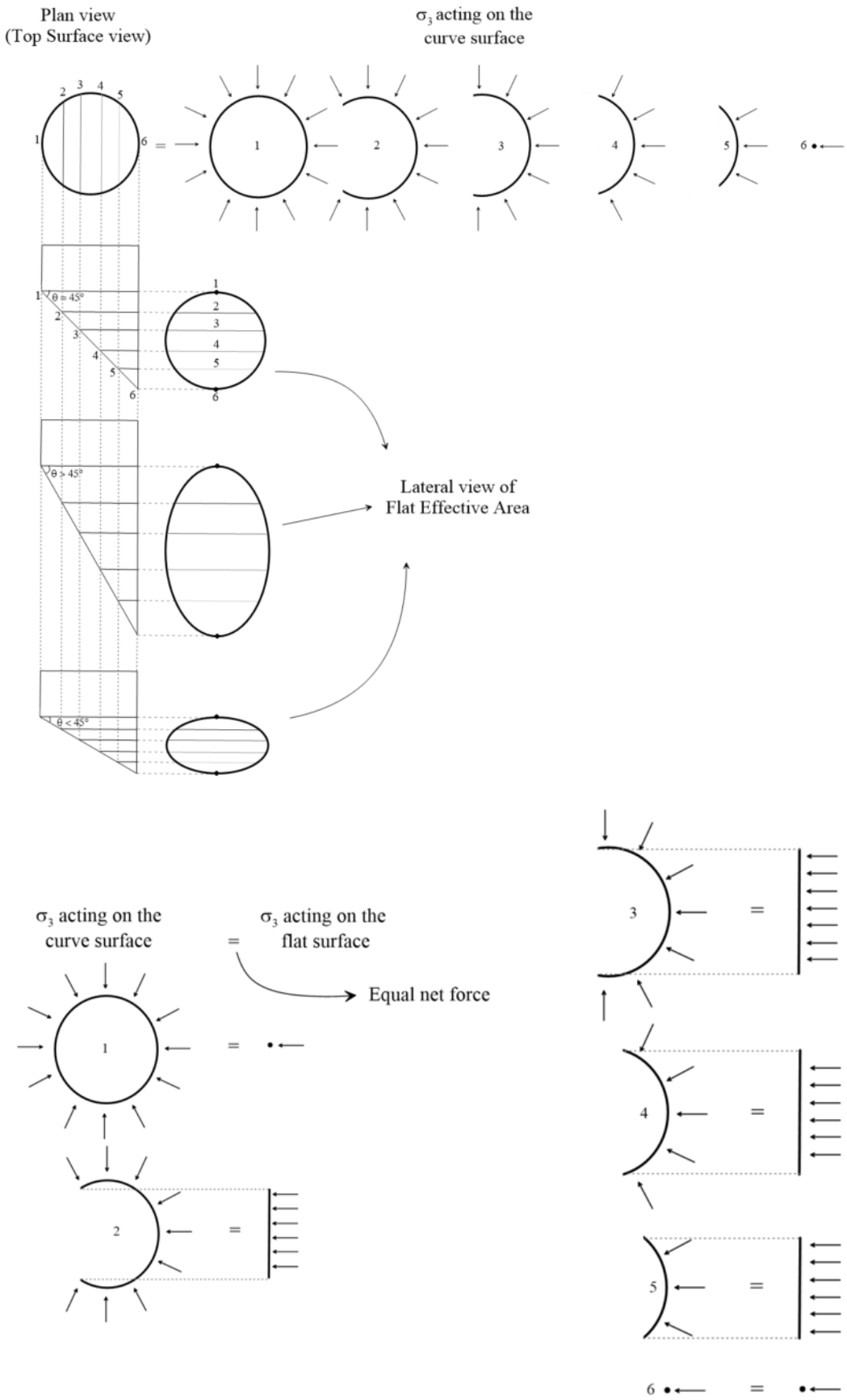

Fig. A4) Effective area of the lateral force (F_{L2}) (detailed explanation).

By looking at the Fig. A3 and Fig. A4, it can be concluded that the effective area for F_{L3}, is equal to an ellipse which $(h_L = 2rtan\theta)$.

Also, according to $N_{cv} = F_{TS}$, and equal σ_3 in all directions, $\rightarrow (\sigma_\theta)_{cv} \times (A_\theta)_v = (\sigma_3)_{TS} \times A_{TS}$.

$(\sigma_\theta)_{cv} = (\sigma_3)_{TS} \rightarrow (A_\theta)_v = A_{TS}$. $(A_\theta)_v$ the effective area for vertical component of force on the failure plane (N_{cv}), which can be seen in the Fig. A5:

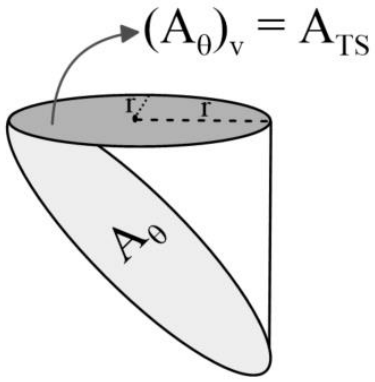

Fig. A5) Effective area of vertical component of force.

To sum up,

$F_{TS} = \sigma_3 \times A_{TS}$, and $F_{L3} = \sigma_3 \times (A_{L3})'$,

$A_{TS} = (A_\theta)_v = A_\theta \times cos\theta$,

$(A_{L2})' = (A_\theta)_h = A_\theta \times sin\theta$,

On the other hand, $N_\theta = N_c = \frac{F_{TS}}{cos\theta} = \frac{F_{L2}}{sin\theta}$

$\rightarrow N_\theta = N_c = \frac{\sigma_3 \times A_\theta \times cos\theta}{cos\theta} = \frac{\sigma_3 \times A_\theta \times sin\theta}{sin\theta} = \sigma_3 \times A_\theta$

$\rightarrow \sigma_\theta = \frac{N_\theta}{A_\theta}$, and $\tau_\theta = \frac{T_\theta}{A_\theta}$

$\rightarrow \sigma_\theta = \frac{\sigma_3 \times A_\theta}{A_\theta} = \sigma_3$, and $\tau_\theta = \frac{0}{A_\theta} = 0$.

2) pre-peak or pre-sliding phase ($q > 0$):

$\sigma_\theta = (\sigma_\theta)_c + (\sigma_\theta)_q \rightarrow N_\theta = N_c + N_q$, and $\tau_\theta = (\tau_\theta)_q \rightarrow T_\theta = T_q$, so the force equilibrium can be shown as the Fig. A6,

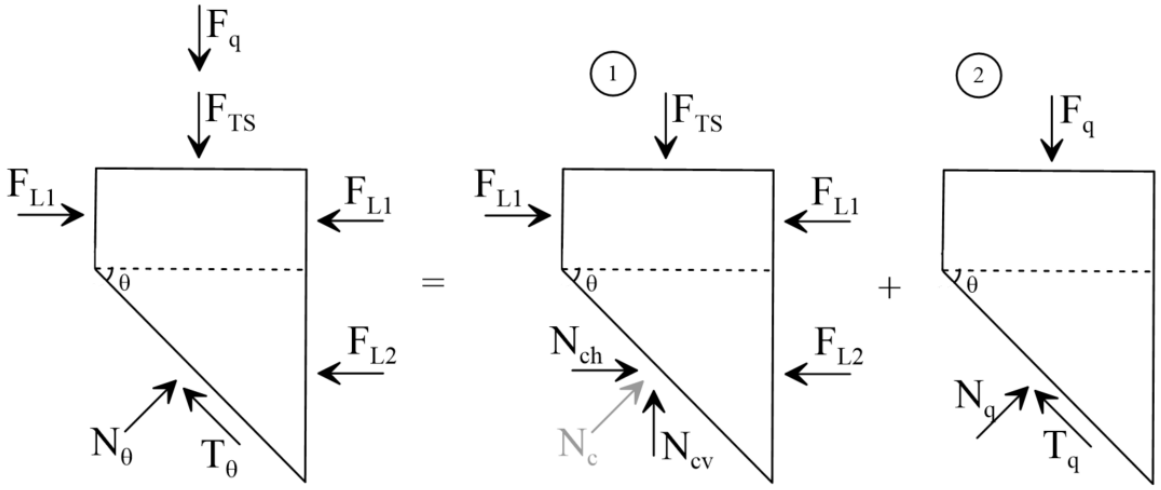

Fig. A6) Forces acting on the top block after the initial phase of shearing stage (q>0).

Because ① in Fig. A6, is equal to Fig. A2, so $N_c = \frac{F_{TS}}{cos\theta} = \frac{F_{L2}}{sin\theta} = \sigma_3 \times A_\theta$, so by looking at ② in Fig. A6, it can be concluded that:

$N_q = F_q \times cos\theta$, and $T_q = F_q \times sin\theta$,

So, $N_\theta = N_c + N_q \rightarrow N_\theta = (\sigma_3 \times A_\theta) + \left(F_q \times cos\theta\right)$, and

$T_\theta = T_q \rightarrow T_\theta = F_q \times sin\theta$

$\rightarrow \sigma_\theta = \frac{N_\theta}{A_\theta}$, and $\tau_\theta = \frac{T_\theta}{A_\theta}$

$\rightarrow \sigma_\theta = \frac{(N_\theta \times A_\theta) + \left(F_q \times cos\theta\right)}{A_\theta}$, and $\tau_\theta = \frac{(F_q \times sin\theta)}{A_\theta}$

$\rightarrow \sigma_\theta = \sigma_3 + \frac{(F_q \times cos\theta)}{A_\theta}$, and $\tau_\theta = \frac{(F_q \times sin\theta)}{A_\theta}$.

3) post-peak or post-sliding phase ($q > 0$):

- First approach:

For the phase 1 and 2, however, this study introduces force equilibrium instead of Equation 3.8, the response of normal and tangential shear stresses on the plane of failure is not different from the conventional methods, and it was only a new perspective for elaboration the data. This equality between this study and conventional methods can be another evident that the force equilibriums and the effective areas were calculated correctly.

In this phase, due to sliding along the failure plane and reduction in contact area, the force equilibrium will result in different normal and tangential stresses compared to conventional methods.

Here, $\sigma_\theta = (\sigma_\theta)_c + (\sigma_\theta)_q \rightarrow N_\theta = N_c + N_q$, and $\tau_\theta = (\tau_\theta)_q \rightarrow T_\theta = T_q$, so the force equilibrium can be shown as the Fig. A7,

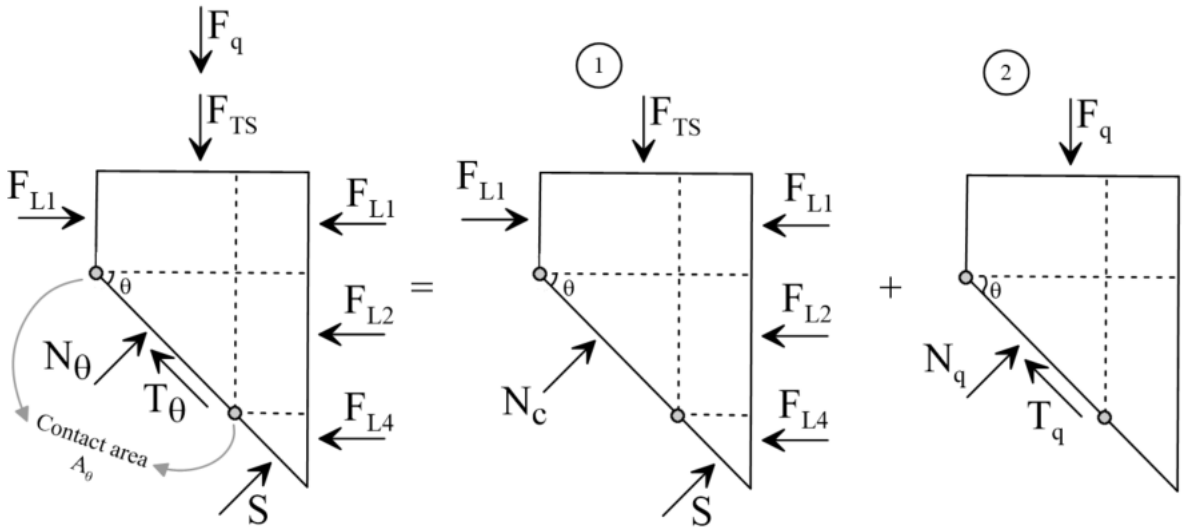

Fig. A7) Forces acting on the top block in the post-peak or post-sliding phase (q > 0).

At first, to compute N_c, by looking at ① in Fig. A7, the force equilibrium can be shown as Fig. A8:

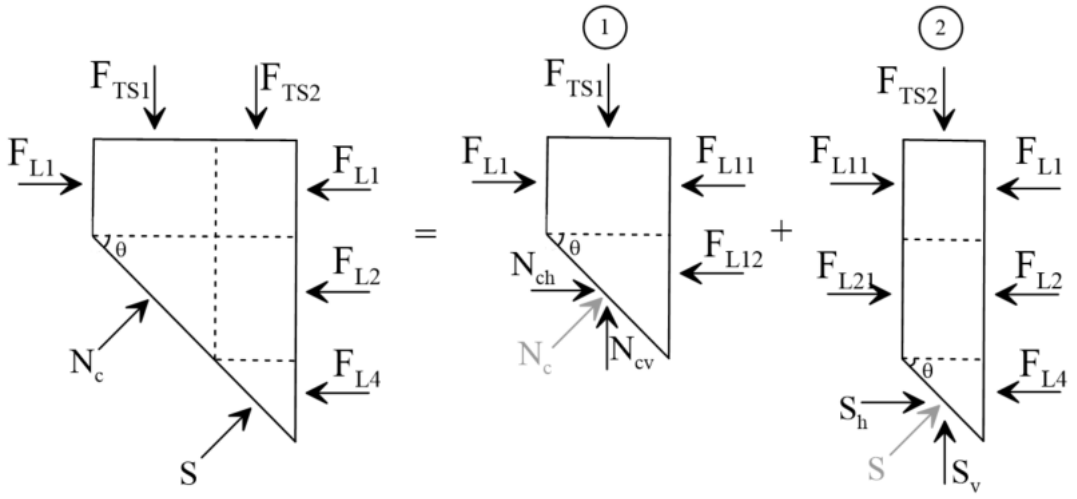

Fig. A8) Another way to show the forces of Fig. A7, part 1.

By looking at ② in Fig. A8, the force equilibrium can be shown as Fig. A9:

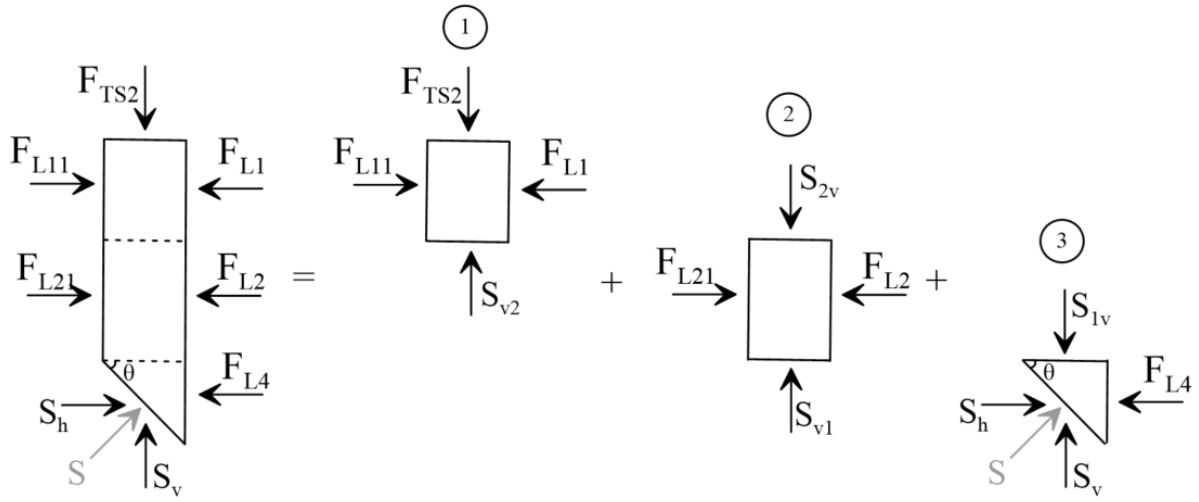

Fig. A9) Another way to show the forces of Fig. A8, part 2.

The force equilibrium in ③ of the Fig. A9 can be written as (*S* is the force for outside of the contact area on the failure plane):

Vertical: $S_{1v} - S_v = 0$, also $S_{1v} = S_{v1} \rightarrow S_{1v} = S_{v1} = S_v$,

Horizontal: $F_{L4} - S_h = 0 \rightarrow F_{L4} = S_h$.

The force equilibrium in ② of the Fig. A9 can be written as:

Vertical: $S_{2v} - S_{v1} = 0$, also $S_{2v} = S_{v2}$, and $S_{v1} = S_v$, $\rightarrow S_{2v} = S_{v2} = S_v$,

Horizontal: $F_{L2} - F_{L21} = 0$, $\rightarrow F_{L2} = F_{L21}$, and equal σ_3 in all directions, so their effective areas are equal (Fig. A10).

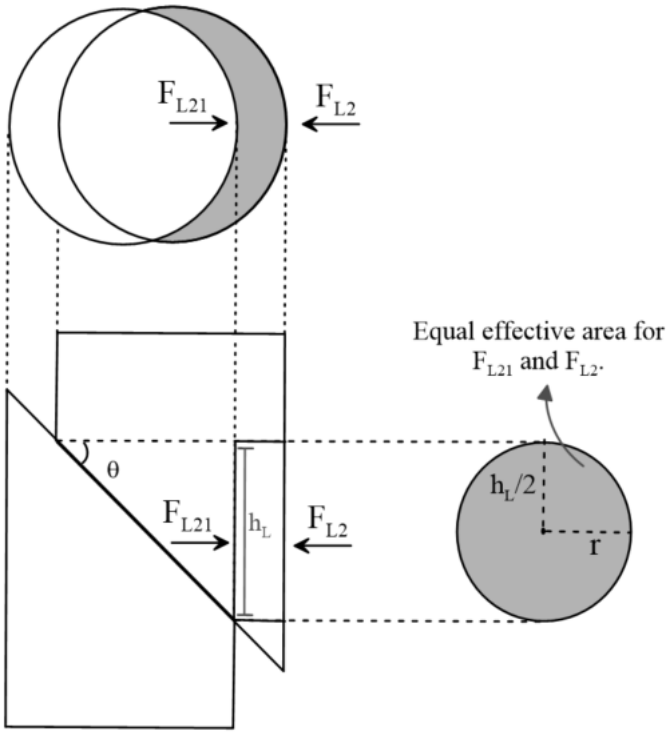

Fig. A10) Equality of the effective area of the forces F_{L2} and F_{L21}.

The force equilibrium in ① of the Fig. A9 can be written as:

Vertical: $F_{TS2} - S_{v2} = 0$, also $S_{v2} = S_v \rightarrow F_{TS2} = S_v$

Horizontal: $F_{L1} - F_{L11} = 0, \rightarrow F_{L1} = F_{L11}$, with the same procedure with Fig. A10, their effective areas are the same.

After these simplifications to find N_c, the force equilibrium for ① in Fig. A8, can be written as:

Horizontal: $F_{L11} - F_{L1} + F_{L12} - N_{ch} = 0$, where $F_{L1} = F_{L11}$, and $F_{L12} = F_{L21} = F_{L2} \rightarrow N_{ch} = F_{L2}$

Vertical: $F_{TS1} - N_{cv} = 0 \rightarrow N_{cv} = F_{TS1}$

$\rightarrow N_c = \frac{F_{TS1}}{cos\theta} = \frac{F_{L2}}{sin\theta} = \sigma_3 \times A_\theta.$

To compute N_q, by looking at ② in Fig. A8, the force equilibrium is the same as:

$N_q = F_q \times cos\theta$, and $T_q = F_q \times sin\theta$,

To sum up.

$$N_\theta = N_c + N_q = (\sigma_3 \times A_\theta) + \left(F_q \times cos\theta\right) \quad (4.9)$$

$$T_\theta = T_q = F_q \times sin\theta \quad (4.10)$$

$\rightarrow \sigma_\theta = \frac{N_\theta}{A_\theta}$, and $\tau_\theta = \frac{T_\theta}{A_\theta}$

$\rightarrow \sigma_\theta = \frac{(\sigma_3 \times A_\theta) + \left(F_q \times cos\theta\right)}{A_\theta}$, and $\tau_\theta = \frac{F_q \times sin\theta}{A_\theta}$

$\rightarrow \sigma_\theta = \sigma_3 + \frac{\left(F_q \times cos\theta\right)}{A_\theta}$, and $\tau_\theta = \frac{\left(F_q \times sin\theta\right)}{A_\theta}$.

The variation of A_θ in this phase, has been calculated in the Section 4.3.

- Second approach without changing the medium:

Force equilibrium:

$$N_\theta = -S + \left[\left(F_q + F_{TS}\right)cos\theta\right] + \left[\left(F_{L2}\right)sin\theta\right] \quad (4.11)$$

$$T_\theta = \left[\left(F_q + F_{TS}\right)sin\theta\right] - \left[\left(F_{L2}\right)cos\theta\right] \quad (4.12)$$

where, N_θ, and T_θ are normal and tangential forces acting on the new or pre-existing failure plane, respectively,

$$S = \sigma_3 \left(\frac{A_{TS}}{cos\theta} - A_\theta\right) \quad (4.13)$$

$$F_{TS} = \sigma_3 A_{TS} = \sigma_3 \pi r^2 \quad (4.14)$$

$$F_{L2} = \sigma_3 A_{L2} = \sigma_3 \pi r^2 tan\theta = \sigma_3 \left[\left(\frac{A_{TS}}{cos\theta}\right) \times sin\theta\right] = \sigma_3 (A_{\theta i} sin\theta) \quad (4.15)$$

F_q = axial load recorded by submerged load cell in triaxial apparatus (kN)

where $A_{\theta i}$ is the initial contact area before sliding onset. By incorporating Equations 4.13, 4.14, and 4.15 into Equation 4.11, it can be shown that,

$$N_\theta = -\sigma_3 \left[\left(\frac{A_{TS}}{cos\theta}\right) - A_\theta\right] + F_q cos\theta + \sigma_3 A_{TS} cos\theta + \sigma_3 A_{L2} sin\theta$$

$$N_\theta = -\sigma_3 \left[\left(\frac{\pi r^2}{cos\theta}\right) - A_\theta\right] + F_q cos\theta + \sigma_3 \pi r^2 cos\theta + \sigma_3 \pi r^2 tan\theta sin\theta$$

$$N_\theta = F_q cos\theta + \left[(\sigma_3 \pi r^2)\left[\left(\frac{-1}{cos\theta}\right) + \left(\frac{A_\theta}{\pi r^2}\right) + cos\theta + \left(\frac{sin^2\theta}{cos\theta}\right)\right]\right]$$

$$N_\theta = F_q cos\theta + \left[(\sigma_3 \pi r^2)\left[\left(\frac{-1 + cos^2\theta + sin^2\theta}{cos\theta}\right) + \left(\frac{A_\theta}{\pi r^2}\right)\right]\right]$$

$$N_\theta = F_q cos\theta + \left[(\sigma_3 \pi r^2)\left[\left(\frac{A_\theta}{\pi r^2}\right)\right]\right]$$

$$N_\theta = F_q cos\theta + [(\sigma_3 A_\theta)] \quad (4.9)$$

$$\sigma_\theta = \frac{F_q cos\theta}{A_\theta} + \sigma_3$$

By incorporating Equations 4.13, 4.14, and 4.15 into Equation 4.12, it can be shown that,

$$T_\theta = F_q sin\theta + \sigma_3 A_{TS} sin\theta - \sigma_3 A_{L2} cos\theta$$

$$T_\theta = F_q sin\theta + \sigma_3 \pi r^2 sin\theta - \sigma_3 \pi r^2 tan\theta cos\theta$$

$$T_\theta = F_q sin\theta + [(\sigma_3 \pi r^2)(sin\theta - tan\theta cos\theta)]$$

$$T_\theta = F_q sin\theta + [(\sigma_3 \pi r^2)(sin\theta - sin\theta)]$$

$$T_\theta = F_q sin\theta \quad (4.10)$$

$$\tau_\theta = \frac{F_q sin\theta}{A_\theta}$$

- **New failure plane formation in the post-sliding phase**:

Initial phase:

Force equilibrium (second approach):

$N_{\lambda i} = \left[(S_f) sin(90 - \theta - \lambda)\right] + \left[(F_q + F_{TS})\right] cos\lambda + \left[(F_{L3} + F_f) sin\lambda\right]$, (Eq1)

$T_{\lambda i} = \left[(S_f) \cos(90 - \theta - \lambda)\right] + \left[(F_q + F_{TS}) sin\lambda\right] - \left[(F_{L3} + F_f) cos\lambda\right]$ (Eq2)

where, $N\lambda$, and $T\lambda$ are normal and tangential forces acting on the new failure plane, respectively.

- **Finding the effective area ($A_{\lambda i} \times sin\lambda$) of F_{L3}** (Fig. A11, Fig. A12, and Fig. A13):

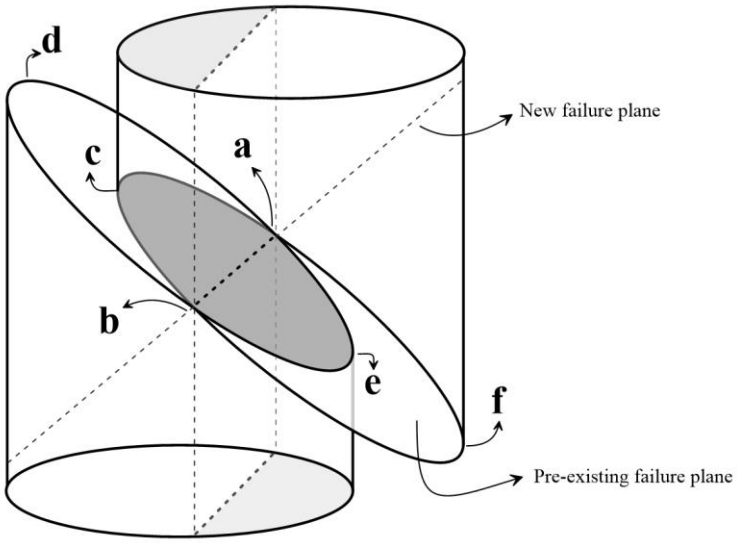

Fig. A11) 3-D view of initial phase of new failure plane formation in the post-sliding phase.

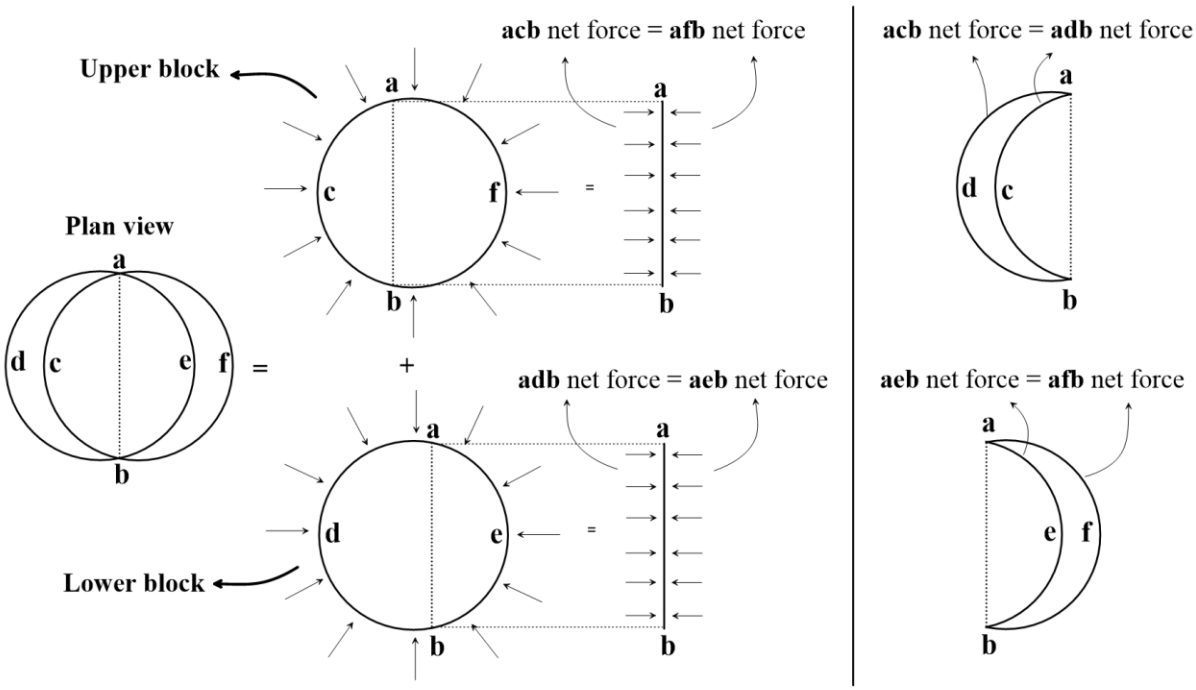

Fig. A12) Equality between the effective area of the acbf and adbe ellipses.

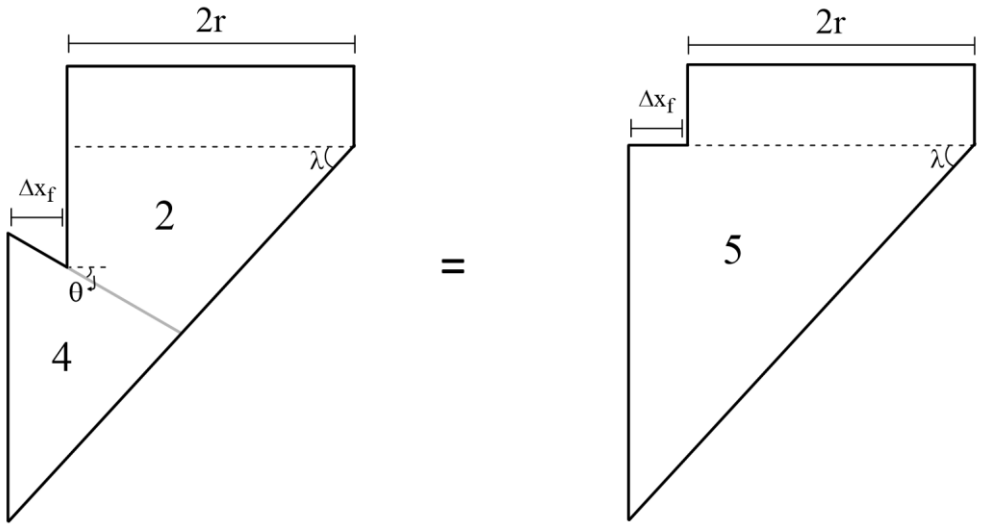

Fig. A13) Equal shapes as a subsequent result of the Fig. A12.

Referring to Fig. A3 and Fig. A4 $A_{L2} = \pi r^2 tan\theta = \left[\left(\frac{A_{TS}}{cos\theta}\right) \times sin\theta\right] = (A_{\theta i} sin\theta)$ where $A_{\theta i}$ is the initial contact area of pre-existing failure plane, therefore here referring to Fig. A13, it is clear that A_{L3}, the effective area of F_{L3}, is equal to $A_{\lambda i} \times sin\lambda$.

Final phase:

Force equilibrium (second approach):

$$N_\lambda = -(S^*) + \left[(S_f) sin(90 - \theta - \lambda)\right] + \left[(F_q + F_{TS})\right] cos\lambda + \left[(F_{L3} + F_f) sin\lambda\right]$$

$$T_\lambda = \left[(S_f) \cos(90 - \theta - \lambda)\right] + \left[(F_q + F_{TS}) sin\lambda\right] - \left[(F_{L3} + F_f) cos\lambda\right]$$

Appendix B: Application of Sliding Block Method

Figures B1 through B9 provide a detailed comparison between the Sliding Block Method (SBM) and Conventional Methods (CM). In these figures, θ represents the inclination of the pre-existing failure plane, and f denotes the inclination of the failure plane formed in homogenous specimens as well as in specimens with a pre-existing failure plane that did not undergo sliding onset on its plane. Additionally, λ indicates the inclination of the newly formed failure plane during the post-sliding phase.

Figures B1, B2, and B3 illustrate the application of the Sliding Block Method on the p'-q graphs, comparing it with the Conventional Methods. These figures also show the variation of radius versus axial strains for both methods.

Figures B4 to B9 demonstrate the application of the Sliding Block Method on the σ'_n-τ graphs and its comparison with the Conventional Methods. These figures additionally depict the ratio of the considered contact area for the Sliding Block Method to the contact area for Conventional Methods versus axial strains.

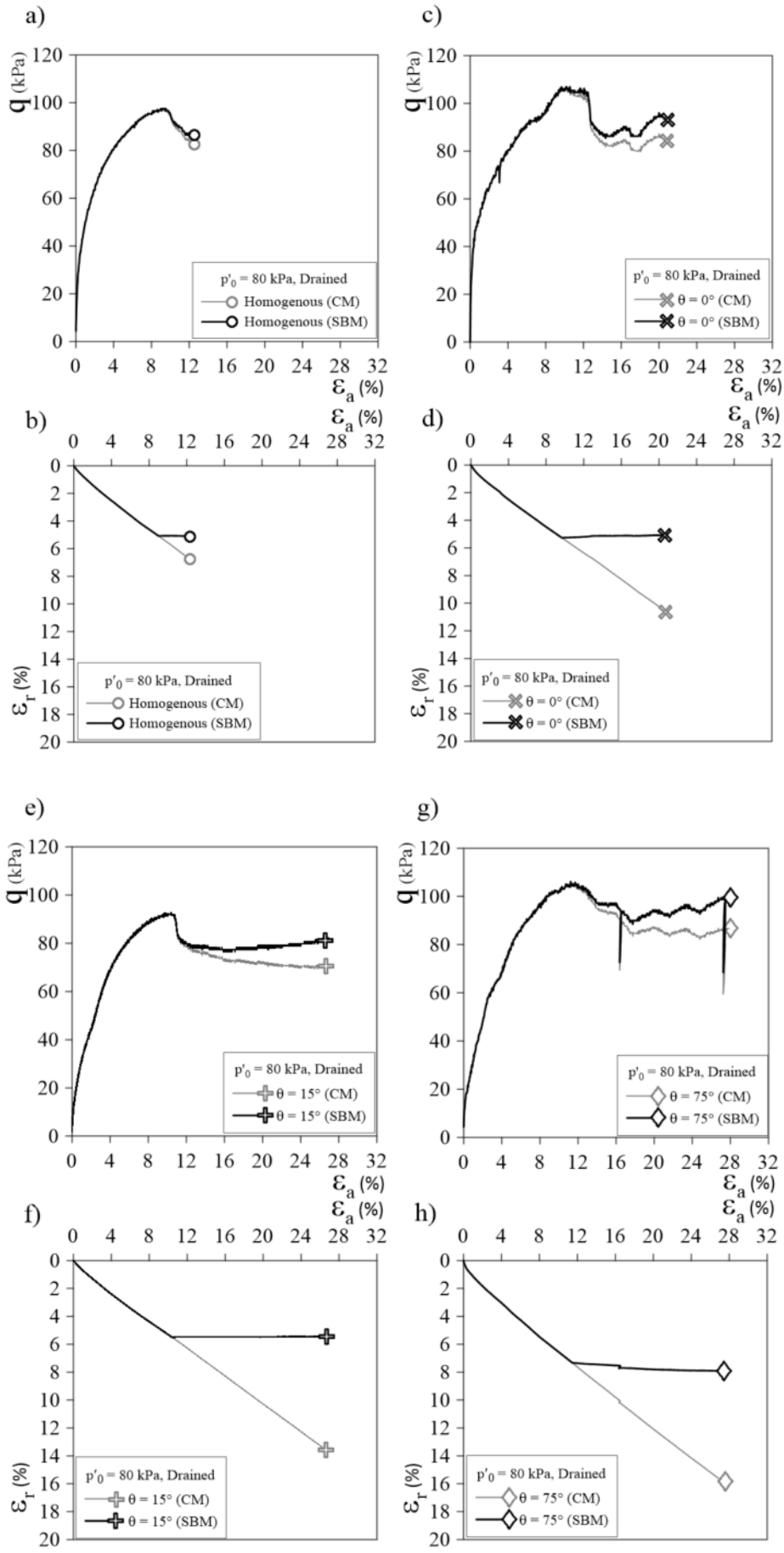
a)
c)
b)
d)
e)
g)
f)
h)
q (kPa)
ε_a (%)
ε_r (%)
p'0 = 80 kPa, Drained
Homogenous (CM)
Homogenous (SBM)
θ = 0° (CM)
θ = 0° (SBM)
θ = 15° (CM)
θ = 15° (SBM)
θ = 75° (CM)
θ = 75° (SBM)

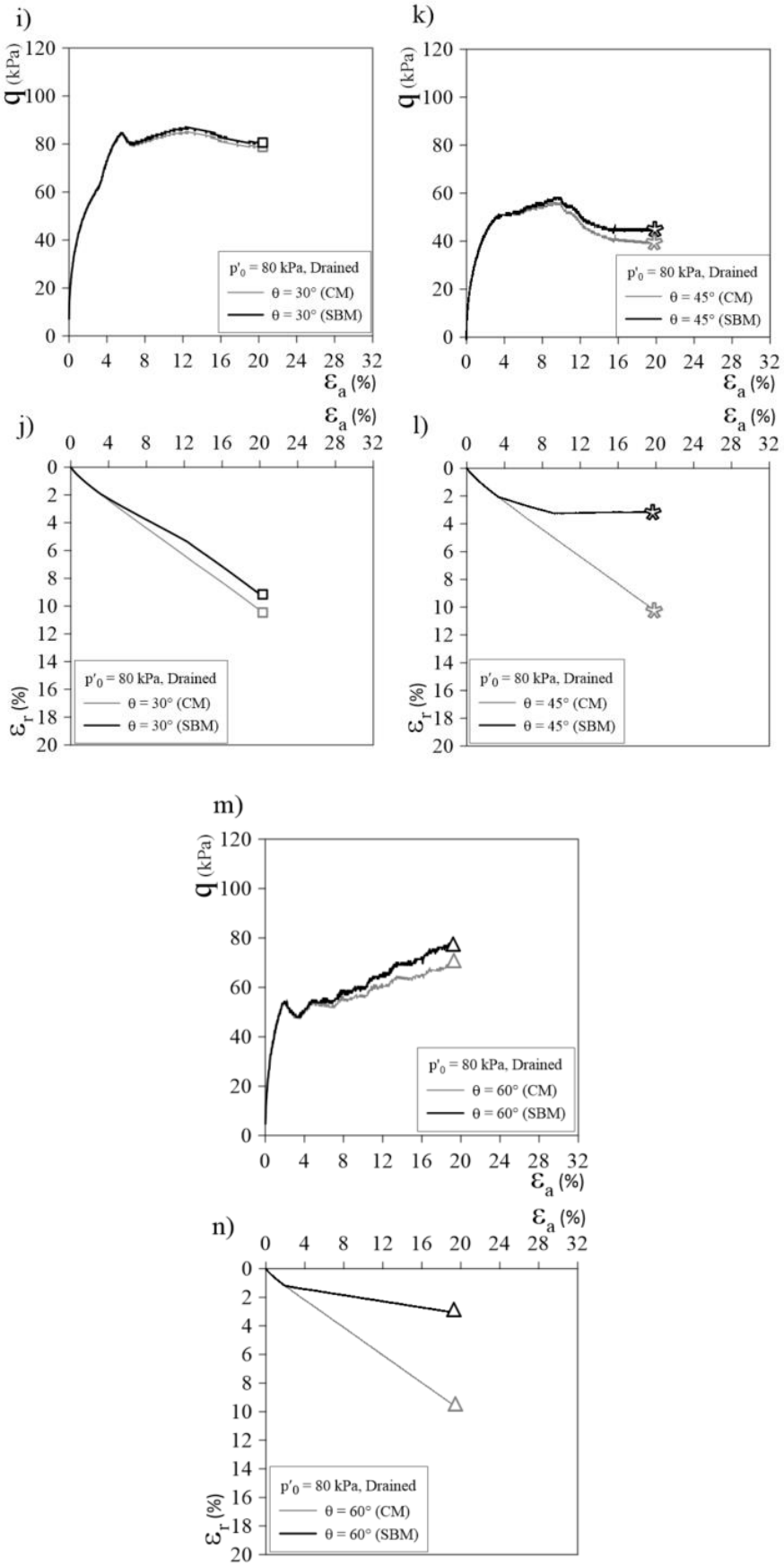

Fig. B1) Comparison of shearing phase interpretations between conventional methods (CM) and sliding block method (SBM) for specimens under drained condition with p'_0 = 80 kPa ($q - \varepsilon_a$ and $\varepsilon_r - \varepsilon_a$).

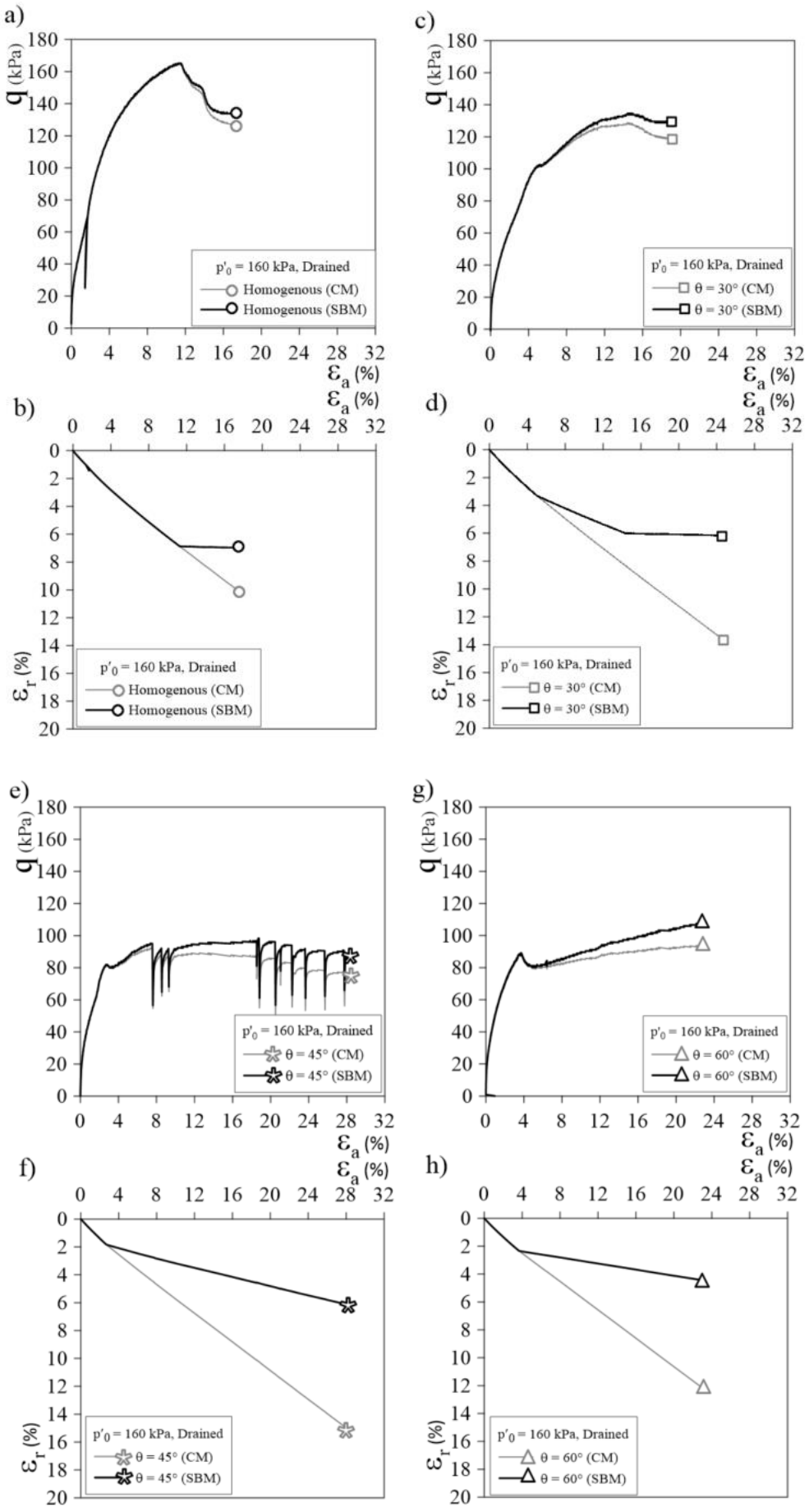
a)
q (kPa)
ε_a (%)
p'0 = 160 kPa, Drained
Homogenous (CM)
Homogenous (SBM)
b)
ε_r (%)
ε_a (%)
p'0 = 160 kPa, Drained
Homogenous (CM)
Homogenous (SBM)
c)
q (kPa)
ε_a (%)
p'0 = 160 kPa, Drained
θ = 30° (CM)
θ = 30° (SBM)
d)
ε_r (%)
ε_a (%)
p'0 = 160 kPa, Drained
θ = 30° (CM)
θ = 30° (SBM)
e)
q (kPa)
ε_a (%)
p'0 = 160 kPa, Drained
θ = 45° (CM)
θ = 45° (SBM)
f)
ε_r (%)
ε_a (%)
p'0 = 160 kPa, Drained
θ = 45° (CM)
θ = 45° (SBM)
g)
q (kPa)
ε_a (%)
p'0 = 160 kPa, Drained
θ = 60° (CM)
θ = 60° (SBM)
h)
ε_r (%)
ε_a (%)
p'0 = 160 kPa, Drained
θ = 60° (CM)
θ = 60° (SBM)

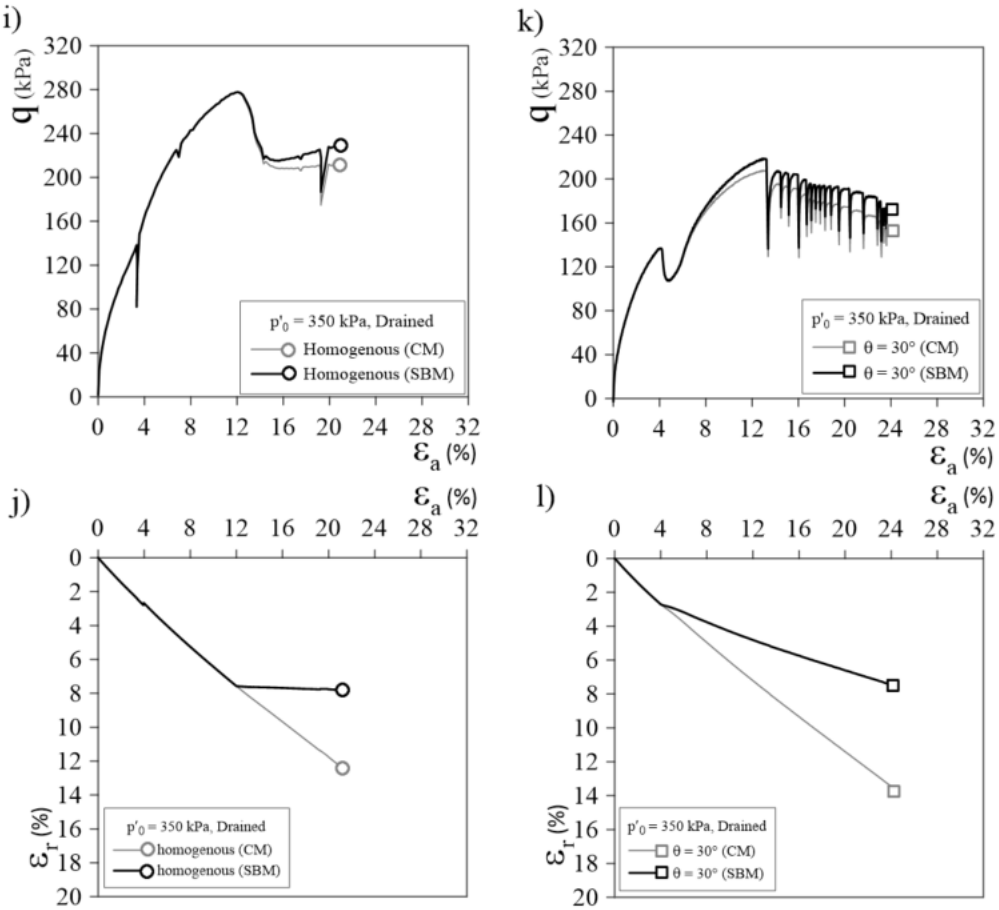

Fig. B2) Comparison of shearing phase interpretations between conventional methods (CM) and sliding block method (SBM) for specimens under drained condition with p'_0 = 160 and 350 kPa ($q - \varepsilon_a$ and $\varepsilon_r - \varepsilon_a$).

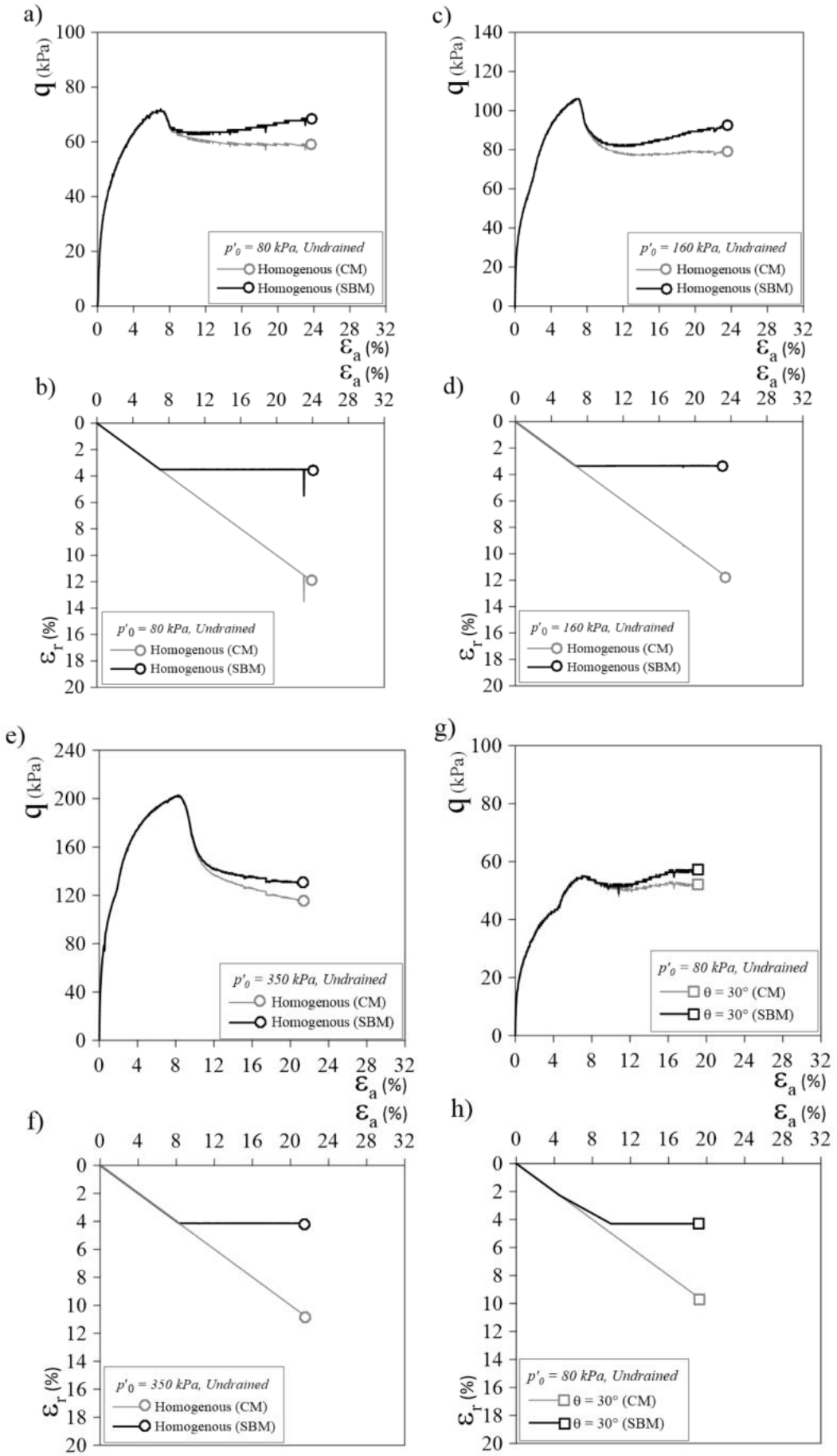
a)
q (kPa)
p'_0 = 80 kPa, Undrained
Homogenous (CM)
Homogenous (SBM)
ε_a (%)
b)
ε_r (%)
c)
p'_0 = 160 kPa, Undrained
d)
e)
p'_0 = 350 kPa, Undrained
f)
g)
θ = 30° (CM)
θ = 30° (SBM)
h)

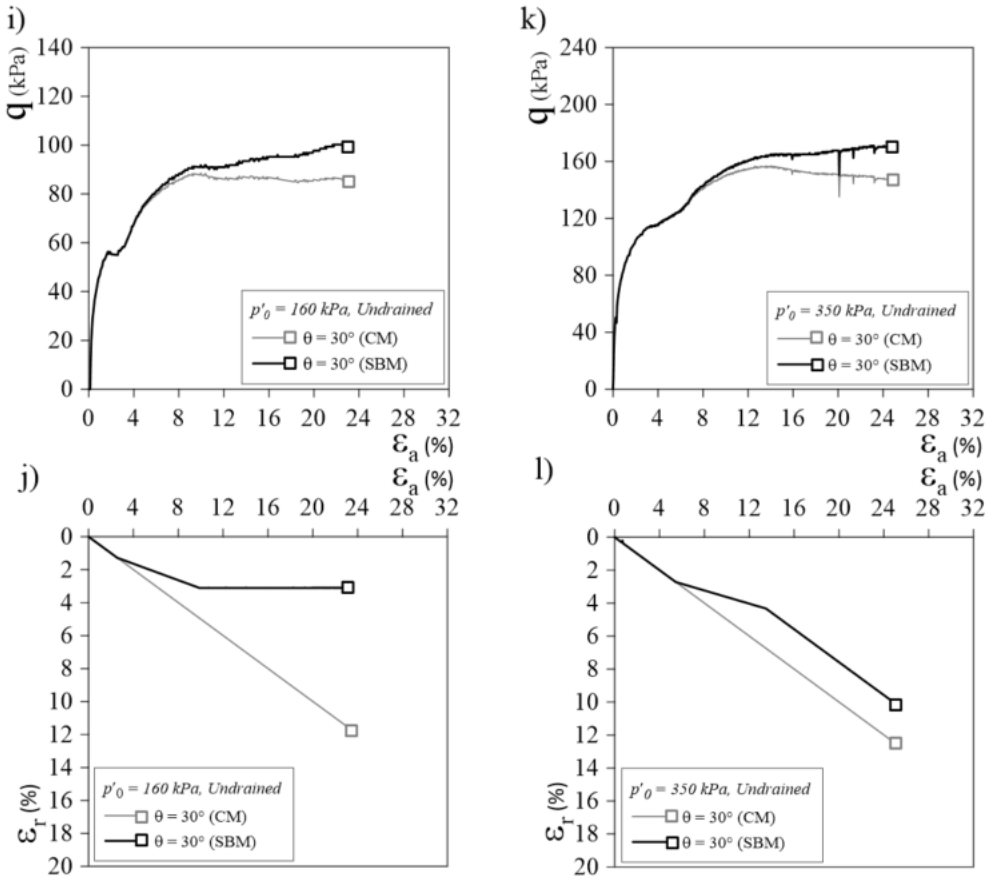

Fig. B3) Comparison of shearing phase interpretations between conventional methods (CM) and sliding block method (SBM) for specimens under undrained condition with p'_0 = 80, 160 and 350 kPa ($q - \varepsilon_a$ and $\varepsilon_r - \varepsilon_a$).

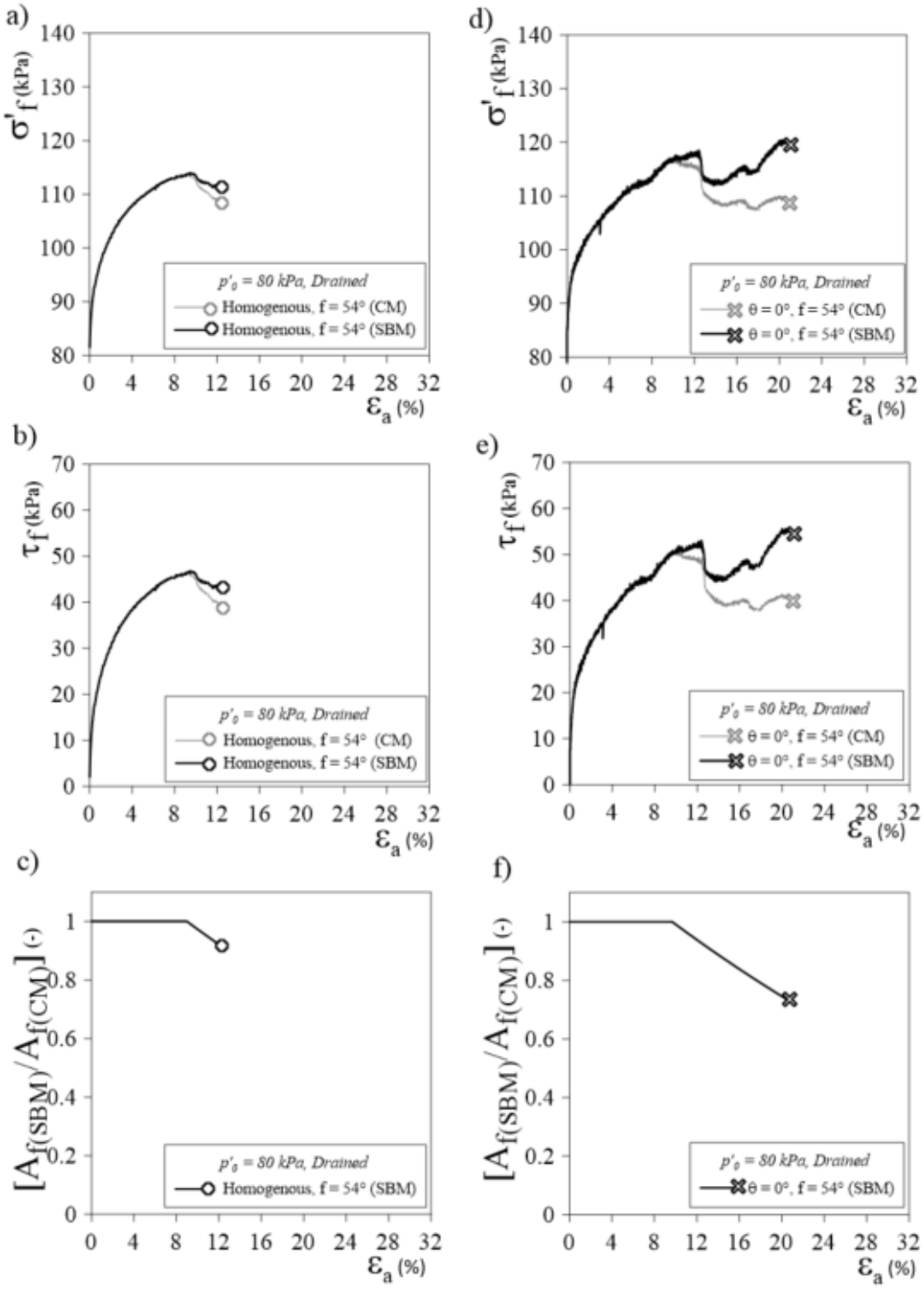
a)
d)
b)
e)
c)
f)
σ'_f (kPa)
τ_f (kPa)
$[A_{f(SBM)}/A_{f(CM)}]$ (-)
ε_a (%)
p'_0 = 80 kPa, Drained
Homogenous, f = 54° (CM)
Homogenous, f = 54° (SBM)
θ = 0°, f = 54° (CM)
θ = 0°, f = 54° (SBM)

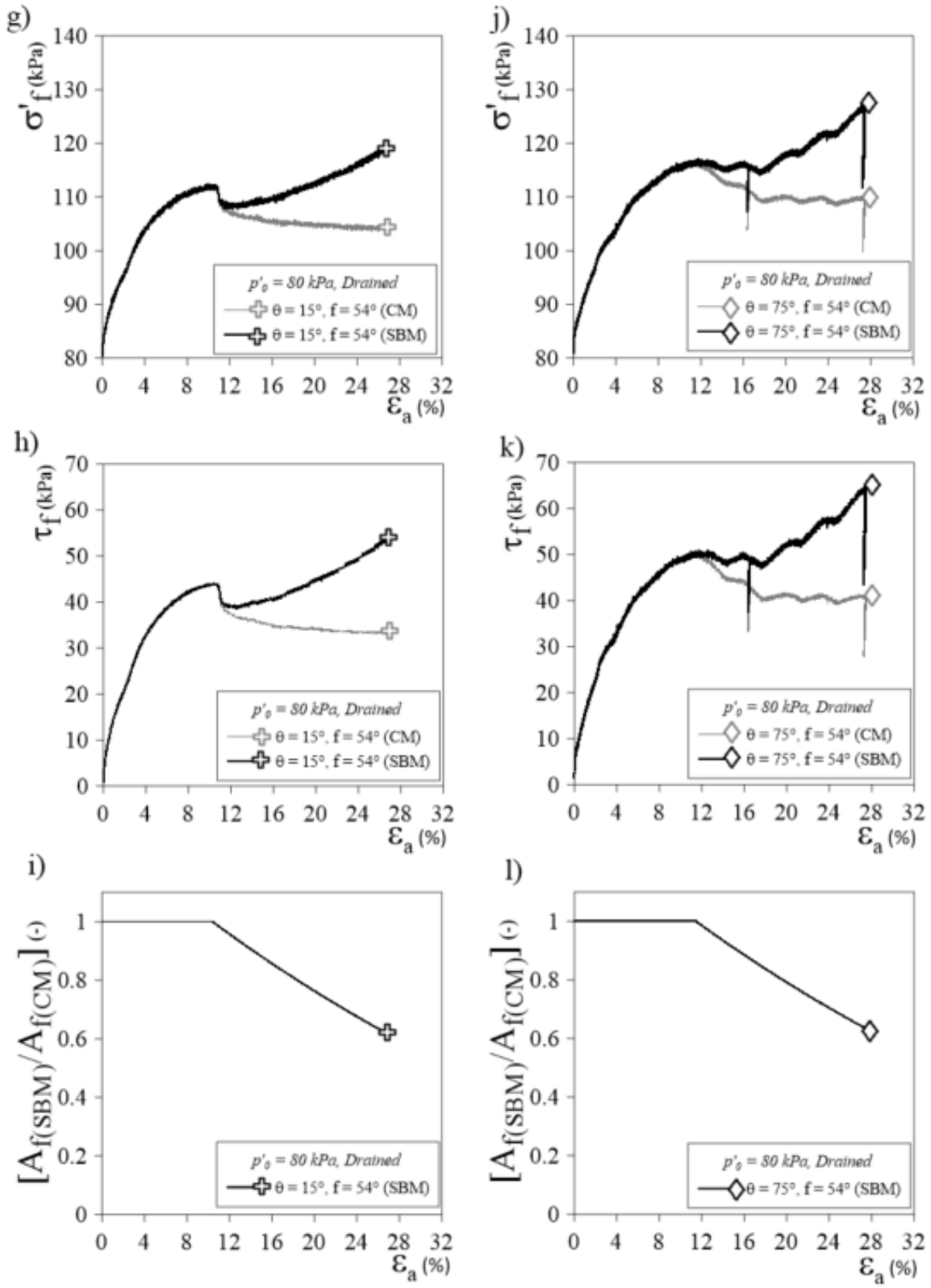

Fig. B4) Comparison of shearing phase interpretations between conventional methods (CM) and sliding block method (SBM) for specimens under drained condition with p'_0 = 80 kPa ((σ_f' – ε_a), (τ_f - ε_a), and (contact areas ratio – ε_a)), (for specimens which experience post-peak stage, instead of θ, f has used as the failure plane inclination).

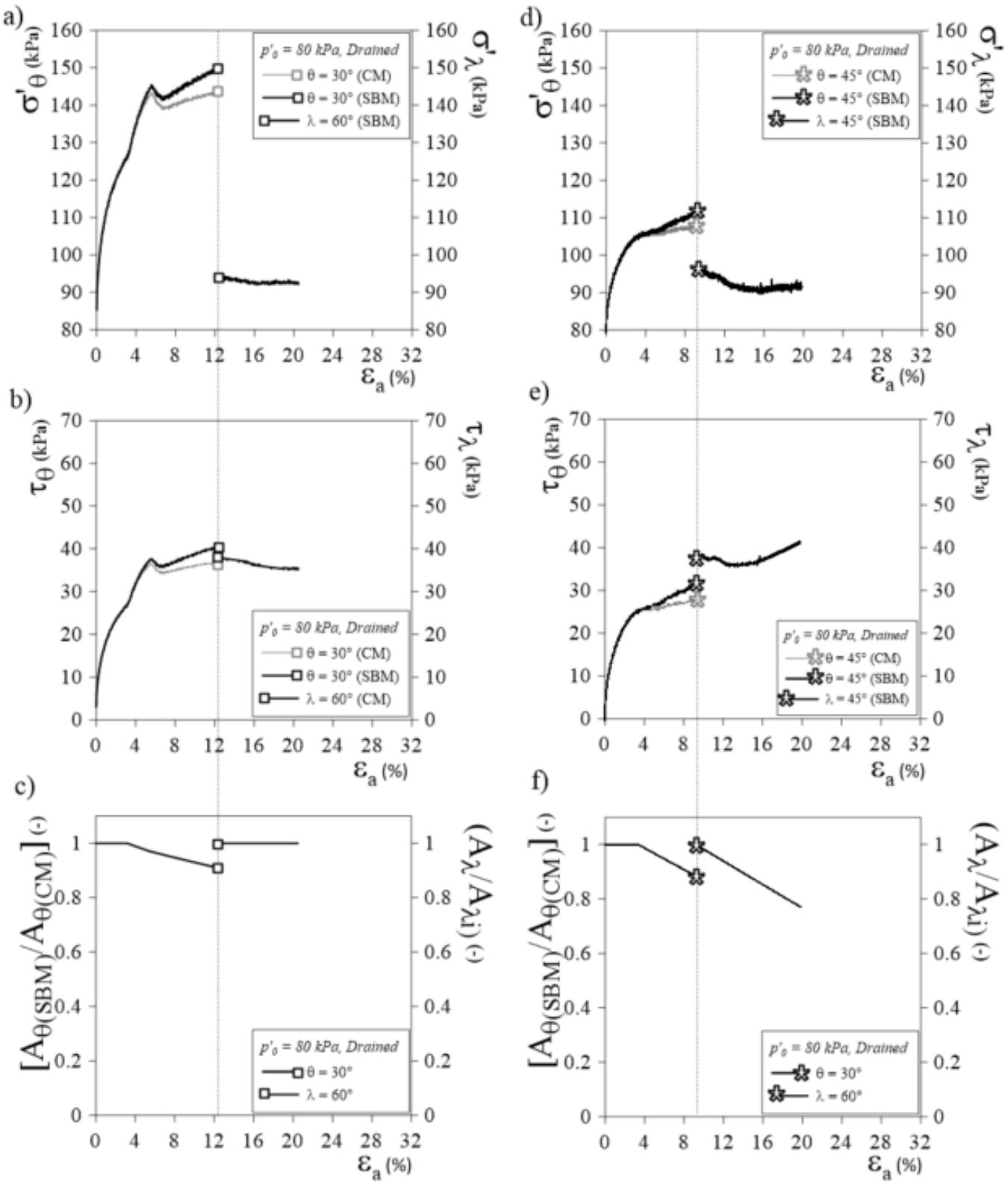
a)
d)
b)
e)
c)
f)
σ'_θ (kPa)
σ'_λ (kPa)
τ_θ (kPa)
τ_λ (kPa)
$[A_{\theta(SBM)}/A_{\theta(CM)}]$ (-)
$(A_\lambda/A_{\lambda i})$ (-)
ε_a (%)
p'_0 = 80 kPa, Drained
θ = 30° (CM)
θ = 30° (SBM)
λ = 60° (SBM)
λ = 60° (CM)
θ = 45° (CM)
θ = 45° (SBM)
λ = 45° (SBM)
θ = 30°
λ = 60°
θ = 45°
λ = 45°

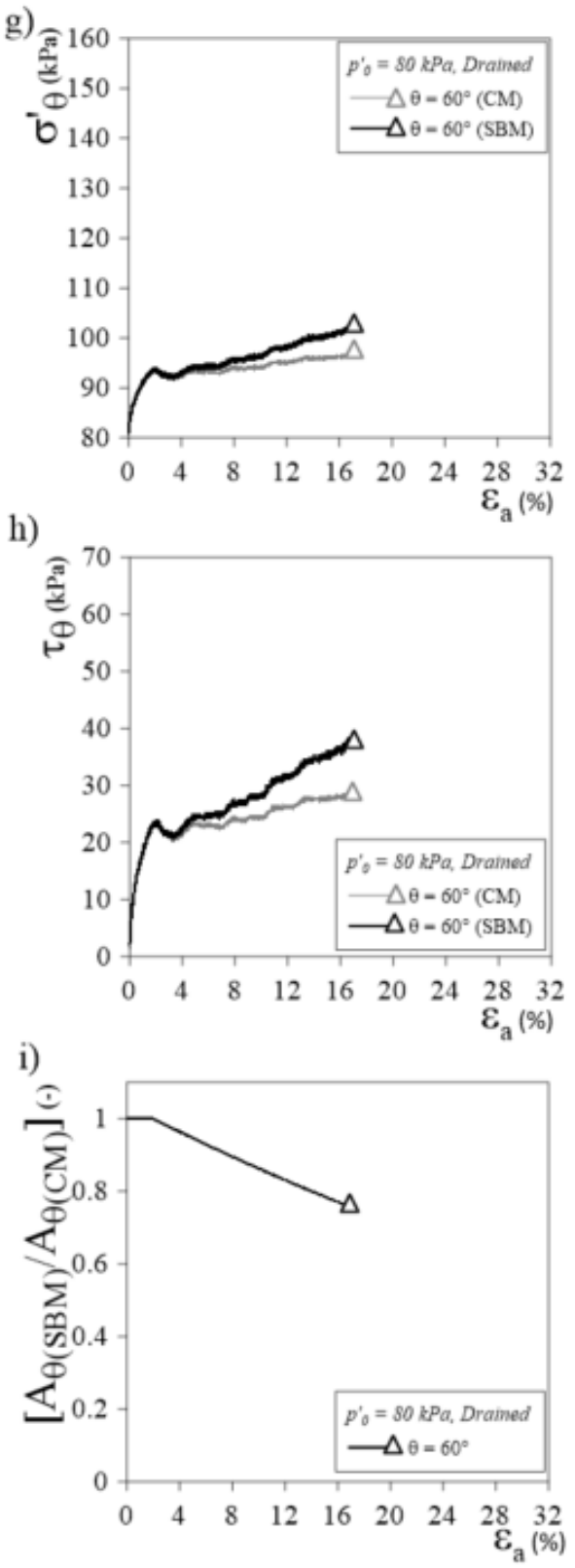

Fig. B5) Comparison of shearing phase interpretations between conventional methods (CM) and sliding block method (SBM) for specimens under drained condition with p'$_0$ = 80 kPa ((σ_θ' – ε_a), (τ_θ - ε_a), and (contact areas ratio – ε_a)), (for specimens which experience post-sliding stage, θ has used as the pre-existing failure plane inclination).

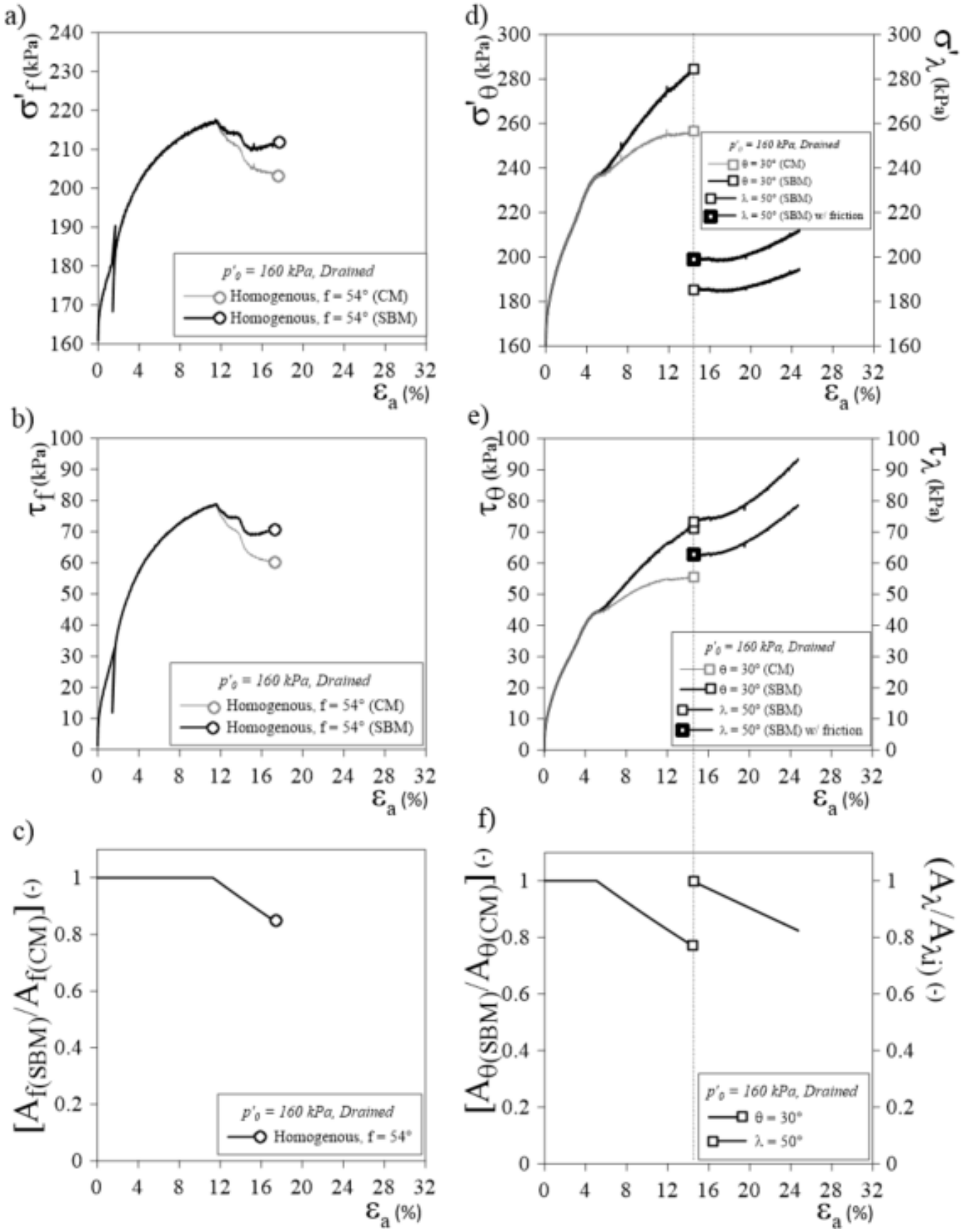
a)
σ'_f (kPa)
p'_0 = 160 kPa, Drained
Homogenous, f = 54° (CM)
Homogenous, f = 54° (SBM)
ε_a (%)
b)
τ_f (kPa)
p'_0 = 160 kPa, Drained
Homogenous, f = 54° (CM)
Homogenous, f = 54° (SBM)
ε_a (%)
c)
$[A_{f(SBM)}/A_{f(CM)}]$ (-)
p'_0 = 160 kPa, Drained
Homogenous, f = 54°
ε_a (%)
d)
σ'_θ (kPa)
σ'_λ (kPa)
p'_0 = 160 kPa, Drained
θ = 30° (CM)
θ = 30° (SBM)
λ = 50° (SBM)
λ = 50° (SBM) w/ friction
ε_a (%)
e)
τ_θ (kPa)
τ_λ (kPa)
p'_0 = 160 kPa, Drained
θ = 30° (CM)
θ = 30° (SBM)
λ = 50° (SBM)
λ = 50° (SBM) w/ friction
ε_a (%)
f)
$[A_{\theta(SBM)}/A_{\theta(CM)}]$ (-)
$(A_\lambda/A_{\lambda i})$ (-)
p'_0 = 160 kPa, Drained
θ = 30°
λ = 50°
ε_a (%)

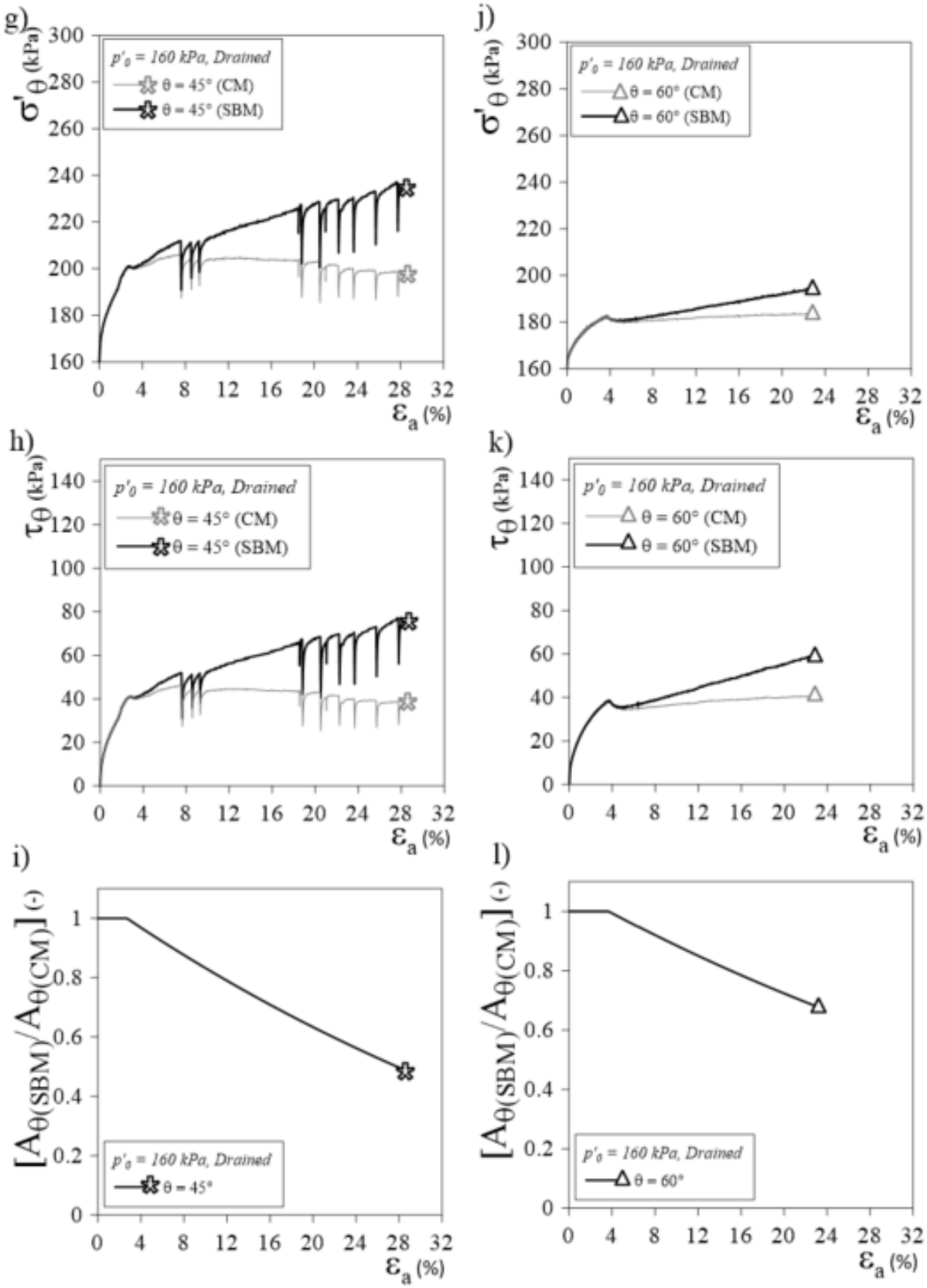

Fig. B6) Comparison of shearing phase interpretations between conventional methods (CM) and sliding block method (SBM) for specimens under drained condition with p'0 = 160 kPa ((σ_f' – ε_a), (τ_f - ε_a), and (contact areas ratio – ε_a)), (for specimens which experience post-sliding stage, θ has used as the pre-existing failure plane inclination).

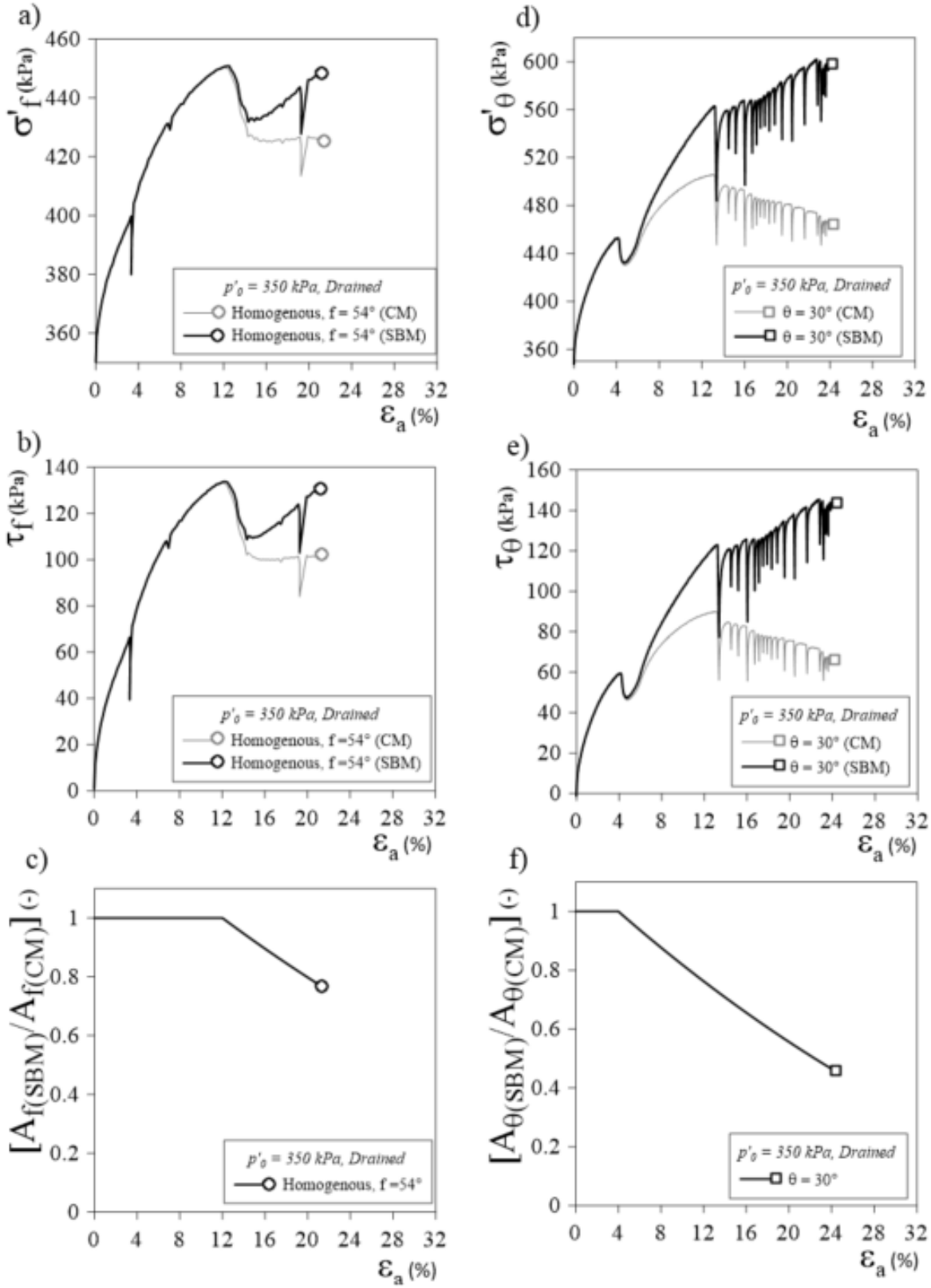

Fig. B7) Comparison of shearing phase interpretations between conventional methods (CM) and sliding block method (SBM) for specimens under drained condition with p'_0 = 350 kPa ((σ_f', σ_θ'– ε_a), (τ_f, τ_θ - ε_a), and (contact areas ratio – ε_a)).

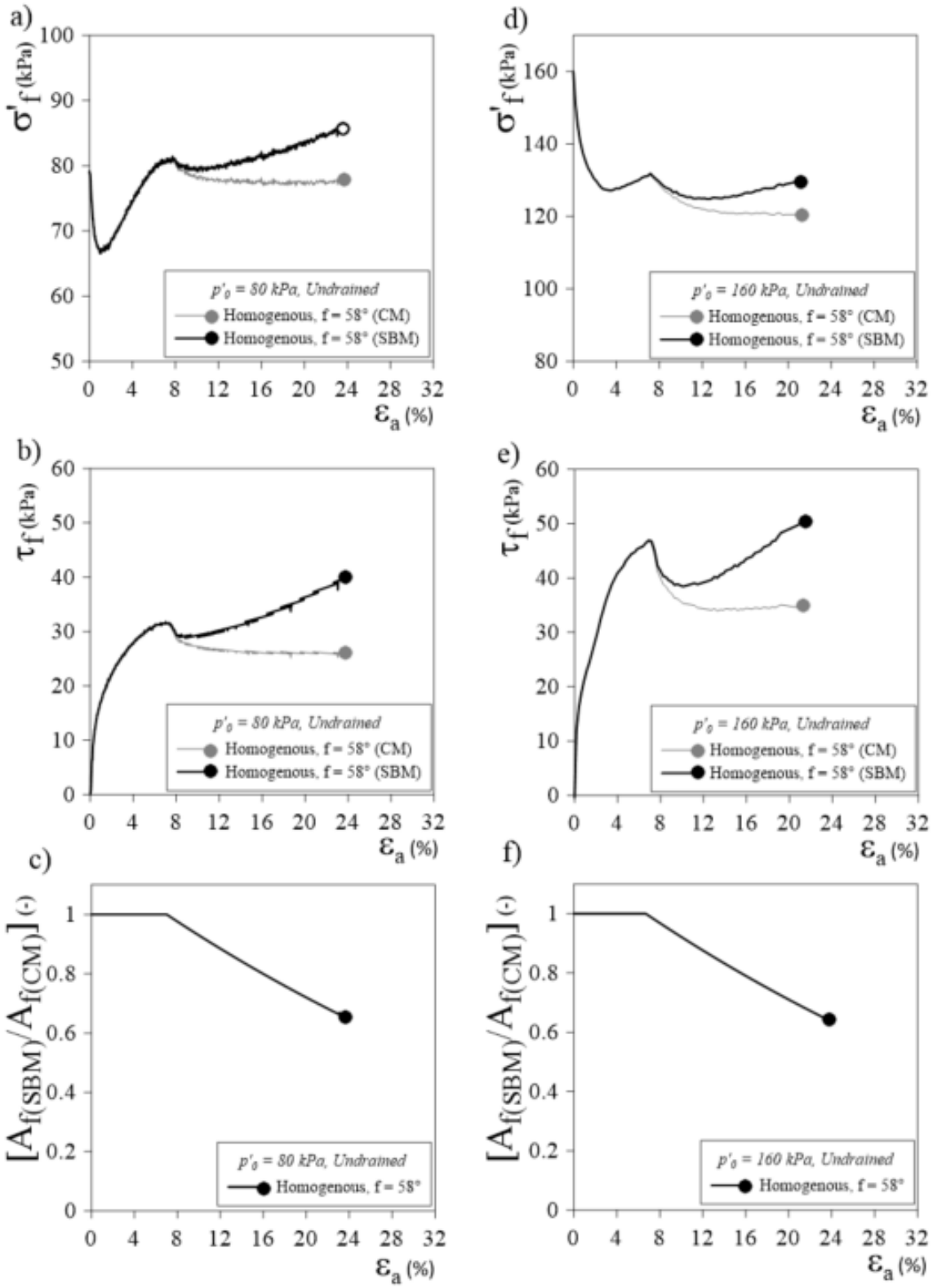
a)
σ'_{f} (kPa)
p'_0 = 80 kPa, Undrained
Homogenous, f = 58° (CM)
Homogenous, f = 58° (SBM)
ε_a (%)
d)
σ'_{f} (kPa)
p'_0 = 160 kPa, Undrained
Homogenous, f = 58° (CM)
Homogenous, f = 58° (SBM)
ε_a (%)
b)
τ_f (kPa)
p'_0 = 80 kPa, Undrained
Homogenous, f = 58° (CM)
Homogenous, f = 58° (SBM)
ε_a (%)
e)
τ_f (kPa)
p'_0 = 160 kPa, Undrained
Homogenous, f = 58° (CM)
Homogenous, f = 58° (SBM)
ε_a (%)
c)
$[A_{f(SBM)}/A_{f(CM)}]$ (-)
p'_0 = 80 kPa, Undrained
Homogenous, f = 58°
ε_a (%)
f)
$[A_{f(SBM)}/A_{f(CM)}]$ (-)
p'_0 = 160 kPa, Undrained
Homogenous, f = 58°
ε_a (%)

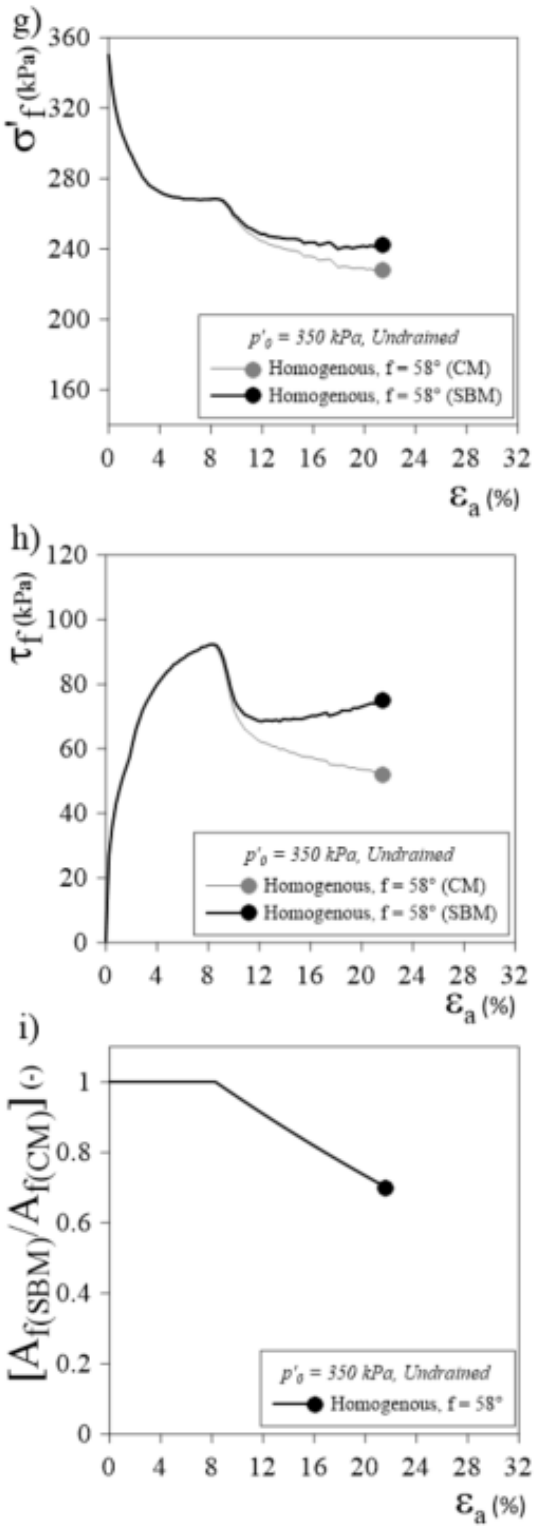

Fig. B8) Comparison of shearing phase interpretations between conventional methods (CM) and sliding block method (SBM) for specimens under undrained condition with p'_0 = 80, 160 and 350 kPa ((σ_f' – ε_a), (τ_f - ε_a), and (contact areas ratio – ε_a)), (for homogenous specimens which experience post-peak stage, f has used as the failure plane inclination).

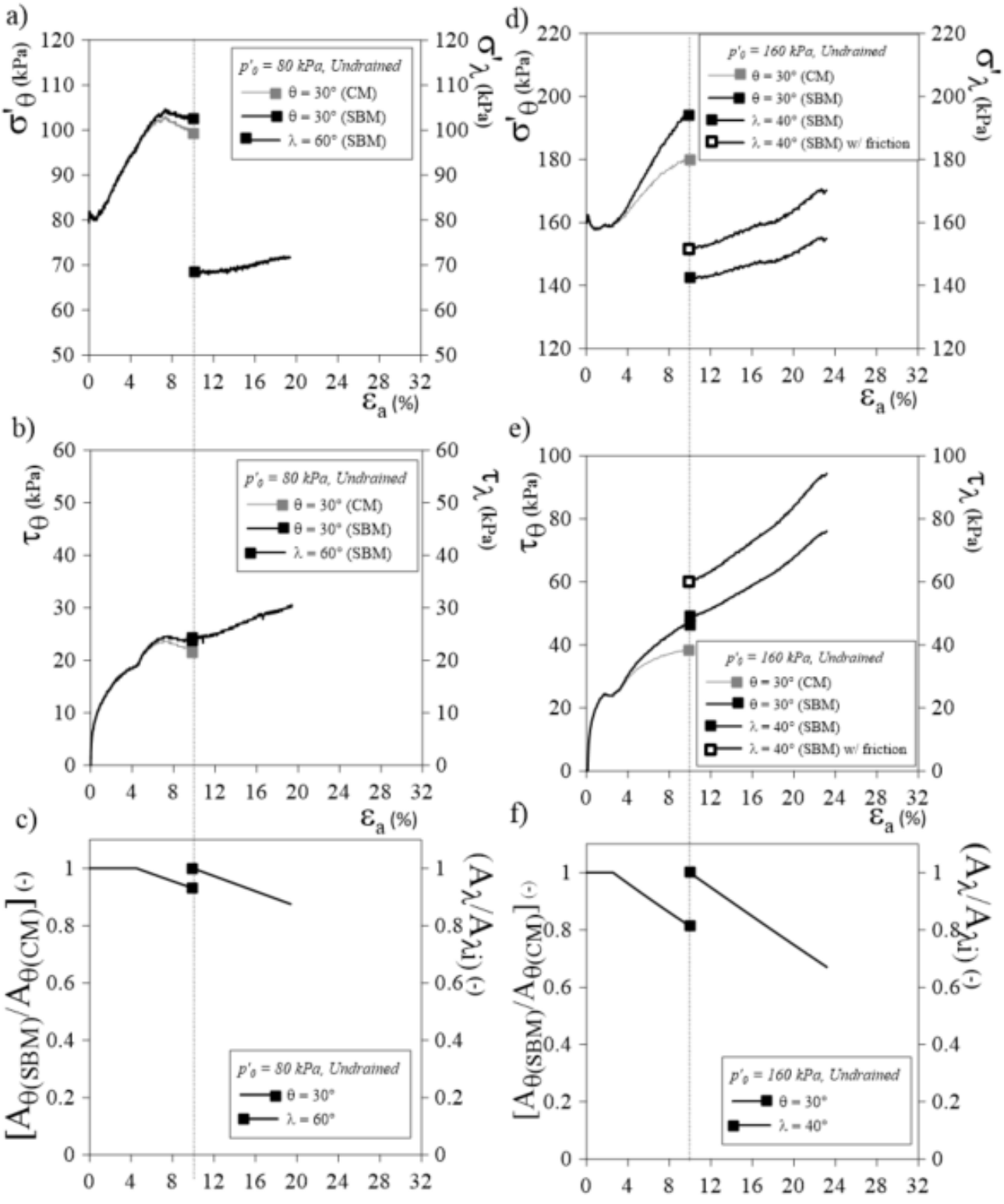
a)
b)
c)
d)
e)
f)
p'0 = 80 kPa, Undrained
θ = 30° (CM)
θ = 30° (SBM)
λ = 60° (SBM)
p'0 = 160 kPa, Undrained
λ = 40° (SBM)
λ = 40° (SBM) w/ friction
σ'θ (kPa)
σ'λ (kPa)
τθ (kPa)
τλ (kPa)
εa (%)
[Aθ(SBM)/Aθ(CM)] (-)
(Aλ/Aλi) (-)

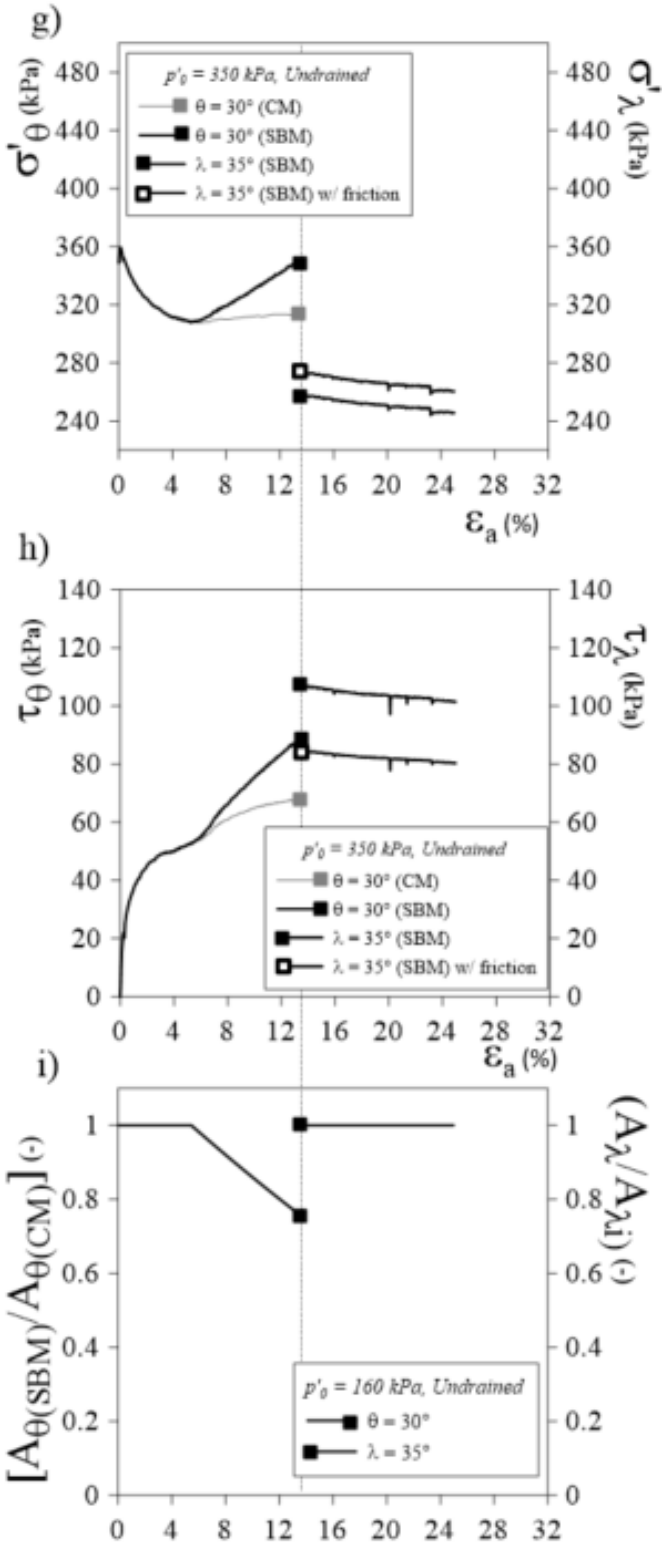

Fig. B9) Comparison of shearing phase interpretations between conventional methods (CM) and sliding block method (SBM) for specimens with $\theta = 30°$ under undrained condition with p'_0 = 80, 160 and 350 kPa ((σ_θ', σ_λ' – ε_a), (τ_θ, τ_λ - ε_a), and (contact areas ratio – ε_a)).